# FULL SCALE COMPONENT LEVEL TESTING & SEVERITY ANALYSIS OF PHANTOM 3 UAV TO CESSNA 182B AIRCRAFT COLLISIONS

by

Benjamin Woodruff Hayes

A thesis submitted in partial fulfillment
of the requirements for the degree

of

Master of Science

in

Mechanical Engineering

MONTANA STATE UNIVERSITY
Bozeman, Montana

May, 2021

©COPYRIGHT

by

Benjamin Woodruff Hayes

2021

All Rights Reserved

# ACKNOWLEDGEMENTS

I would like to thank professor Robb Larson and Dr. Douglas Cairns for their wisdom and guidance throughout the project. I would also like to thank Forrest Arnold along with the undergraduate researchers and capstone group who devoted time and effort into the research process. I would like to thank ASSURE for their support and funding of this work. Additionally, I would like to thank Burdette Anderson of Rocky Mountain High Speed and the Trilion support team for their knowledge of high speed camera systems and the assistance they provided throughout. Last but not least I would like to thank my family and loved ones for their support.

TABLE OF CONTENTS

1. INTRODUCTION ..... 1

2. THEORETICAL BACKGROUND ..... 4

Collision Mechanics ..... 4
Strain Gage Load Cells ..... 5
Uncertainty in Load Cell Measurements ..... 6
Digital Image Correlation (DIC) ..... 8
2-D DIC ..... 9
3-D DIC ..... 10
Uncertainty in DIC Measurements ..... 11
GOM Correlate ..... 13

3. CESSNA 182B COMPONENT FIXTURE DESIGN ..... 15

Data Collection Methods ..... 15
Load Cells ..... 15
Force Calculations ..... 16
Design Considerations ..... 16
High Speed Video ..... 17
DIC ..... 18
Design Requirements ..... 18
In Flight Geometry ..... 18
Assembly and Disassembly ..... 19
Durability ..... 19
Integrated Data Acquisition ..... 19
Strut Testing Fixture ..... 20
Test Article Geometry ..... 20
Data Collection ..... 21
Final Design ..... 21
Design Validation ..... 22
Wing Testing Fixture ..... 22
Test Article Geometry ..... 22
Data Collection ..... 23
Final Design ..... 24
Design Validation ..... 26
Windscreen Testing Fixture ..... 26
Test Article Geometry ..... 26
Data Collection ..... 27
Final Design ..... 28
Design Validation ..... 31

TABLE OF CONTENTS CONTINUED

4. CESSNA 182B COMPONENT LEVEL TESTING ..... 33

Phantom 3 Drone Fleet ..... 33
Data Acquisition setup ..... 34
Load Cells ..... 34
DIC ..... 35
Measurement Uncertainty in Testing ..... 36
Launcher Characterization ..... 37
Cessna 182B Strut Impact Testing ..... 37
Data Acquisition ..... 37
Strut Testing Results ..... 39
Strut Testing Error ..... 42
Strut Testing Conclusions ..... 44
Cessna 182B Wing Impact Testing ..... 45
Data Acquisition ..... 45
Wing Nomenclature ..... 47
Wing Testing Results ..... 49
Wing Testing Error ..... 56
Load Cells ..... 56
2-D DIC ..... 57
Wing Testing Conclusions ..... 59
Cessna 182B Windscreen Impact Testing ..... 61
Data Acquisition ..... 61
3-D DIC Windscreen Nomenclature ..... 63
Windscreen Testing Results ..... 65
Windscreen Testing Error ..... 71
Load Cells ..... 71
3-D DIC ..... 73
Windscreen Testing Conclusions ..... 75
Tilted Windscreen Penetration Test ..... 77
Tilted Windscreen Testing Results ..... 78
Tilted Windscreen Testing Conclusions ..... 80

5. SUMMARY AND CONCLUSIONS ..... 82

6. FUTURE WORK ..... 88

REFERENCES CITED ..... 89

APPENDICES ..... 94

TABLE OF CONTENTS CONTINUED

APPENDIX A: Testing Launch Data .....95
APPENDIX B: Test Fixture Drawings and Material Lists.....97
APPENDIX C: Strut Testing Crash Sequences and Plots .....105
APPENDIX D: Wing Testing Crash Sequences and Plots.....108
APPENDIX E: Windscreen Testing Crash Sequences and Plots .....112
APPENDIX F: Windscreen DIC Displacement Plots .....130
APPENDIX G: Load Cell Usage and Calibration Certificates.....135
APPENDIX H: Load Cell Post Processing Codes.....141
APPENDIX I: DIC Calibration Results and Calibration Artifact Certificate.....145
APPENDIX J: Literature Review .....159

# LIST OF TABLES

Table Page

1. Sources of uncertainty and values in load cell measurement .....7
2. Summary of windscreen fixture validation tests.....32
3. Data and results from strut testing .....39
4. Sources of error in load data for strut testing and effects on results.....43
5. Damage level categories (FAA-ASSURE) [7] .....49
6. Test data and results for wing test A16-GA_0003.....49
7. Test data and results for wing test A16-GA_0004.....50
8. Sources of error in load data for wing testing and effects on results.....56
9. Sources of error in 2-D DIC for wing testing and effects on results .....57
10. Results and data from test A16-GA_0008 .....65
11. Results and data from test A16-GA_0009 .....65
12. Results and data from test A16-GA_0010 .....66
13. Results and data from test A16-GA_0011 .....66
14. Sources of error in load data for windscreen testing and effects on results.....71
15. Sources of error in 3-D DIC for windscreen testing and effects on results.....73
16. Launch data from testing .....97
17. Results from test A16-GA_0005 .....114
18. Results from test A16-GA_0006 .....116
19. Results from test A16-GA_0007 .....119

20. Results from test A16-GA_0012 .....128

21. Load cell numbering system, test usage, and equipment.....137

22. DIC equipment.....147

# LIST OF FIGURES

Figure Page

1. Wiring diagram for a Wheatstone bridge [11]. ....5

2. Stereo DIC camera setup ....11

3. THC-10k load cell specification from Transducer Tech [16]....17

4. Assembled strut attachment (left) and full test fixture (right) ....20

5. Wing attachments points on wing (left) and fuselage (right) ....23

6. Mimic strut attachment with nested load cell at c-channel (left) and mimic strut attachment at wing (right) ....25

7. Front view (left) and rear view (right) of leading edge wing attachment ....25

8. Trailing edge wing attachment (left) and assembled wing testing fixture (right) ....25

9. Windshield attachments and installation from Cessna 182 parts manual [20] ....27

10. Layout of windscreen test fixture highlighting key features ....29

11. View of stereo DIC setup from inside shipping container (left) and protective ballistic screen and window (right)....30

12. Load cell interfaces for windscreen test fixture for capturing vertical forces (left) and horizontal forces (right)....31

13. Roller bar interface between upper and lower structures (left) and fully assembled windscreen test setup with windscreen installed (right)....31

14. Phantom 3 UAV motor and arm numbering system....34

15. Wiring diagram for load cell data acquisition....35

16. Test site layout for strut testing....38

17. Load cell layout for strut testing ....38

LIST OF FIGURES CONTINUED

Figure Page

18. Impact orientation and crash sequence of UAV #10 in test A16-GA_0002 ....40

19. Damage from test A16-GA_0002 ....41

20. Load cell output from Matlab for test A16-GA_0002 ....42

21. Test site layout for wing (right) testing ....46

22. Load cell layout for wing (right) testing ....47

23. Locations and numbering system of ribs and leading edge spar ....48

24. Layout of tracking dots on wing tip from GOM Correlate ....48

25. Impact orientation and crash sequence of UAV 5 in test A16-GA_0003 ....52

26. Damage from test A16-GA_0003 ....53

27. Load cell output from Matlab for test A16-GA_0003 ....54

28. 2-D displacement tracking in x-direction for test A16-GA_0003 ....55

29. 2-D displacement tracking in y-direction for test A16-GA_0003 ....55

30. Test site layout for windscreen testing ....62

31. Load cell numbering for windscreen testing ....62

32. Interior view of windscreen with speckle pattern and tracking dots ....63

33. Point component numbering for windscreen testing from GOM ....64

34. Crash sequence from test A16-GA_0010 ....68

35. Damage from test A16-GA_0010 ....69

36. Load cell plots from Matlab for test A16-GA_0010 ....70

LIST OF FIGURES CONTINUED

Figure Page

37. Deformation series of surface component in test A16-GA_0010 ..... 71

38. Test setup for tilted windscreen penetration test ..... 78

39. Crash sequence for test A16-GA_0014 ..... 79

40. Damage from penetration test A16-GA_0014 ..... 80

41. A16-GA_0003 collision footage side by side with FE model from NIAR [27] ..... 85

42. A16-GA_0010 collision footage side by side with FE model from NIAR [27] ..... 86

43. A16-GA_0014 collision footage side by side with FE model from NIAR [27] ..... 86

44. Engineering drawing of c-channel for strut testing fixture from Capstone Technical Addendum [17] ..... 98

45. Engineering drawing of strut mount for strut testing fixture from Capstone Technical Addendum [17] ..... 98

46. Engineering drawing of spacer 1 for strut testing fixture from Capstone Technical Addendum [17] ..... 99

47. Engineering drawing of spacer 2 for strut testing fixture from Capstone Technical Addendum [17] ..... 99

48. Engineering drawing of strut fixture assembly from Capstone Technical Addendum [17] ..... 100

49. Engineering drawing of mimic strut for wing testing fixture from Capstone Technical Addendum [17] ..... 101

50. Engineering drawing of mimic strut insert at fuselage end for wing testing fixture from Capstone Technical Addendum [17] ..... 101

51. Engineering drawing of mimic strut insert at wing end for wing testing fixture from Capstone Technical Addendum [17] ..... 102

LIST OF FIGURES CONTINUED

Figure Page

52. Engineering drawing of mimic strut attachment at c-channel for wing testing fixture from Capstone Technical Addendum [17] ..... 102

53. Engineering drawing of wing to c-channel attachment at trailing edge for wing testing fixture from Capstone Technical Addendum [17] ..... 103

54. Engineering drawing of wing to c-channel attachment at leading edge for wing testing fixture from Capstone Technical Addendum [17] ..... 103

55. Engineering drawing of upper c-channel assembly for wing testing fixture from Capstone Technical Addendum [17] ..... 104

56. Engineering drawing of full wing mount fixture from Capstone Technical Addendum [17] ..... 104

57. Impact orientation crash sequence of UAV #10 in test A16-GA_0001 ..... 106

58. Damage from test A16-GA_0001 ..... 106

59. Load cell output from Matlab for test A16-GA_0001 ..... 107

60. Impact orientation of UAV #6 in test A16-GA_0004 ..... 109

61. Damage from test A16-GA_0004 ..... 109

62. Load cell output from Matlab for test A16-GA_0004 ..... 110

63. 2-D displacement tracking in x-direction for test A16-GA_0004 ..... 111

64. 2-D displacement tracking in y-direction for test A16-GA_0004 ..... 111

65. Clipping and impact orientation of UAV #11 in test A16-GA_0005 ..... 113

66. Damage from test A16-GA_0005 ..... 114

67. Load cell output from Matlab for test A16-GA_0005 ..... 114

68. Deformation series of surface component in test A16-GA_0005 ..... 115

LIST OF FIGURES CONTINUED

Figure Page

69. Clipping and impact orientation of UAV #20 in test A16-GA_0006 ..... 116

70. Damage from test A16-GA_0006 ..... 116

71. Load cell output from Matlab for test A16-GA_0006 ..... 117

72. Deformation series of surface component in test A16-GA_0006 ..... 117

73. Stills from high speed footage of test A16-GA_0007 ..... 118

74. Damage from battery in test A16-GA_0007 ..... 119

75. Load cell plots from Matlab for test A16-GA_0007 ..... 119

76. Deformation series of surface component in test A16-GA_0007 ..... 120

77. UAV #16 at beginning and middle of impact in test A16-GA_0008 ..... 120

78. Damage from test A16-GA_0008 ..... 121

79. Load cell plots from Matlab for test A16-GA_0008 ..... 122

80. Deformation series for test A16-GA_0008. The top three images show deformation #1 from motor #3 and the other images depict deformation #2 ..... 122

81. Impact orientation and crash sequence for test A16-GA_0009 ..... 123

82. Load cell plots from Matlab for test A16-GA_0009 ..... 124

83. Deformation series of surface component in test A16-GA_0009 ..... 124

84. UAV impact orientation for test A16-GA_0011 ..... 125

85. Damage from windscreen test A16-GA_0011 ..... 126

86. Load cell plots from Matlab for test A16-GA_0011 ..... 126

87. Deformation series of surface component in test A16-GA_0011 ..... 127

LIST OF FIGURES CONTINUED

Figure Page

88. Crash sequence for test A16-GA_0012 ....128

89. Damage from test A16-GA_0012 ....128

90. Load cell output from Matlab for test A16-GA_0012 ....129

91. Deformation series of surface component in test A16-GA_0012 up until first visible fracture ....129

92. DIC point locations and displacement plots for test A16-GA_0005 ....131

93. DIC point locations and displacement plots for test A16-GA_0006 ....131

94. DIC point locations and displacement plots for test A16-GA_0007 ....132

95. DIC point locations and displacement plots for test A16-GA_0008 ....132

96. DIC point locations and displacement plots for test A16-GA_0009 ....133

97. DIC point locations and displacement plots for test A16-GA_0010 ....133

98. DIC point locations and displacement plots for test A16-GA_0011 ....134

99. DIC point locations and displacement plots for test A16-GA_0012 ....134

100. Calibration sheets for load cells #0 and #1 ....137

101. Calibration sheets for load cells #2 and #3 ....137

102. Calibration sheets for load cells #4 and #5 ....138

103. Calibration sheets for load cells #6 and #7 ....138

104. Calibration sheets for load cells #8 and #9 ....139

105. Calibration sheets for load cells #10 and #11 ....139

106. Calibration sheet for load cell #12 ....140

LIST OF FIGURES CONTINUED

Figure Page

107. DIC calibration quality data for test A16-GA_0005 from GOM Correlate ..... 146

108. DIC calibration quality data for test A16-GA_0006 from GOM Correlate ..... 147

109. DIC calibration quality data for tests A16-GA_0007 – A16-GA_0009 from GOM Correlate ..... 147

110. DIC calibration quality data for tests A16-GA_0010 – A16-GA_0012 from GOM Correlate ..... 148

111. Windscreen testing fixture from NRCC report [21] ..... 161

112. Wing stand for testing from NRCC report [21] ..... 161

113. Windshield impact at 140 kts from NRCC report [21] ..... 162

114. Damage to outside of windshield (left) and inside of windshield (right) from NRCC report [21] ..... 162

115. Drone to wing slat impact during test #2 from NRCC report [21] ..... 163

116. Post test pictures of wing slat from NRCC report [21] ..... 164

117. Slat deflection post wing test from NRCC report [21] ..... 164

# ABSTRACT

Unmanned Aircraft Systems (UAS) are more attainable now than ever before. With uses ranging from re-forestation, agriculture, film-making, and recreation; a significant amount of airspace is being occupied by UAS. To better understand the risks posed by UAS to other aircraft, the Alliance for System Safety of UAS through Research Excellence (ASSURE) was created. One aspect of ASSURE's agenda is to conduct air to air collision studies using Finite Element Analysis (FEA) in combination with full scale collision data.

Montana State University contracted with ASSURE to conduct component level testing for the project, and provide data for validating FEA models being developed at the National Institute of Aviation Research (NIAR). Component level testing consisted of the following aircraft components: Cessna 182B struts, wings, and windscreens. In order to accurately simulate in-flight geometry, fixtures were custom fabricated to individually mount aircraft components. High velocity impact data was collected via load cells, high speed video, and Digital Image Correlation (DIC).

A drone launching system developed during an MSU conducted research effort was used to launch Phantom 3 quadcopter UAVs as projectiles for component level tests. For all tests, the impact was captured from two viewpoints using high speed video, and reaction force data was collected using load cells at critical attachment points. For wing and windscreen testing, 2-D DIC and 3-D DIC were used respectively to capture displacements during the collision. Testing showed that struts received mainly superficial damage, but that both wings and windscreens exhibited the potential for catastrophic failure.

# INTRODUCTION

Unmanned aerial systems (UAS) are the fastest growing branch of aviation, continuing to grow in numbers, complexity, availability, and applications year to year [1]. According to the Drone Market Report 2020, the global drone market is expected to grow from $22.5 billion in 2020 to $42.8 billion in 2025 [2]. Given the affordable price, ease of use, and access to UAS it is no surprise that civilian owned UAS now occupy a significant amount of shared airspace. While drones have been beneficial in many ways, some of the unintended consequences include: interruption of airport activities, wildfire fighting operations, medical helicopter flights, and escalating civil unrest situations to name a few [3].

In order to keep track of drones and mitigate dangers, the FAA has created the "Federal Aviation Administration Reauthorization Act" which requires registration of all drones both commercial and civilian [4]. Additionally, general rules for operating UAV can be found on the FAA's website to help ensure safe operation [5]. When the guidelines are followed, drones pose little risk. Unfortunately, there will always be users who don't comply with the guidelines, potentially creating dangerous situations. One area of concern is the risk of air to air collisions between drones and manned aircraft both private and commercial. To assess the dangers posed by UAS to aircraft, the Alliance for System Safety of UAS through Research Excellence (ASSURE) was created.

ASSURE's mission is to provide the research needed in order to safely and quickly incorporate UAS into our National Airspace System with minimal changes to the system already in place [6]. In order to evaluate the severity of an air to air collision,

impact testing of aircraft components is required. However, conducting full scale impact testing is very expensive both fiscally and temporally. Due to this, a combined approach involving finite element analysis (FEA) and full scale testing is being used. This involves the creation of highly detailed finite element models of UAS and aircraft of interest. By assembling models virtually, a variety of crash scenarios can be simulated and compared with the data collected from full scale testing. If the model performs the same as full scale tests, then it can be confirmed and used to study additional crash scenarios without the need to conduct more full scale tests.

The National Institute of Aviation Research (NIAR) at Wichita State University is the ASSURE team member tasked with developing and overseeing model creation. As part of their work, a finite element model for a Cessna 182 single prop plane has been created for analysis. This work involves reverse engineering of all plane components, assembling and defining components with contact boundaries, incorporating material models into components, and comparing model results with full scale testing results. Additionally, a reverse engineered model for a DJI Phantom 3 quadcopter style drone has been created by NIAR to be used as the impactor in these simulations [7]. The Phantom 3 drone was chosen based on previous research done at Montana State University (MSU) to select representative UAS models [8].

Montana State University has been tasked with assisting in the collision studies between Cessna 182 planes with phantom 3 drones. In previous work done at MSU, a material model for C-182 windscreens was developed in LS-DYNA, along with a test facility capable of accurately launching phantom 3 UAVs at take off and landing

velocities [9]. The work presented here picks up where previous work left off, focusing on fixture development for component level testing of C-182 parts and full scale test results.

In order to provide useful data for model validation, test fixtures representative of in flight conditions were required. Components to be tested included wing struts, wings, and windscreens. Using the fuselage of a retired C-182B plane for reference, component geometry, connections, and contact points had to be re-created in test fixtures. In order to provide relevant data for model validation, fixtures needed to be easily modified and incorporate various data collection methods including high speed video, force transducers, and digital image correlation (DIC). Test fixtures for struts, wings, and windscreens were developed to meet these requirements and 3-D modeled using computer-aided design (CAD).

Full scale testing was performed with a combination of high (120 knots) and low (80 knots) velocity shots. Two strut tests, two wing tests, and ten windscreen tests were performed in total. High speed video and reaction forces were captured for each test, and 2-D wing tip displacement data and 3-D windscreen displacement data was collected for wings and windscreens respectively. Upon completion of testing, data was processed and shared with NIAR for use in model validation.

# THEORETICAL BACKGROUND

## Collision Mechanics

Collision mechanics describe the event of two objects colliding and are in large an application of Newton's laws of motion. In collision studies, we are generally interested in the impulse or change in momentum associated with an object as it collides with another and the reaction forces as the other object pushes back. In order to cause a change in momentum, a force must be applied over a given amount of time [10]. To find the impulse of a collision, we simply start with Newton's 2nd Law (equation 1) and insert the definition of acceleration (equation 2). Rearranging, we can see that impulse is equal to mass times the change in velocity (equation 3). Further rearranging, we can find the force applied to the object that caused the change in momentum in terms of mass, change in velocity, and duration time of impact (equation 4). In a real world collision, this force is a function of time and this equation assumes a constant force. However, it is still a useful metric for estimating the amount of reaction forces that might be expected when designing an experimental setup.

$$F = m * a \tag{1}$$

$$a = \frac{\Delta v}{t} \tag{2}$$

$$F * t = m * \Delta v \tag{3}$$

$$F = \frac{m * \Delta v}{t} \tag{4}$$

## Strain Gauge Load Cells

Strain gauge load cells work by converting a physical deformation of the measuring surface of the load cell into an electrical signal via strain gauges attached to the surface. Strain gauges work by detecting a small linear change in resistance when a strain is applied [11]. In order to measure this change in resistance more accurately, strain gauge load cells commonly use four strain gauges arranged in a Wheatstone bridge. A Wheatstone bridge is a series of 4 known balanced resistors with an applied voltage ($V_{EX}$) and a measured voltage ($V_o$) as seen in figure 1 below.

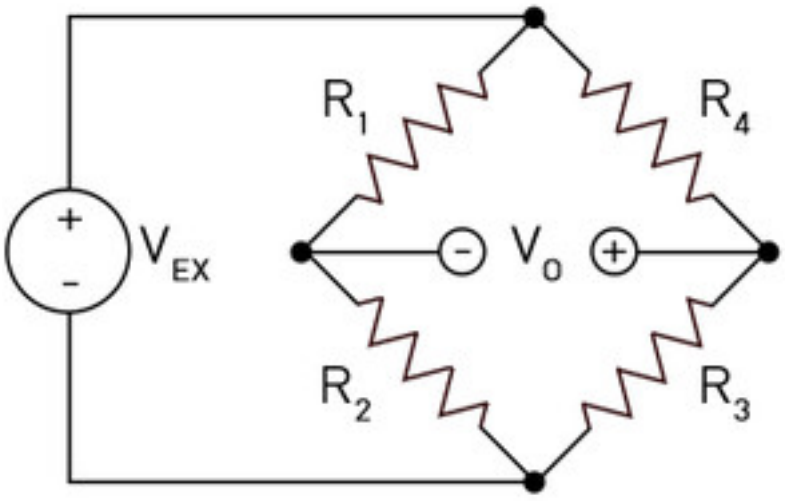



Figure 1. Wiring diagram for a Wheatstone bridge [11].

Using Ohm's Law (equation 5), and applying it to the four legs of the Wheatstone bridge above, we can find $V_o$ in terms of the other variables as seen below (equation 6). In terms of a load cell, the resistors in the Wheatstone bridge correspond to the strain gauges [11]. By measuring the change in voltage from change in resistance in the strain gauges, we can solve for the force applied since it is proportional to change in voltage.

Using equation 7 below where *C* is the output in mV/V of the load cell at full load and *L* is the full load capacity of the model we can calculate force.

$$V = I * R \tag{5}$$

$$V_o = \left[\frac{R3}{R3+R4} - \frac{R2}{R1+R2}\right] \times V_{EX} \tag{6}$$

$$Force = \frac{V_o \times L}{C \times V_{EX}} \tag{7}$$

Uncertainty in Load Cell Measurements

When calibrating a strain gauge load cell, there are several metrics calculated that represent the uncertainty in measurements made with that load cell. Calibration certificates come with each load cell and list these values. Details are given below.

- Temperature. Inconsistent temperature can impact a strain gage load cell's sensitivity thus introducing error into the system. This source of error is generally quite small compared to other uncertainty sources, but is worth considering if operating in extreme temperatures.
- Non-linearity. Non-linearity is essentially a measure of a load cells weighing error over its entire operating range [12]. It is a factor that affects all strain gage load cells, and must be considered for accurate measurements. It is listed as a percent of the rated output of the load cell, and is unique to each load cell.
- Hysteresis. Hysteresis is the difference between load cell readings for the same applied load, one measurement taken from ascending to the load from 0 and the

other from descending to the load from the load cells maximum [12]. Hysteresis error functions similar to nonlinearity, and can be calculated in the same manner.

- Non-repeatability. Non-repeatability is the maximum difference between load outputs from identical loading conditions [12]. Similar to non-linearity and hysteresis, it is a percent function of a load cells rated output and its associated maximum error can be found with the same method.

All of these sources of uncertainty are specific to the individual load cell and are found through calibration. They each provide a different view of the error associated with a given measurement. To determine the maximum uncertainty due to the load cell itself, you simply use the largest value from either non-linearity, hysteresis, or non-repeatability. Error in load measurements depend on not just the measurement error of the load cell, but also on the sensitivity and accuracy of the measuring device, power supply, and the random noise present in the results. Sources of uncertainty in load measurements are outlined in table 1 and discussed below.

Table 1. Sources of uncertainty and values in load cell measurement.

| Source of Uncertainty | Value |
|---|---|
| Load Cell | Specific to each load cell |
| DAQ Uncertainty | 0.174 mV |
| Power Supply Uncertainty | 0.1% of R.O. |
| System Noise | Quantified for each test |

To quantify the error present in the DAQ used for testing, values from the National Instruments (NI) 9205 spec sheet [22] were cited. The spec sheet lists the accuracy at full scale to be 0.174 mV. Another source of uncertainty in load cell measurements is due to the power supply. During testing, a BV Precision 1672 power supply was used to provide a DC current to the load cells. The datasheet for this power supply lists the accuracy as 0.1% of the output, which was 10V for all tests [26]. The other main source of uncertainty in the DAQ system is the noise present from random electromagnetic interference (EMI). This is quantified by performing statistical analysis on the load cell testing data pre-impact, and is unique for each load cell. With the noise band quantified at three standard deviations, a value for the total combined uncertainty in the measurement can be calculated using a root sum of squares approach. In this manner, uncertainty in the load cell is combined with uncertainty in the DAQ measurement along with supply voltage uncertainty and noise in the system to create bounds for each load cells' results for each test.

## Digital Image Correlation (DIC)

Digital image correlation is a method of using optics to measure the changing full-field 2-D or 3-D coordinates of a surface during a mechanical test [13]. Using the measured coordinate, various quantities of interest can be calculated such as displacement, velocity, acceleration, stress, and strain to name a few. DIC can be used to characterize deformations in a number of different materials since it is a no-contact method. Some of these materials include metals, polymers, biological tissues, and even explosives. DIC can also be applied to surfaces of greatly varying sizes ranging from

small tensile testing coupons to entire heavy machinery assemblies [13]. In order to track the coordinates of a test piece, there must be some kind of pattern on the surface. Tracking patterns can range from tracking dots in the form of stickers that are specially designed to work with a specific DIC software, to a random speckle pattern applied to the surface with paint. Size of the tracking dots or speckling pattern is determined by the application and resolution of the setup. In general, dots in a speckle pattern should be three to five pixels across for best tracking results [13]. One of the fundamental assumptions for DIC measurement is that the pattern on the surface being measured follows the surface as it deforms [13]. By doing so, images can be correlated to form full field coordinates for the duration of the test. For both types of DIC, calibration photos containing an object of known length must be taken prior to testing.

2-D DIC

2-D DIC is used to capture motion only in the x-y plane. As a result, multiple perspectives are not needed and it can be performed with only one camera. In 2-D testing, calibration can be as simple as inputting a measured distance between two points in an image for reference. Using this distance as the reference, DIC processing software can then calculate the change in coordinates as a distance. It is important for 2-D DIC measurements that the test article be perfectly in plane with the camera lens, otherwise out of plane motion will introduce error into measurements. Due to this, 2-D DIC is applicable primarily for scenarios where thinning, buckling, or rotations are not expected otherwise additional error will be induced [13]. For this reason, 3-D DIC should always be used when and high accuracy results are needed.

3-D DIC

3-D DIC is used to capture motion in x-y-z. In order to do this, two cameras must be used in stereo, focusing in on the same field of view from different angles. The setup for 3-D DIC can be seen in the figure below. The two cameras share a common trigger resulting in two sets of images with identical time stamps. In order to calibrate a stereo DIC system, a series of images must be taken with a high precision calibration artifact. The amount of images in the series and the orientation of the calibration artifact for each image varies for the type of artifact. In general, 16-24 images are taken where the artifact is rotated for each picture and angled in various directions. The calibration artifact typical consists of a series of dots where the distance between them is known to a high degree of certainty. By inputting the type and model of calibration artifact into the DIC software, the system can then use the series of calibration images to define a 3-D scale.

A good calibration is critical for obtaining accurate results, and should be repeated until a calibration within the software's requirements is achieved. Calibration quality is quantified usually with two values, scale deviation and calibration deviation. Scale deviation refers to known distances between coded markers on the calibration artifact. Using the series of calibration images, these distances are calculated, averaged, and compared to the known distance on the artifact. The difference between the measured and actual values is quantified and listed as scale deviation. Calibration deviation is a metric listed in pixels, and is essentially the error associated with the calibration [14]. Both of these metrics mainly indicate whether or not the calibration was successful. The threshold for a successful calibration may vary between experimental setups, and it is sometimes up to the user to determine whether or not the calibration is of

sufficient quality for the experiment. Although these metrics have to do with error, they provide only an estimate of the quality of calibration, and subsequent uncertainty analysis is required to determine the baseline error of the system.

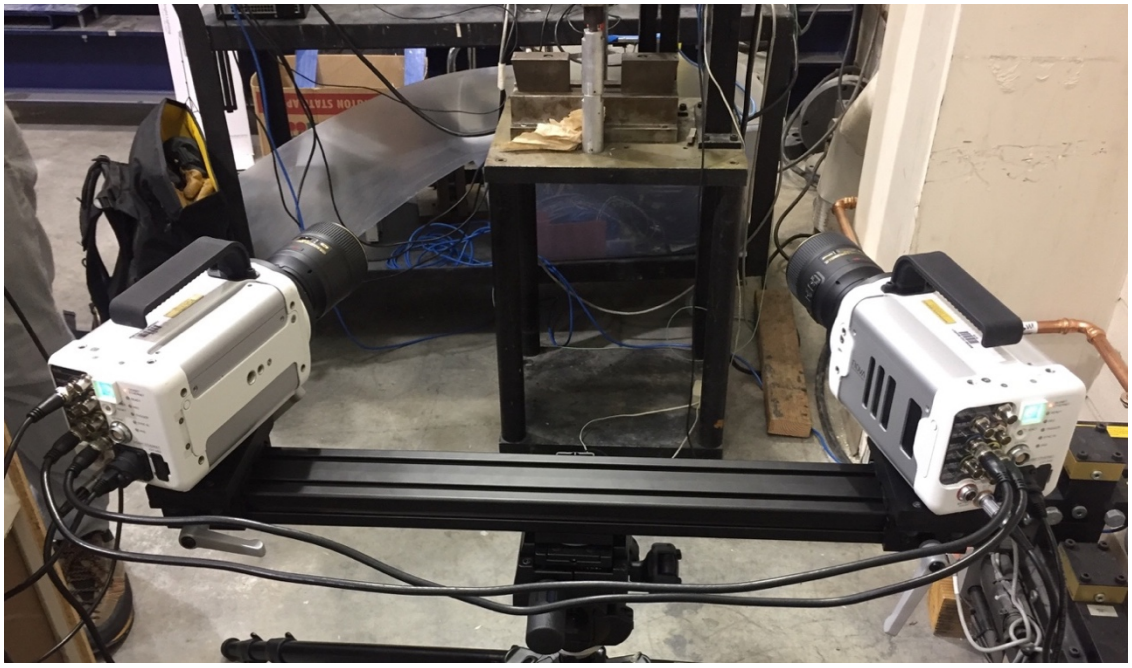


Figure 2. Stereo DIC camera setup.

Uncertainty in DIC Measurements

Uncertainty in DIC measurements is typically broken up into two types: variance (noise) errors and bias errors. Variance errors are random errors with a mean about the true value of the quantity of interest (QOI). Uncertainty due to bias refers to an offset of the mean from the real value of the QOI [13]. The primary sources for uncertainty in DIC measurements are due to cameras noise and matching errors while correlating images (stereo).

Variance errors can be found by performing statistical analysis on the noise floor of the system. To do this, a series of images must be taken of the surface of interest prior

to performing the test. It is critical that the test setup for these images is identical to the final testing setup. Therefore, the best way to do this is to take 10-20 frames from the test sequence when it is known that the surface is completely stationary. Using the displacement values for a series of points on the surface, the standard deviation of the values can be found. As outlined in the DIC Good Practices Guide [13], standard deviations for each point can be found and averaged both temporally and spatially. It is up to the user to determine which metric to use for uncertainty quantification and the confidence interval that is meaningful for the experiment. Common approaches are to either use whichever value is higher between temporal and spatial deviation, or to average the two values together and use that. Typically, variance errors in the x and y directions are similar, and the higher value should be used for both. Motion in the z direction usually has the higher uncertainty in measurements. Even if the images used for variance error evaluation are from directly before motion in the test, it still may not be fully representative of the errors present during the test. As a result, variance error is typically presented as the minimum error associated with a measurement rather than the true uncertainty [13].

Bias errors are generally difficult to quantify due to the fact that the true value of the QOI is rarely known. The DIC Good Practices Guide [13] outlines a few ways to quantify bias errors, but they do not fully explain all bias error that could be present in the experiment. The main approach to quantifying bias error is to take the mean value of the QOI in the images taken for uncertainty analysis and see if they change over time. If the mean is found to be changing over time, this could indicate a bias due to camera drift,

heating of the camera, or vibrations to name a few [13]. Another source for bias error could be due to uncorrected lens distortions. This type of error will show up as an elliptical shape in strain (or displacements if the mean value has been subtracted for the images) plots and is usually lower in the center of the field of view and higher at the edges. In 2-D DIC, bias error due to out of plane motion needs to also be evaluated. This is done by determining the QOI as a function of rotation. For rigid body motion, strain for example should be zero throughout the test and any value indicated is due to a combination of noise and bias error. This in turn can be compared to the baseline system noise, and should be noted if similar of greater [13]. Once again, these are just some of the ways to try and quantify bias errors. In reality, there is likely bias error whether or not it is detected.

## GOM Correlate

GOM Correlate is a comprehensive DIC processing software. It is used to process images captured in testing and turn them into meaningful results. By recognizing and interpreting a pattern on the surface on interest in an experiment, various quantities such as displacement, velocity, acceleration, stress, and strain can be calculated. GOM achieves this by comparing the image series captured during testing in combination with using calibration data for reference and scale. Calibration is accomplished by taking a series of images of a precision engineered GOM calibration artifact as outlined earlier. Using specialized GOM tracking dots or a surface pattern, the software can calculate a quantity of interest and present data over time or at each stage in the project. In order to calculate values across an entire surface, the software interprets the random speckled

pattern to create square overlapping facet points across the surface [15]. Values at locations between facet points are interpolated based on the surrounding point values. The size and distance between facet points is important in that it determines the resolution of the area of interest. For best results, the smallest facet size that yields a complete surface should be used. Specifications for speckle pattern size and additional information can be found in the GOM Correlate manual [15].

# CESSNA 182B COMPONENT FIXTURE DESIGN

Fixture design was an important aspect of conducting component level impact testing. Well thought out designs were essential to collecting data that would be useful for model validation and collision severity analysis. Several undergraduate researchers along with a senior capstone group were tasked with working on the design and fabrication of test fixtures. This chapter focuses on the design challenges faced and the design and fabrication of fixtures for testing.

## Data Collection Methods

In order to provide accurate data for use in FE model validation, relevant reaction forces, displacements, shot speed, and UAV impact conditions needed to be captured. To do this, varying combinations of load cells, DIC, and high speed video were used to collect data for UAV to C-182B component impact testing.

### Load Cells

To determine reaction forces between the backstop at the test facility and the test article fixtures, load cells were required. In order obtain results with minimal uncertainty, load cells needed to have a high enough capacity to avoid overloading, but not so high that unnecessary resolution error is introduced. In order to choose optimum load cells for testing, an estimate of the forces transferred through the structure was needed.

Force Calculations. To estimate the reaction forces present in a UAV collision, a basic physics approach was used to analyze a collision with a flat plate. Based on examination of videos during launcher development, it was determined that a Phantom 3 UAV collision with a flat steel plate has a duration of about 0.003 s. Using the speed recorded from high velocity launcher testing of 220 ft/s (130 knots) as an upper bound for velocity, and a Phantom 3 average mass of 2.6 lbm, force was calculated using equation 4 in the background information section. Assuming that all kinetic energy from the drone is transferred to the plate, the impulse required for that change in momentum is equal to 6000 lbf applied over 0.003 s. This value is based on the assumption that the force applied during the collision is constant, but in reality the force applied will increase over time, peaking as the center of mass of the drone reaches the plate. Interpreting this force value as an average for the collision, it can be doubled to obtain a rough estimate of the peak load, resulting in about 12,000 lbf at peak. Now with an estimate for the upper limit on peak loads, other design considerations needed to be addressed for load cell selection.

Design Considerations. In order to be used in a variety of test setups, load cells needed to be easily attached and removed. Additionally, load cells needed to provide accurate results if subjected to off-axis loading. Given this, uniaxial through hole donut style load cells were chosen. The advantage of using donut style load cells over other designs is that they can be easily attached and pre-loaded with a bolt to capture oscillations in the data. To capture reaction forces, load cells could simply be sandwiched between the fixture and the backstop at its attachment points and bolted in. At a minimum, two load cells would be used in a test for a simple fixture with two

attachment points. Given that force would be distributed between the attachment points, Transducer Tech THC-10k load cells with a 10,000 lbf limit were chosen for use in strut and windscreen testing. With a safe overload capacity of 15,000 lbf, a load cell would be safe in the unlikely scenario that all of the drone's kinetic energy be dropped onto a single cell. The maximum inner diameter for this model, 5/8" was chosen to withstand any shear forces present. In order to capture reaction forces, fixtures needed to be designed to interface with these load cells. Load cell geometry can be seen in figure 3 below.

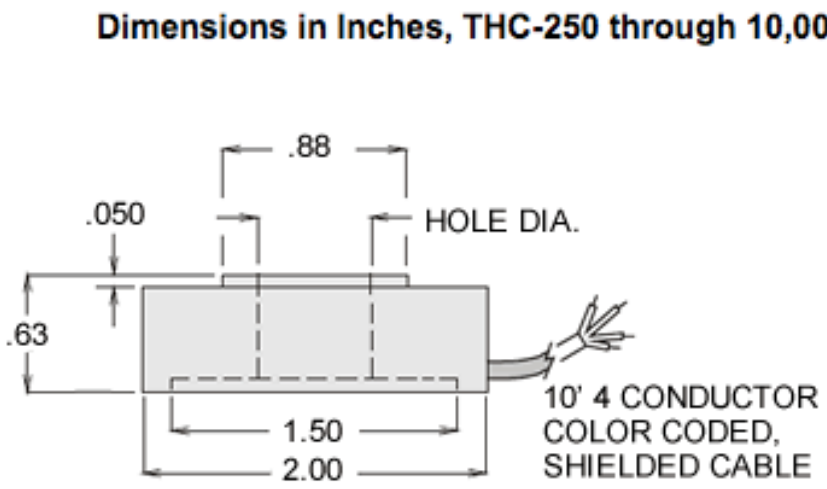



Figure 3. THC-10k load cell specification from Transducer Tech [16].

High Speed Video

To determine the velocity of the drone, its orientation at impact, and the collision itself, implementation of high speed cameras was required. Setup for velocity measurement consisted of a camera perpendicular to the drone's path used in conjunction with a speed board of known length. Footage of the collision was captured from an

oblique angle to the target, thus providing an additional view of the collision for use in determining impact orientation. Depending on availability, a variety of cameras ranging from the Photron NOVA S6, Photron Fastcam Mini UX100, and Fastec TS3 were used. To allow for high speed video collection, fixtures had to be designed so that camera views were unobstructed.

### DIC

To capture displacements during testing, 2-D and 3-D DIC was used with one camera and two cameras (stereo) respectively. The NOVA S6 cameras were used for DIC and along with high power LED lights when needed. Setup for DIC cameras varies for 2-D and 3-D DIC along with the quantity of interest. As a result, fixture designs were to incorporate spatial and safety requirements for the cameras pending on the component being tested.

## Design Requirements

### In-Flight Geometry

In order to evaluate the severity of an air to air collision and collect meaningful data for model validation, it was crucial that the fixtures be representative of the in flight geometry of the aircraft. Examination and measurement of a retired Cessna C-182B airplane provided measurement data at component attachments. Fixtures being authentic to in flight orientation was deemed a critical design requirement during development. In order to not overcomplicate the test setup, other in flight conditions such as aerodynamic

wing loading were ignored. Additionally, for testing and fixture design it was assumed that the drone was flying parallel to the planes longitudinal axis.

Assembly and Disassembly

Another important design requirement in fixture design was that fixtures needed to be easily assembled and disassembled by three team members and weight less than 300 lbm for safety. In order to conduct tests, a minimum of three personnel was required on site. Given this, components of the fixture could not be overly heavy, and setup could not be so intensive that three people could not assemble in a reasonable amount of time. Additionally, in order to test components from both the left and right sides of the aircraft in the same day, fixtures needed to be modular, easily reversible, and interface with the pre-existing I-beams attached to the test facility's backstop.

Durability

Due to the large forces present in UAV impact testing, fixtures needed to be rigid, strong, and withstand at least fifty test cycles without fatigue or failure. To achieve this, ASTM A36 hot rolled steel was predominantly used in fabrication.

Integrated Data Acquisition

Lastly, another critical design requirement was that the various systems for data acquisition be integrated into the design. Data collection methods vary for each component, and each fixture presented its own challenges for how and where data was collected. Fixtures needed to allow for data collection while also adhering to in flight geometry requirements and safety requirements for the equipment.

With these design requirements in mind, struts, wing, and windscreens were studied and custom test fixtures were modeled, designed, and fabricated to be validated for use in testing.

## Strut Testing Fixture

### Test Article Geometry

In order to meet the design requirements for fixture design, two C-182B struts (left and right) were purchased to be used in testing and to provide measurements for design. Upon inspection of the strut and its attachment points on the fuselage and wing, it was noted that a ½" pin connection was used at both attachments to hold the strut in place. Further inspection of the attachments showed that a 4° angle was present on the ends of the strut to enable it to nest properly at its attachment points. Due to this angle, attachments needed to incorporate this angle into the design to allow a flush connection with the I-beams. Figure 4 below shows the strut end attachment and full test fixture.

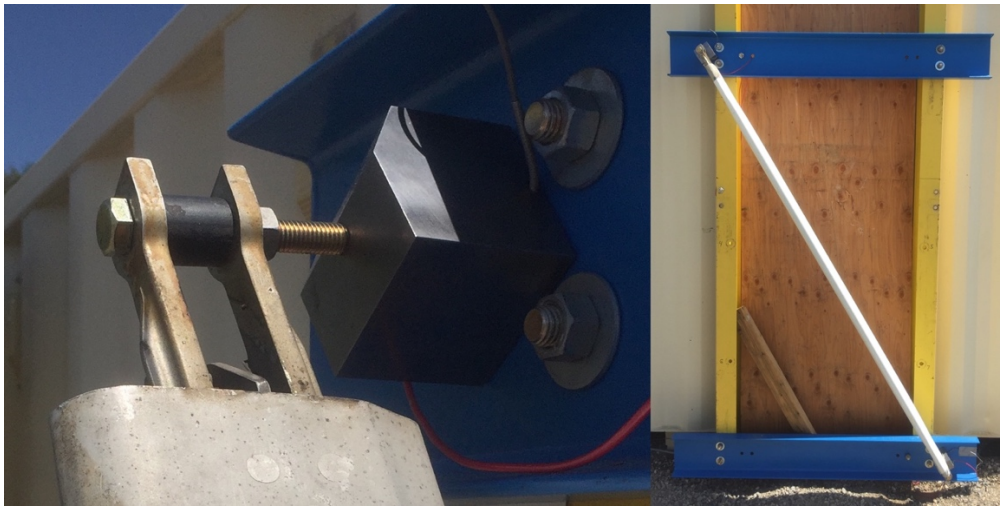


Figure 4. Assembled strut attachment (left) and full test fixture (right).

Data Collection

For strut testing, data to be collected included reaction forces at the attachment points and high speed footage of the collision. Reaction forces were to be collected at the attachment points via two of the THC-10k load cells outlined earlier. Load cells were to sit between the face of the I-beams and the attachment to the strut.

Final Design

Considering all design requirements, it was decided that the strut would span vertically between the two I-beams as seen in figure 4. The angle of the strut in the fixture was not representative of its angle on a full assembled plane, but this requirement was not deemed essential for strut testing. Load cells were to be nested into a machined block of steel with a 5/8" hole tapped into it for fastening and pre-loading the cells to the backstop. To attach the strut to the I-beams, two c-channels were placed horizontally between the I-beams and the strut attached to the c-channel. Several designs were considered for incorporating the 4° angle at the attachment. A hole tapped at a 4° angle into the load cell attachment housing was the most durable design which also incorporated the plane's geometry. This design however, meant that the pin connection used to secure the strut on the plane would not work here. Instead, a hard bushing was placed between the forks of the strut end and a bolt was threaded through and fastened to the angled tap. A nut was then used to secure the strut to the bolt. Figure 4 illustrates the final design. Additional engineering drawings and material lists for strut fixture components can be found in Appendix B.

### Design Validation

With the strut fixture design finalized, validation of the design was required before testing could begin. Prior to manufacturing, FEA was performed on the fixture's model in SolidWorks to evaluate any weak points [18]. No failures or major stress concentrations were detected when a 10,000 lbf was applied to the center of the strut. Once manufacturing had been completed, the full fixture was assembled at the test site to confirm load cell response and proper tolerances in the fixture. Load cell operation was confirmed by first applying a force to the strut and measuring the response. The setup was then further confirmed by replacing the strut with a 2x4 on the fixture and impacting with a junk drone to check functionality of the high speed data acquisition system. With the design confirmed and functioning as intended, the fixture was ready to be used in testing.

## Wing Testing Fixture

### Test Article Geometry

To fabricate a wing testing fixture representative of a flight worthy plane, C-182B wings purchased for testing were measured and characterized. The wings are attached via two ½" pin connections at its base, and two ½" pin connections for the strut on the wing and body of the plane. With the strut being an essential support for the wing, it would need to be in place during the testing sequence. However, due to the expense of struts and to simplify the fixture's geometry, a mimic steel strut was used in its place during the test sequence. Given this, fully characterizing strut geometry was critical to recreate the strut connection to the plane and wing. Again the most challenging geometry

to recreate was the 4° angles on the strut attachments. All distances between attachments on the plane were measured and were recreated on the fixture. Wing attachments and the wing strut attachment can be seen in figure 5 below.



Figure 5. Wing attachments points on wing (left) and fuselage (right).

Data Collection

For wing testing, data collected included reaction forces at all attachment points (wing and mimic strut), 2-D DIC for deflections at the wing tip, and high speed footage of the collision. Reaction forces were collected at the attachment points via three of the THC-10k load cells outlined earlier. Load cells sat between the face of the same c-channels used for the strut fixture (relocated) and the attachments to the wing and strut. Due to the geometry of the wing connections, its attachments experienced compressive forces on the trailing edge side and tensile forces on the leading edge side. In order to use the compression only load cells, a special attachment was developed for the leading edge. Due to the geometry of the strut, it too experienced both compressive and tensile forces during testing. However, due to the smaller magnitude of forces expected at the

mimic strut attachment, the load cell was simply preloaded to half capacity, allowing for movement in either direction. No special accommodations were required for collection of 2-D DIC and high speed footage.

Final Design

To integrate load cells into the attachment points, a similar approach to the strut attachments was used. A wing connection matching the fuselages was machined out of steel for both connections along with one that mimicked the struts connection. The strut and trailing wing edge's mount contained a slot for the load cell to nest in to, and a tapped hole for a 5/8" bolt to fasten everything to the c-channel. In order to integrate a load cell into the leading edge attachment, a different design needed to be used since it would undergo tension as the wing tip deflects. The load cell was instead placed behind the c-channel and connected to the bolt fastening the attachment in place. By doing so, tension and compressive forces were collected at their respective attachments. To use in place of an actual wing strut, a steel square tube was used to support the wing. Machined steel inserts recreated the geometry at the strut ends and were inserted and attached to the steel tube with ½" precision pins. Figures 6-8 illustrate the final design. Additional engineering drawings and material lists for wing fixture components can be found in Appendix B.



Figure 6. Mimic strut attachment with nested load cell at c-channel (left) and mimic strut attachment at wing (right).

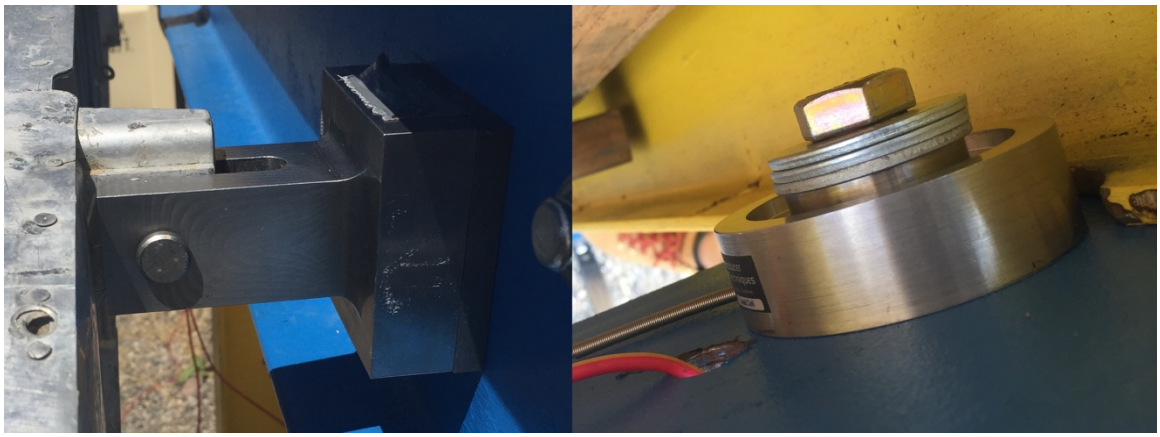


Figure 7. Front view (left) and rear view (right) of leading edge wing attachment.



Figure 8. Trailing edge wing attachment (left) and assembled wing testing fixture (right).

### Design Validation

Two THD-50k load cells [19] were purchased to be used at the wing attachments. These load cells are identical in shape to the THC-10k load cells, only larger in diameter and having a capacity of 50,000 lbf. Minor changes were made to the wing attachment designs to accommodate the larger diameter load cells. Load cell fit and response was confirmed during setup, and the fixture was ready for full scale wing testing.

## Windscreen Testing Fixture

### Test Article Geometry

To begin designing a fixture for windscreen testing, the geometry of the windscreen and its orientation during flight needed to be determined. During cruise, a C-182B plane has an angle of attack of roughly 2°-4° measured at the top center of the wing instance. This angle was recreated in the fixture to match the in-flight geometry and all of the necessary components for securing a windscreen were acquired. The windscreen is attached by slots that the top and side edges nest in to, and is secured by a retaining strip that rivets down the front edge of the windscreen between it and the nosecone of the plane. To ensure a snug fit, silicone was inserted into the slots during installation. Windscreen dimensions were taken from a new C-182B windscreen and were used in combination with fuselage measurements to recreate the fit. An original C-182B nosecone and retaining strip were purchased for use in the fixture. It is worth noting that there is slight variation in the sizes of Cessna windscreens and will sometimes need to be trimmed in order to fit the aircraft. Measurements for fixture design were taken from the

windscreen that was in hand at the test facility. Windscreen attachments and installation can be seen in figure 9 below.

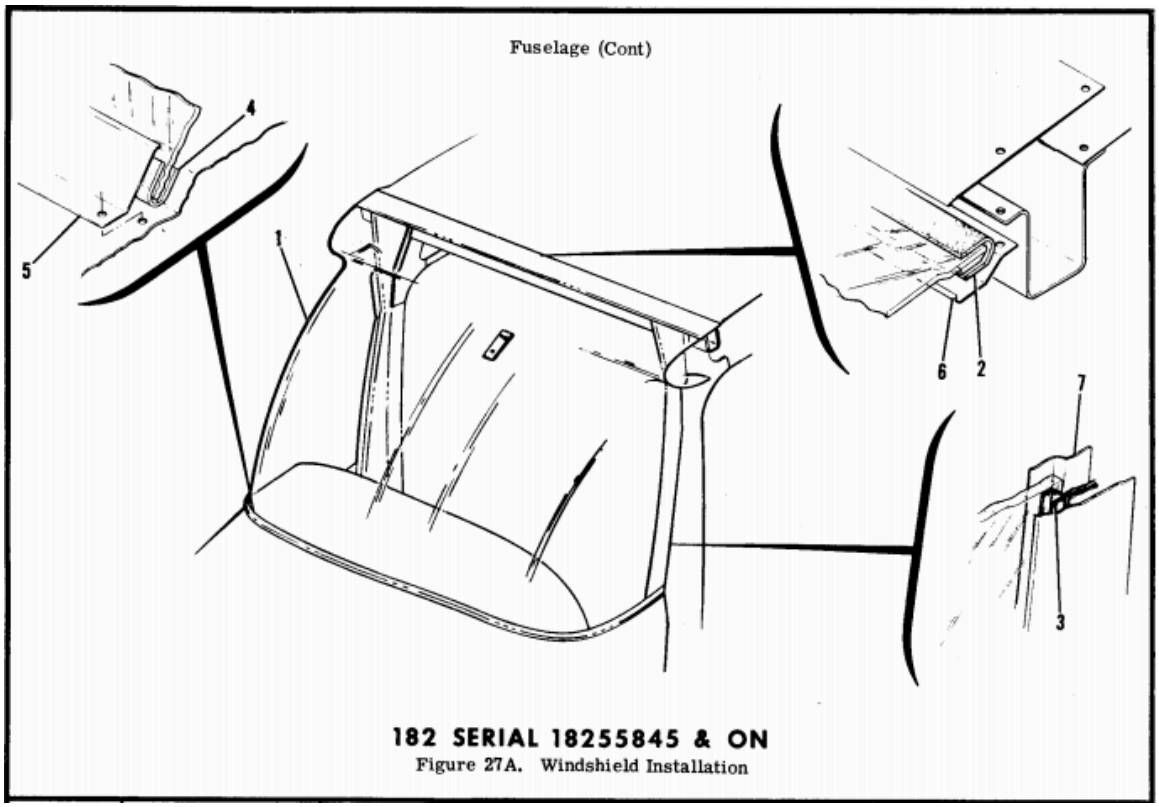



Figure 9. Windshield attachments and installation from Cessna 182 parts manual [20].

Data Collection

For windshield testing, data collection included high speed video, load cells for reaction forces, and 3-D DIC for windscreen displacements. High speed video was collected in the usual manner, and required no special arrangements from the fixture. In order to capture reaction forces, load cells were placed at every attachment to the backstop and at every interface of the fixture to the ground. In order to accurately collect reaction forces at the ground, the fixture's connections were designed to remain centered and flat on the load cell measuring surface. To collect 3-D displacement data with DIC,

the fixture was designed to allow an unobstructed and perpendicular view of the windscreen from two high speed cameras. Due to the amount of light required for capturing high speed video at 50,000 fps, the fixture incorporated high powered LED lights to illuminate the windscreen from behind. Lastly, the fixture and setup required safety precautions to protect the camera system from debris during the collision. All data collection requirements were integrated into the final design.

Final Design

The final design for the windscreen testing fixture was made up of an upper and lower section. The upper section consists of a right angle frame with a C-182B nosecone mounted along with slots that the windscreen's upper and side edges nest into. The orientation of the nosecone and slots was designed to match the geometry of the fuselage measured. To secure the windshield, a retaining strip secures the lower edge to the fixture with fasteners. Additionally, silicone caulk with similar properties to that used on actual Cessna planes was used under the retaining strip and in the slots to ensure a tight fit and successful load transfer. The upper fixture interfaces with the backstop via four 5/8" bolts at each corner of the vertical component's backside. To capture horizontal reaction forces, load cells were to be placed at each of these attachments. To support the upper structure from below and reduce binding at the bolts, the lower structure consists of a table with adjustable leg heights. To capture horizontal reaction forces, load cells would be placed under each of the four table legs. The lower fixture's legs consist of steel tube with 1 ½" nuts welded at the bottom and sections of 1 ½" all thread that allows the table leg height to be adjusted for each leg. The load cell side of the all thread was machined

to have a raised surface to nest inside the hole of each load cell, and a flat surface to fit flush to the measuring edge. To create rigid boundary conditions, concrete pads were set into the gravel at the test site for each table leg. To connect the upper and lower fixtures without restricting motion, two steel roller bars were placed between the two halves on hardened steel sections fastened to the steel tube frame. The design can be seen in figure 10 below.

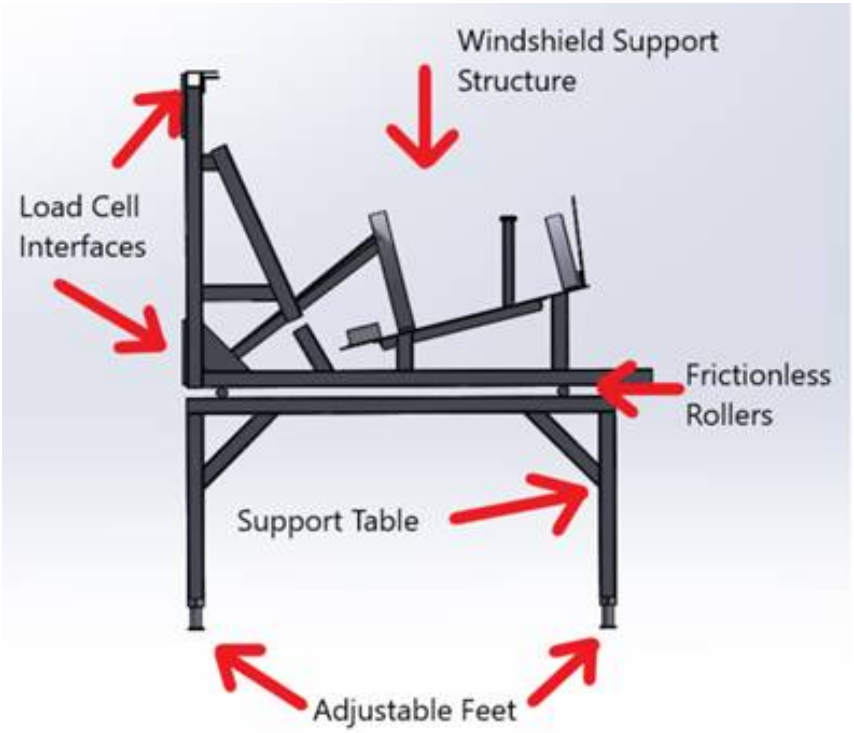



Figure 10. Layout of windscreen test fixture highlighting key features.

The stereo DIC setup was incorporated into the fixture by leaving the behind of the windscreen open to ensure the camera's views were left unobstructed. A window was cut into the test facility backstop (shipping container) to allow cameras to be mounted inside. Window size was determined using the distance from the cameras to the windscreen and the field of view size. A tripod mount and camera bar were mounted to

the floor of the shipping container for the cameras. In order to ensure camera safety, a 3/8” cast acrylic ballistic shield was secured to the outside of the window for testing. As an additional protective measure, a heavy steel plate was positioned 36” in front of the fixture to block a low shot from skidding under the fixture and into the window. The back of the windscreen was illuminated by the two high powered LEDs detailed earlier, which were mounted above the cameras. Reflections from the lights to the camera lenses were stopped using a simple cardboard shield. The stereo DIC fixture and full windscreen test fixture details can be seen in figures 11-13 below.



Figure 11. View of stereo DIC setup from inside shipping container (left) and protective ballistic screen and window (right).




Figure 12. Load cell interfaces for windscreen test fixture for capturing vertical forces (left) and horizontal forces (right).



Figure 13. Roller bar interface between upper and lower structures (left) and fully assembled windscreen test setup with windscreen installed (right).

Design Validation

The windscreen testing fixture was fabricated, and the design and geometry of the fixture was confirmed from a full setup with load cells and a windscreen in place. Two different tests were conducted to confirm the functionality of the load cells and the DIC

system with the design. A new upper fixture was constructed, allowing test pieces to be mounted at a 45° angle, while maintaining the interface between load cells and lower fixture. With this setup, load cell and DIC response was confirmed without testing an actual windscreen. Load cell and DIC data acquisition systems were tested separately with different test articles mounted to the fixture. All data acquisition parameters and setup were identical to those used in full scale testing. The setups were impacted with projectiles at test velocities and results are summarized in table 2 below.

Table 2. Summary of windscreen fixture validation tests.

| Setup Tested | Projectile | Target | Results |
|---|---|---|---|
| Load Cell | Sand Bag | Acrylic on Plywood | Vertical and horizontal load cell response confirmed |
| 3-D DIC | Sand Bag | Acrylic Citation Window | DIC pattern tracking and acquisition setup and parameters confirmed |

# CESSNA 182B COMPONENT LEVEL TESTING

## Phantom 3 Drone Fleet

Phantom 3 UAVs in new, used, and re-manufactured conditions were used for conducting all aspects of testing. Photo documentation of each side of the drone was captured along with mass before each test. Due to the Phantom 3 going out of production, several drones were reconstructed using spare and recycled components. All components and internals of reconstructed drones were to spec, with the exception of some wires being glued into place rather than soldered. For the purposes of our testing, it was not deemed necessary that our test drones be able to fly so long as all components were in their proper locations and mass distribution was correct. The only other difference between the drones used for testing is that the rotor blades were clipped to allow for a clean fit in the launcher. For consistency, the same UAV motor numbering system implemented in other Phantom 3 UAV impact tests was used and can be seen in figure 14 below [21].

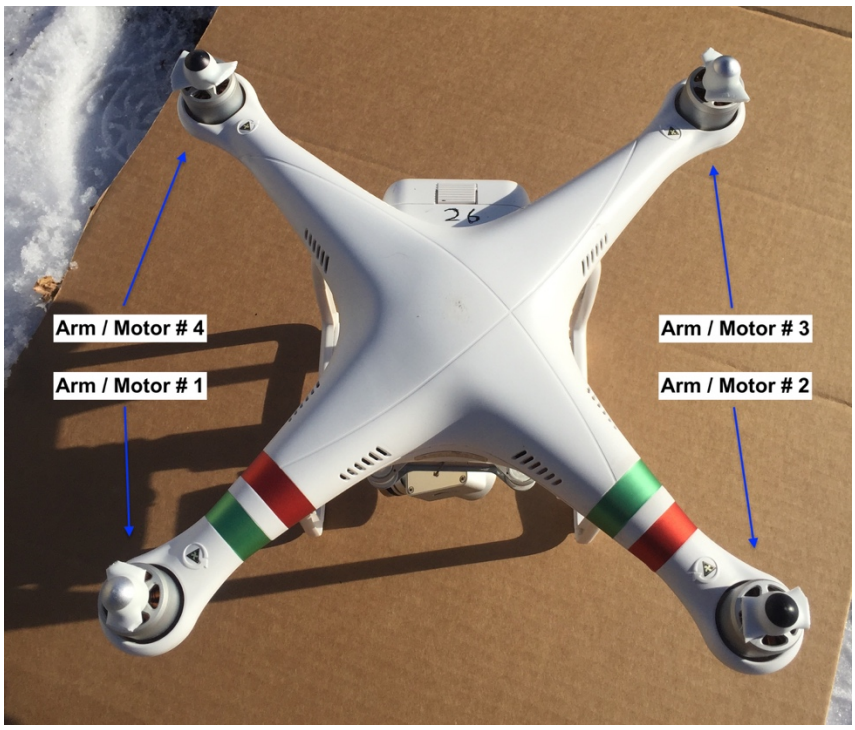



Figure 14. Phantom 3 UAV motor and arm numbering system.

## Data Acquisition Setup

### Load Cells

The setup for load data acquisition consists of the THC-10k and THD-50k load cells outlined earlier, an NI-9205 DAQ paired with a NI-cDAQ-9174 chassis, a BK Precision 1672 DC power supply to provide an excitation current. To collect and output results, LabView 2018 was used with a TDMS file converter. Due to the off grid location of the test facility, there was no A/C power readily available. This caused significant grounding issues to arise with the load cell setup since a generator was required to power all data acquisition devices. Several generators were tested to determine which introduced the smallest amount of noise to the system, and a Honda generator was ultimately decided on. To minimize noise from EMI, an earth ground was used and all

components were communally grounded. Figure 15 illustrates the wiring diagram and setup for one load cell.

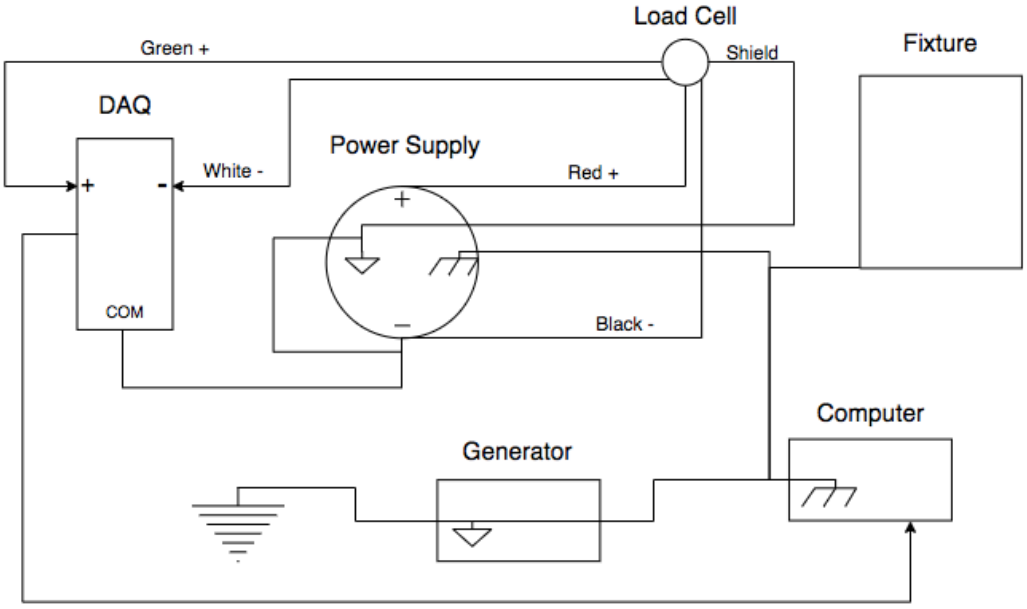



Figure 15. Wiring diagram for load cell data acquisition.

DIC

For capturing displacements with DIC, either one or two Photron NOVA S6 cameras (stereo) was used for testing wing and windscreens respectively. This type of camera uses onboard memory to store images, and if power is lost to the cameras then all data stored on the cameras is also lost. This was a major source of concern given that a generator was required to power all devices at the test site. To prevent data loss in the event of generator failure, an APC battery backup unit was used as a failsafe. The setup for 2-D DIC was very simple and required only capturing high speed footage with a known distance in a single frame that could be used for calibration. The setup for 3-D

DIC consisted of the two cameras wired in stereo with a common trigger mounted to a camera bar. To provide enough light for capturing DIC at 50k fps, two Energy Saver PHSI3060 120 watt LED lights were used to illuminate the surface. To optimize tracking of displacements, 18 mm precision tracking dots were used on the wing tip as well as the corners of the field of view for windscreen testing as recommended by the engineers at Trilion. Following recommendations from the DIC Good Practices Guide [13] a repeatable random speckling pattern was achieved with dot sizes in the optimum range for our setup (3-5 pixels across). For calibrating the GOM system, a CC20/MV1000x800 calibration cross from GOM Industries was used; details and calibration sheet for the cross can be found in Appendix I. A custom fixture was built for mounting the large cross for ease, consistency, and safety during calibration.

Measurement Uncertainty in Testing

Accurately determining the uncertainty of results is essential to being able to draw any meaningful conclusions from them. By providing bounds for data, the extent to which results can be trusted is quantified. If measurements are left unbounded, then results can not be compared to one another, reducing all of their value. Furthermore, this can lead to the spread of misinformation or misinterpretation of results. For all testing, uncertainties in load cell and DIC measurements were calculated using the methods outlined earlier. Random errors were quantified to 99% confidence, and additional sources of error in and their potential impact on measurement data are discussed for each testing setup.

## Launcher Characterization

The drone launcher used to conduct impact testing was previously developed during research conducted by another graduate student working on the project. Accuracy and repeatability requirements were deemed adequate for completing test goals [9]. Testing goals included conducting tests at both speeds of roughly 90 knots and 120 knots. In order to both accurately hit our target and control the speed of the drone at lower velocities, the launching system needed to be further characterized for draw length and band height. In place of drones, representative mass sand bags were shot at a target steel plate during the test series. Launcher draw lengths and band heights were recorded along with the corresponding velocities and shot placements. As a result of launcher characterization, it was determined that the slowest shot yielding consistent results was 80 kts with higher velocities experiencing a reduction in accuracy.

## Cessna 182B Strut Impact Testing

The goal of these tests was to collect and document impact data from a high speed (~120 knots) Phantom 3 UAV collision with a Cessna 182-B wing strut. Two tests were performed in total.

### Data Acquisition

For strut testing, data acquisition consisted of load cells at the strut attachment points and high speed video of the impact from two angles. Impact force data was collected via two Transducer Tech. THC-10k donut style load cells. Load cells were preloaded to 1000 lbf pre-test and data was sampled at 25 kHz via the system outlined

earlier. High speed video was captured with at 10,000 fps. Test site layout including camera locations can be seen in figure 16, and load cell layout can be seen in figure 17 below.

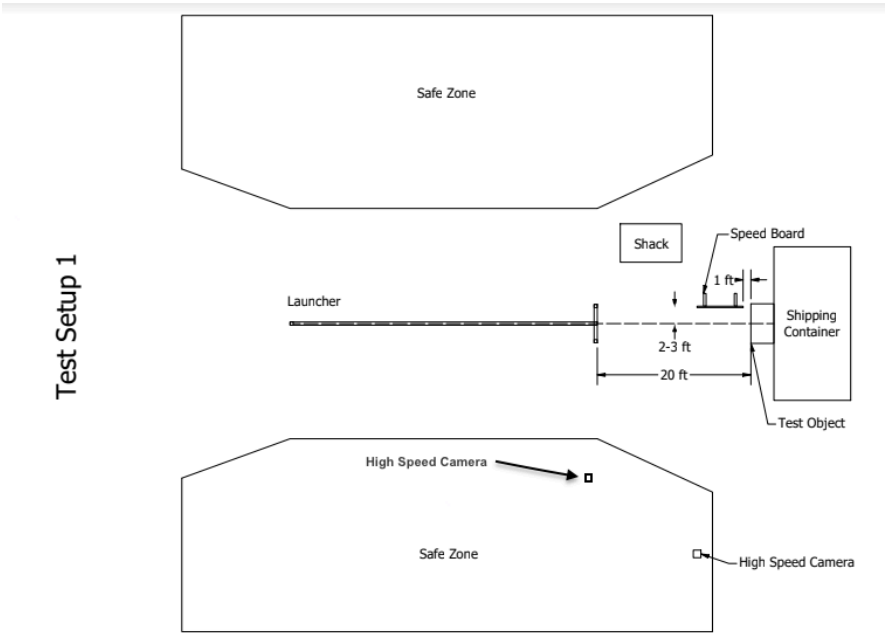



Figure 16. Test site layout for strut testing.

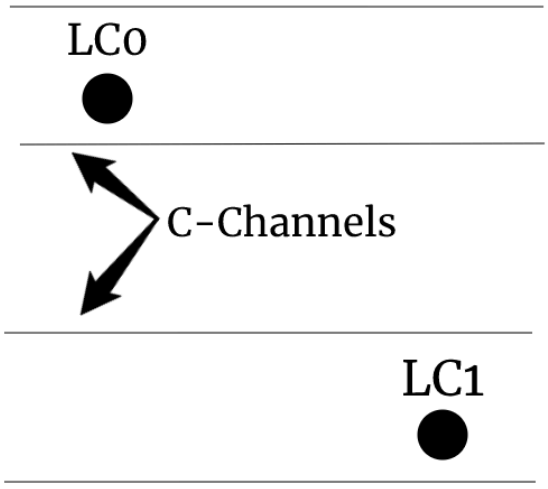



Figure 17. Load cell layout for strut testing.

Strut Testing Results

Two strut tests were performed on a right strut in total. The same strut was used for both tests due to minimal damage, and differing shot location. Results and metadata from testing is summarized in table 3 below.

Table 3. Data and results from strut testing.

| Test # | UAV # | Mass (g) | Velocity (kts) | LC 0 Peak Load (Lbf) | LC 1 Peak Load (Lbf) |
|---|---|---|---|---|---|
| A16-GA_0001 | 1 | 1103 | 129 | 2257 ± 91 | 1926 ± 113 |
| | Damage: Mostly superficial, scratches and small indentations | | | | |
| | Remarks: Camera detached on launch / LC 0 compromised | | | | |
| A16-GA_0002 | 10 | 1173.9 | 116 | 1504 ± 91 | 1590 ± 112 |
| | Damage: Mostly superficial, small gouge and indentations | | | | |
| | Remarks: Motor #4 and motor #1 impacted target | | | | |

Testing showed mostly superficial damage from a drone impact with a strut. Both test shots glanced off the side of the strut, impacting with 1 or 2 motors. Test A16-GA_0002 showed the greatest damage out of the two, and consisted of small indentations, gouges, and scratches to the paint. The crash sequence for test A16-GA_0002 can be seen in figure 18 below.

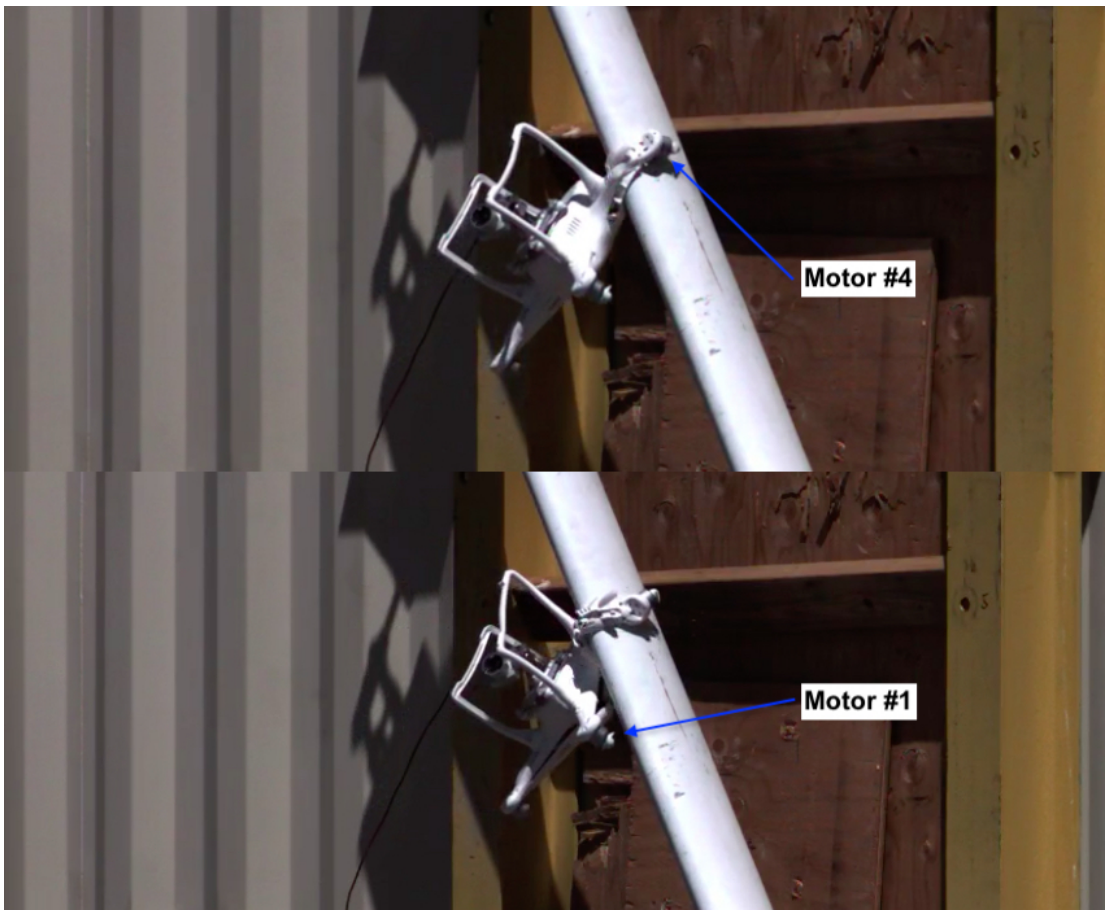



Figure 18. Impact orientation and crash sequence of UAV #10 in test A-16-GA_0002.

As can be seen in figure 18, the drone tumbled forward after its release from the bucket. Arm #4 impacted the strut first, soon followed by motor #1 lower down on the strut. Damage from this test was more substantial than the first, yet was still largely superficial. Motor #4 inflicted paint chipping and a small gouge 11/16" long and 1/64" deep out of the aluminum. Motor #1's imparted more damage due to impacting closer to the leading edge of the strut. Damage consisted of paint chipping along with a dent to the structure. The dent measured 1/16" deep and 1 ¼" along the length of the strut. The surrounding strut remained fully intact. Damage from test A16-GA_0002 can be seen in figure 19 below.

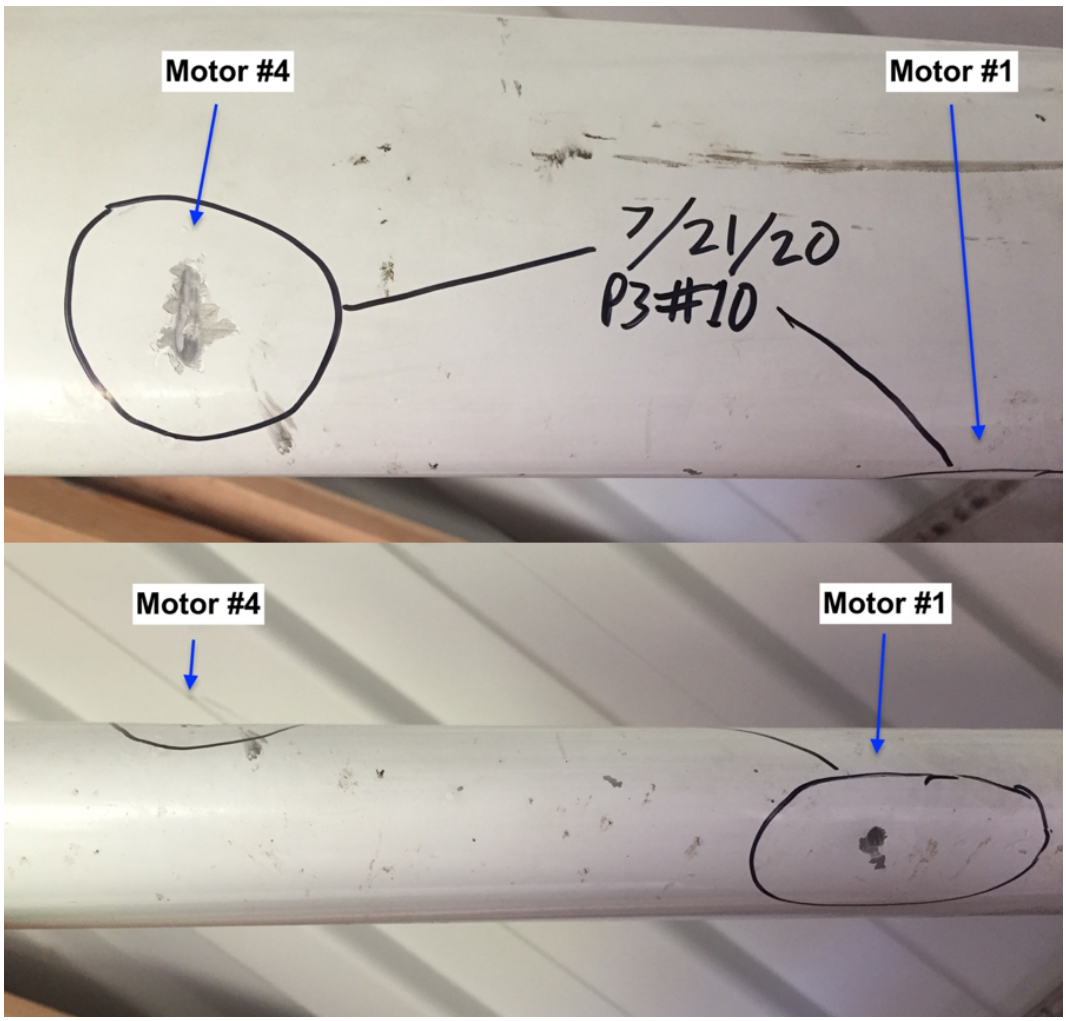



Figure 19. Damage from test A16-GA_0002.

Load cell data showed that reaction forces were equally distributed between the two attachment points. As expected, following impact there is a sharp peak in load results followed by decaying oscillations until reaching stasis. Force data plots for test A16-GA_0002 can be seen below in figure 20.

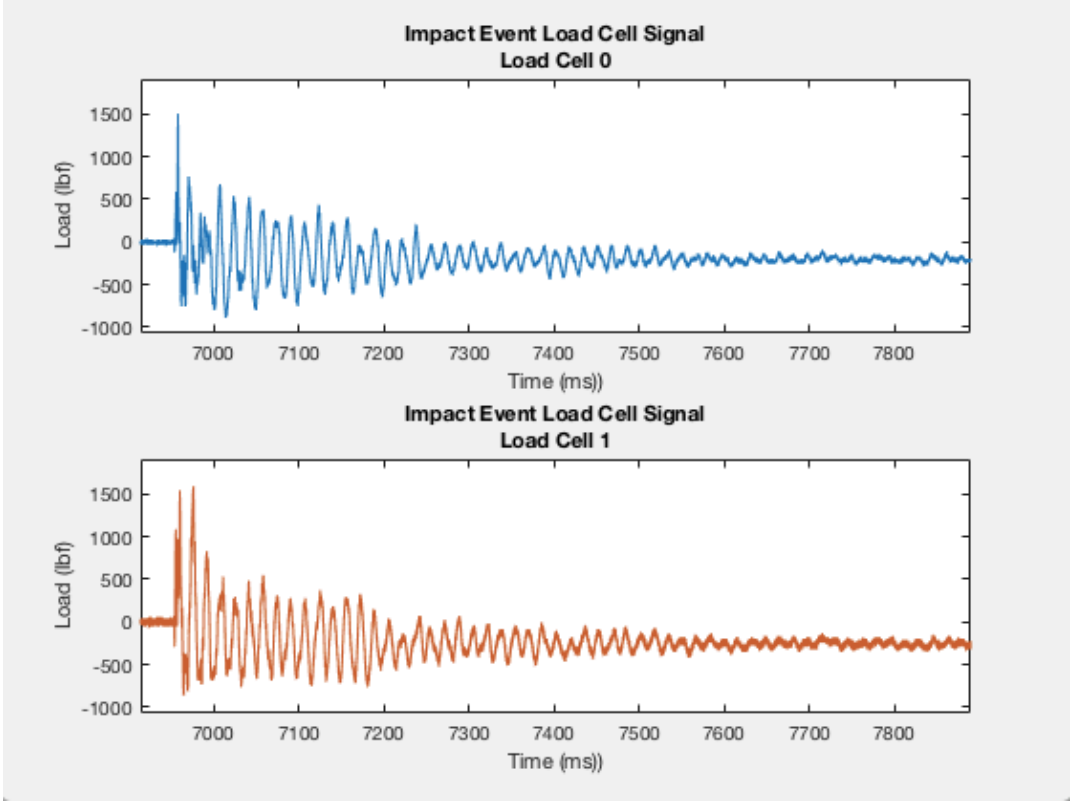



Figure 20. Load cell output from Matlab for test A16-GA_0002.

During test A16-GA_0001 the connection to LC 0 was damaged, and signal was briefly sent to ground. Due to this, load cell data from this test cannot be trusted. Otherwise, all data acquisition systems performed as planned. Crash sequences, damage, and force plots from test A16-GA_0001 can be found in Appendix C.

Strut Testing Error

There were several factors that contributed to error during the testing sequence. General sources for measurement error with load cells were detailed earlier and uncertainty is presented for each load cell in each test. Additional sources of error specific to strut testing are outlined in table 4 below.

Table 4. Sources of error in load data for strut testing and effects on results.

| Source of Error | Effect on Results |
|---|---|
| Mass change of UAV #1 | Change in kinetic energy of drone |
| Load cell wire damage | Load data sent to ground during test A16-GA_0001 |
| Off axis loading | Skew of load data |
| Fixture geometry | Bending moment leading to off axis loading |
| Loss of pre-load | Reduction in peak loading |

- Mass of UAV 1. Due to the camera detaching from UAV 1 during release from the launcher, its mass was reduced. To find the mass of the drone when it impacted, the mass of another camera (83g) was subtracted from the original mass of UAV 1. Although the cameras likely had a similar weight, it should be noted that there is probably some discrepancy although small.
- Load Cell Wire Damage. In test A16-GA_0001, a sharp edge on the load cell housing lightly cut the outside of the load cells wire during the impact. The steel housing contacted the grounding braid within the load cell wire, sending the signal briefly to ground for both load cells since a common ground was used. Peak load cell data collected before the signal was grounded may still be accurate, but results should not be trusted due to the compromised wire.
- Off Axis Loading. The load cells used for testing are uni-axial, and can only collect data on forces perpendicular to their orientation. While most of the force transmitted from the UAV is in this direction, there is likely still some off axis loading due to flexing of the strut. As the strut flexes, it pulls the bolts toward the strut center, possibly influencing load results. Error from off axis loading is believed to be small due to the load cell design, but worth noting.

- Fixture Geometry. In order to incorporate the 4° angle of the strut attachments, the load cell housings were machined to reflect that angle. This means that the bolt attaching the strut to the fixture is not aligned with the axis that the load cells detect force on and a bending moment may occur. This could be a source of error present in load data, but is believed to be small.
- Reduction in Pre-Loading. In both tests, the impact was strong enough to jostle the bolt connections at the load cells slightly loose, reducing the pre-load that was performed prior to testing. Due to this, load values past the initial peak response are likely lower than reality. Load cell zero dropped about 250 lbf during both tests as the strut oscillated post collision.

Strut Testing Conclusions

Testing showed that damage to a Cessna 182B strut from a collision with a Phantom 3 quadcopter may have dangerous results. For impacts at velocities of 129 kts and 116 kts, significant force was reacted through the attachment points, with test A16-GA_0001 delivering a combined total of 4183 lbf to the structure, and test A16-GA_0002 delivering a total of 3094 lbf. The structural integrity of the strut remained mostly in tact post collision, but the small plastic deformations sustained are cause for concern. This is due to the potential for local buckling to occur at the locations of the dents. During flight, the strut would experience compression and tension as the plane ascends and descends respectively. When the strut is under compression, dents in the structure could become problematic due to the nature of thin walled cylinders. If buckling were to induce failure of the strut, a dangerous situation would arise. Even small dents can

seriously compromise the structural integrity of a thin walled cylindrical shape [29] and as a result, this potential failure mode must be noted. Additional testing where a compressive load is applied to the strut would be needed to determine whether the dents seen in the strut would result in buckling. Although damage to the strut itself was mostly superficial, the forces reacted through the struts attachment points could be problematic. The strut attachment points on a C-182B are aluminum pin connections and it's possible that their structural integrity would be compromised from forces reacted through the strut. Since this test was designed to investigate damage to only the strut from such an impact, additional testing is required to determine if forces are substantial enough to cause failure at attachment points. Due to the limited number of strut tests conducted, additional testing would be necessary to draw any hard conclusions, but testing showed that there is potential for strut failure from a drone collision.

## Cessna 182B Wing Impact Testing

The goal of these tests was to collect and document impact data from a low speed (~90 knots) Phantom 3 UAV collision with a Cessna 182-B right wing. Two tests were performed in total.

### Data Acquisition

For wing testing, data acquisition consisted of: collecting reaction force data with load cells at both the wing attachment points and the mimic strut attachment point, high speed video of the collision from two angles, and 2-D DIC displacement data at the wing tip. Two Transducer Tech. THC-50k donut style load cells were used at the wing

attachments, and one THC-10k load cell at the mimic strut attachment. Wing load cells were preloaded to 1000 lbf pre-test and the strut load cell was preloaded to 5000 lbf pre-test to capture both compression and tension loading. Data was sampled at 25 kHz via the system outlined earlier. High speed video for both DIC and impact capture was taken at 10,000 fps. The test site layout and load cell numbering system is shown below in figures 21 and 22 respectively.

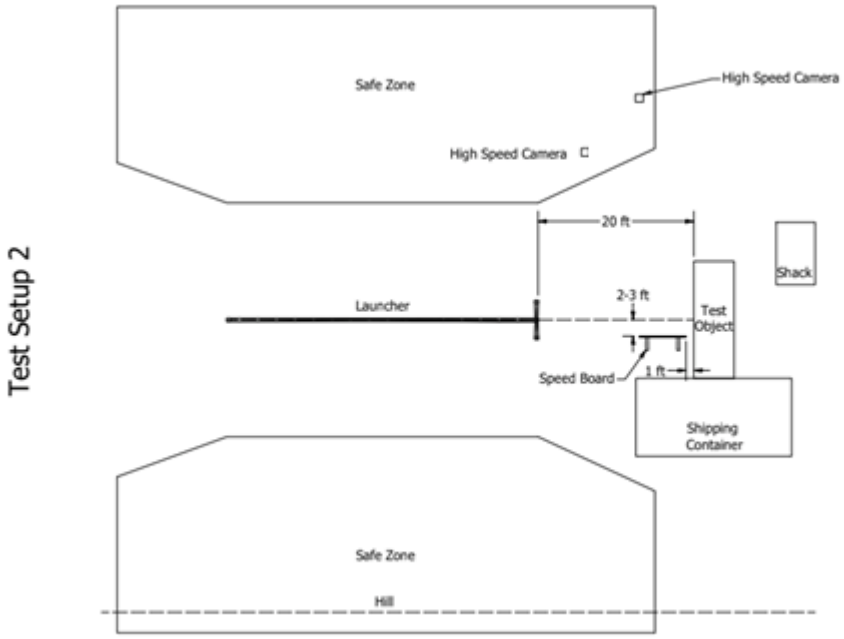



Figure 21. Test site layout for wing (right) testing.

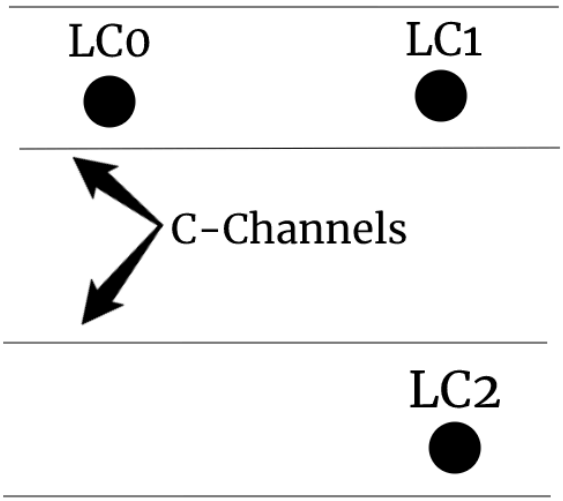



Figure 22. Load cell layout for wing (right) testing.

Wing Nomenclature

Definitions and locations on the wing were referenced using the following system. Wing measurements were taken along the spar closest to the leading edge of the wing. Ribs are numbered starting at the wing tip from 1-7. For DIC on the wing tip, 7 tracking dots were placed on the wing tip face. Axes are defined such that + y is up and + x is to the right. To evaluate severity of wing damage, the system defined by ASSURE in their wing testing series will be used here and is shown in table 5. Figures 23 and 24 illustrate the wing nomenclature and tracking dot locations.

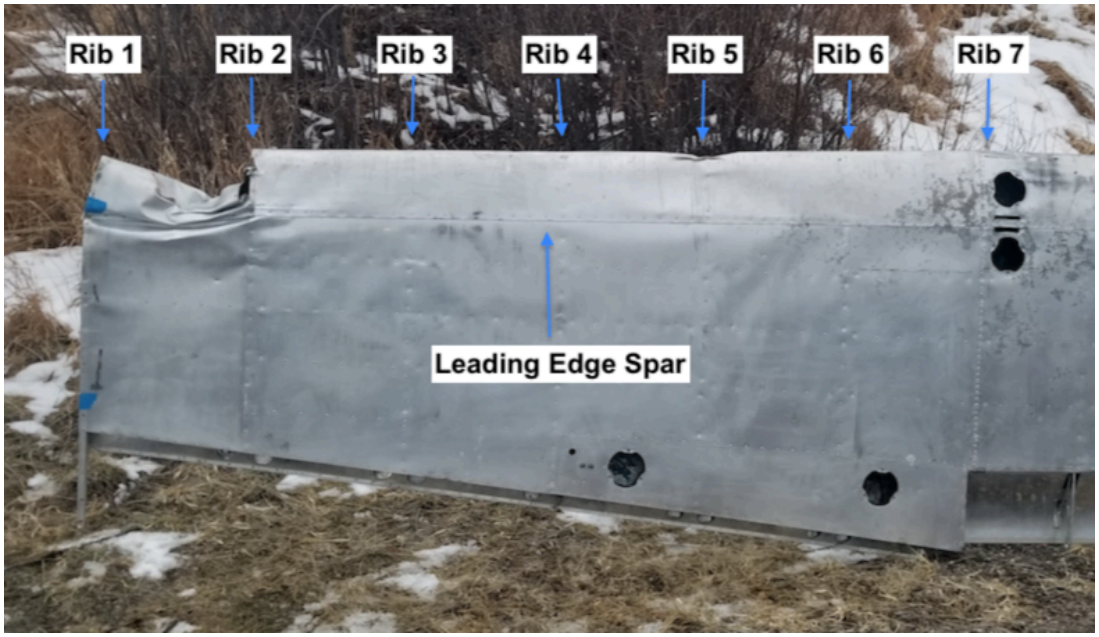
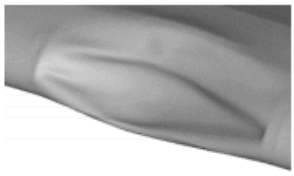
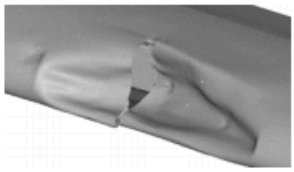
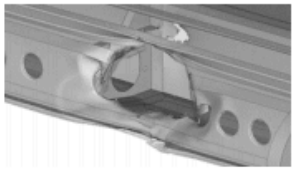



Figure 23. Locations and numbering system of ribs and leading edge spar.




Figure 24. Layout of tracking dots on wing tip from GOM Correlate.

Table 5. Damage level categories (FAA – ASSURE) [7].

| Severity | Description | Example |
|---|---|---|
| **Level 1** | • Airframe undamaged.<br>• Small deformations. |  |
| **Level 2** | • Extensive permanent deformation on external surfaces.<br>• Some deformation in internal structure.<br>• No failure of skin. |  |
| **Level 3** | • Skin fracture.<br>• Penetration of at least one component into the airframe. |  |
| **Level 4** | • Penetration of UAS into airframe.<br>• Failure of parts of the primary structure. |  |

Wing Testing Results

Both wing tests successfully impacted the wing. The same wing was used for both tests, with the target zone shifted inward for the second shot. Test A16-GA_0003 resulted in a direct hit between the UAV center mass and the wing tip. Test A16-GA_0004 resulted in a direct hit between the camera assembly and rib #5, with the drone body glancing off the wing low. Results can be seen below in tables 6 and 7.

Table 6. Test data and results for wing test A16-GA_0003.

| | UAV # | Mass (g) | Velocity (kts) | Target |
|---|---|---|---|---|
| A16-GA_0003 | 5 | 1175.3 | 93 | Wing tip |
| | Damage: Level 3 damage sustained, crumpling up to leading edge spar 7” deep and 11” across | | | |

| | | | | | | | |
|---|---|---|---|---|---|---|---|
| | Remarks: Direct hit on wing tip 173 ½" from base | | | | | | |
| | LC 0 Peak Load (Lbf) | | | LC 1 Peak Load (Lbf) | | LC 2 Peak Load (Lbf) | |
| | 6965 ± 465 | | | 6304 ± 538 | | -1750 ± 104 | |
| | DIC Dot # | Max + dx (mm) | Max – dx (mm) | Uncertainty (+/-) (mm) | Max + dy (mm) | Max – dy (mm) | Uncertainty (+/-) (mm) |
| | 1 | 19.47 | -61.68 | 0.45 | 31.69 | -47.90 | 0.45 |
| | 2 | 30.29 | -49.89 | 0.45 | 45.01 | -39.36 | 0.45 |
| | 3 | 30.35 | -49.94 | 0.45 | 45.42 | -38.93 | 0.45 |
| | 4 | 30.59 | -49.70 | 0.45 | 45.94 | -41.10 | 0.45 |
| | 5 | 30.56 | -49.70 | 0.45 | 46.14 | -41.09 | 0.45 |
| | 6 | 30.41 | -49.73 | 0.45 | 46.54 | -43.25 | 0.45 |
| | 7 | 30.58 | -49.76 | 0.45 | 46.74 | -43.31 | 0.45 |

Table 7. Test data and results for wing test A16-GA_0004.

| | | | | | | | |
|---|---|---|---|---|---|---|---|
| A16-GA_0004 | UAV # | Mass (g) | | Velocity (kts) | | Target | |
| | 6 | 1181.8 | | 98 | | Wing Center | |
| | Damage: Level 3 damage sustained, crumpling at rib #5 measuring 2" deep and 9 ½" across | | | | | | |
| | Remarks: Camera assembly was primary impact at rib #5, 112" from base | | | | | | |
| | LC 0 Peak Load (Lbf) | | | LC 1 Peak Load (Lbf) | | LC 2 Peak Load (Lbf) | |
| | 1542 ± 463 | | | 1505 ± 539 | | -679 ± 105 | |
| | DIC Dot # | Max + dx (mm) | Max – dx (mm) | Uncertainty (+/-) (mm) | Max + dy (mm) | Max – dy (mm) | Uncertainty (+/-) (mm) |
| | 1 | 8.20 | -10.82 | 0.44 | 10.61 | -9.91 | 0.44 |

| | | | | | | | |
|---|---|---|---|---|---|---|---|
| | 2 | 8.12 | -10.56 | 0.44 | 11.22 | -10.57 | 0.44 |
| | 3 | 8.12 | -11.02 | 0.44 | 11.30 | -10.56 | 0.44 |
| | 4 | 8.17 | -10.82 | 0.44 | 11.55 | -10.92 | 0.44 |
| | 5 | 8.34 | -10.82 | 0.44 | 11.62 | -10.87 | 0.44 |
| | 6 | 8.12 | -10.76 | 0.44 | 12.02 | -11.26 | 0.44 |
| | 7 | 8.04 | -11.03 | 0.44 | 11.98 | -11.28 | 0.44 |

Test A16-GA_0003 resulted in significantly more damage than A16-GA_0004, though both caused level 3 damage to the wing structure. This was due to the drone's center mass hitting the wing dead on, compared to the camera assembly primarily impacting the wing in the second test. Figure 25 shows the UAV's impact orientation and crash sequence for test A16-GA_0003 below.

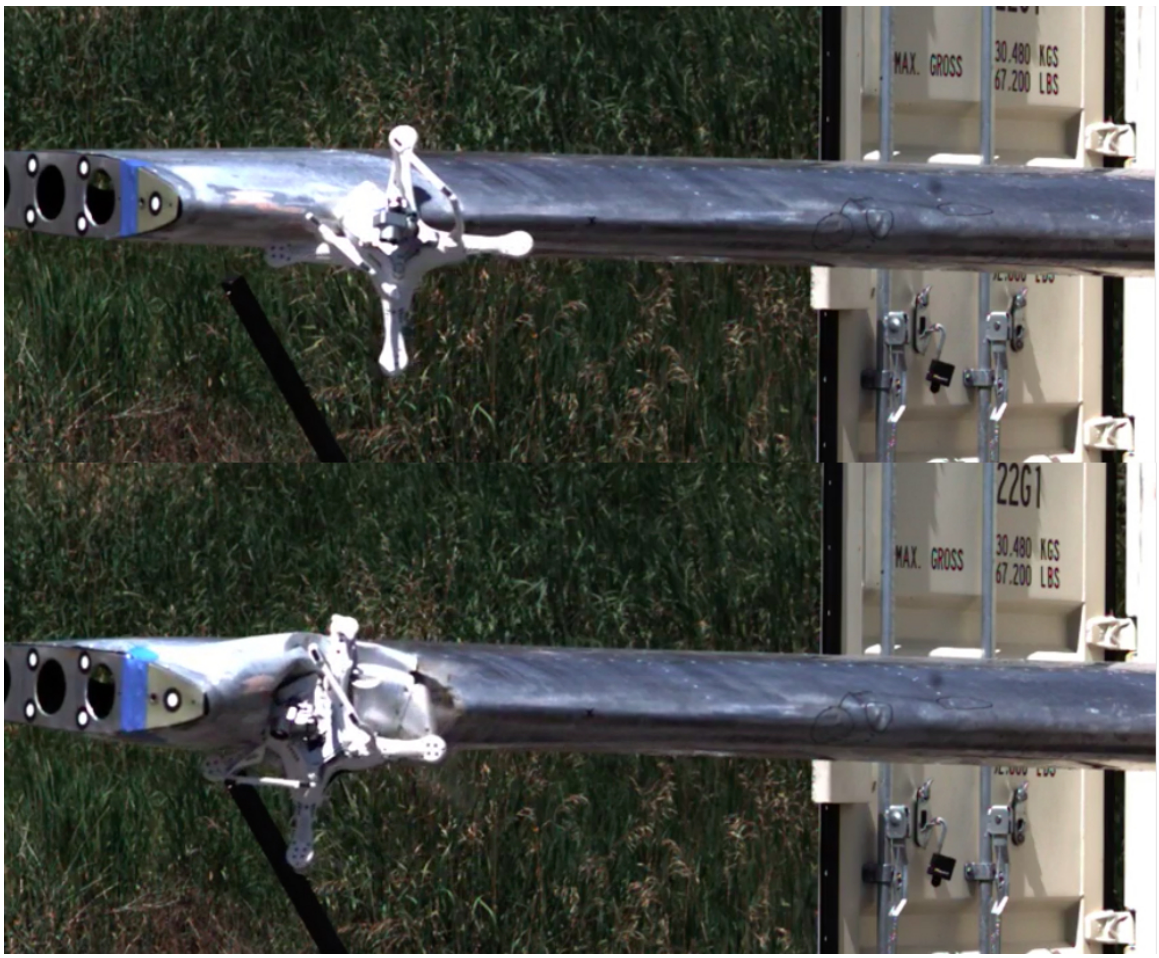



Figure 25. Impact orientation and crash sequence of UAV 5 in test A16-GA_0003.

As seen in the above figure, the drone tumbled forward and rotated to the right during flight, with the rear (battery) side of the drone impacting the wing first. The primary impact was from the center mass of the drone, colliding just below center between ribs #1 and #2. Upon impact, the wing skin crumpled back to the leading edge spar and was torn off the rivets at rib #2 as can be seen in the figures below. Post collision the UAV dropped straight down to the ground, indicating that most of its kinetic energy had been passed on to the wing. Damage from test A16-GA_0003 is shown in figure 26 below.

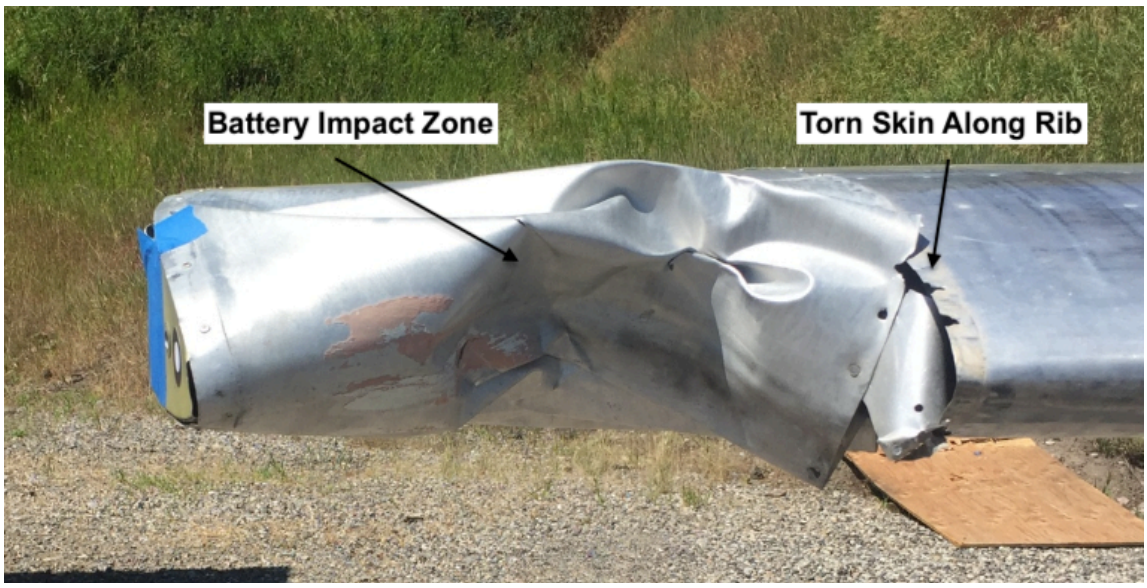


Figure 26. Damage from test A16-GA_0003.

Load cell data acquisition systems performed as planned, successfully capturing reaction forces at each attachment point. Peak loads were lower than expected given the mechanical advantage of the wing span and were well within load cell capacity limits. Significantly more force was reacted through the attachments in test A16-GA_0003 than in A16-GA_0004 due to both the location and directness of the impact. In both tests, peak loads in load cells #0 and #1 were similar in magnitude, peaking shortly after impact and then damping out until stasis was reached. Load cell #2 showed an initial tensile load followed by compression as the wing rebounded back and forth post impact. Reaction forces at the attachments are shown graphically for test A16-GA_0003 in figure 27 below.

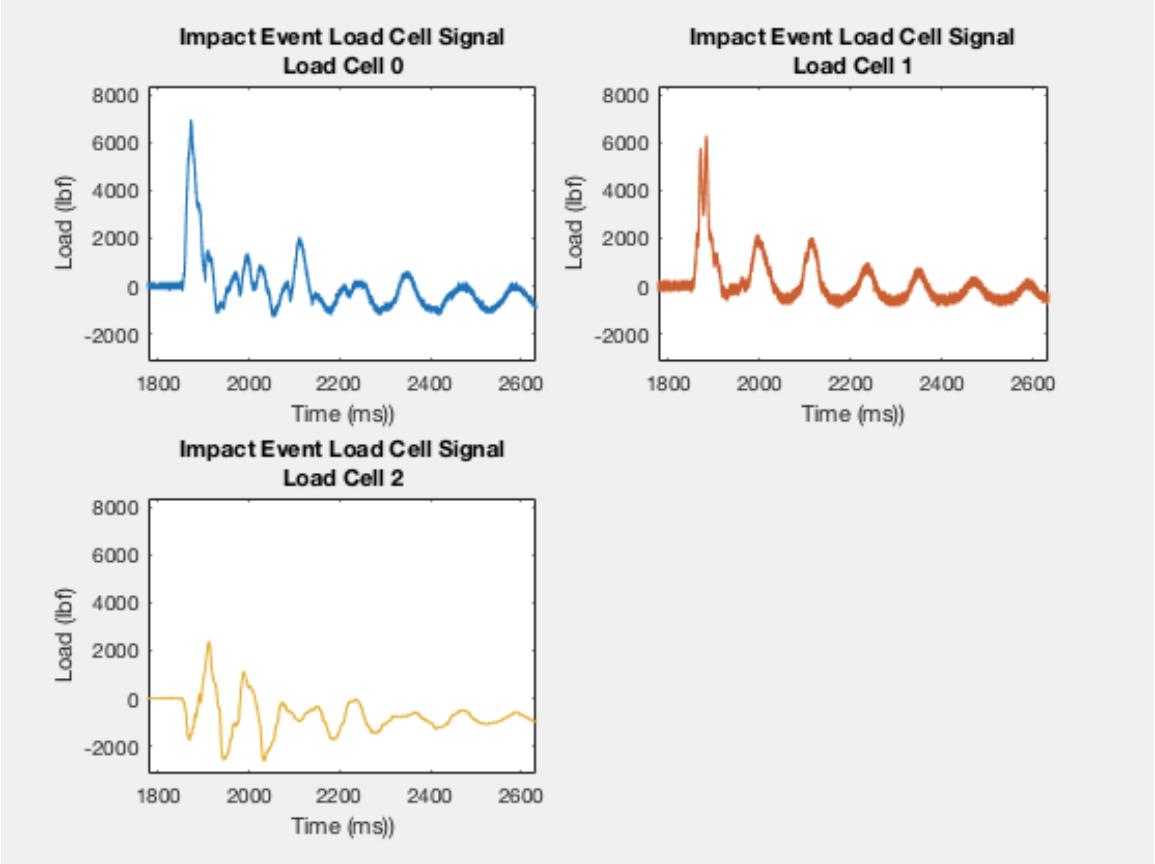



Figure 27. Load cell output from Matlab for test A16-GA_0003.

2-D DIC successfully captured the motion of the wing tip during impact at the tracking dot locations detailed earlier. In test A16-GA_0003, tracking dot 1 was shifted due to wing deformation during the collision and as a result cannot be used to analyze displacements. Visibly none of the other tracking dots seemed to be affected by the deformation near the leading edge, and data was determined to be trustworthy. This was further confirmed when analysis in GOM that showed dots 2-7 tracked consistently as a group. Wing tip displacement plots for test A16-GA_0003 are shown below in figures 28 and 29. For additional details on wing test A16-GA_0004 refer to Appendix D.

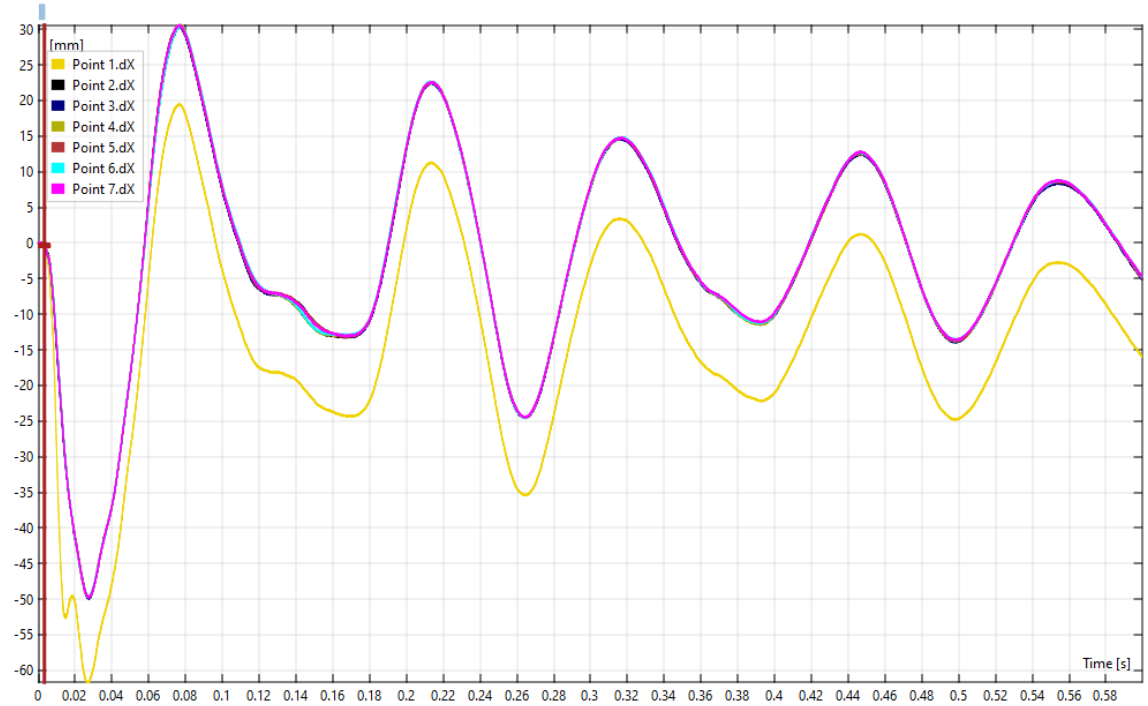



Figure 28. 2-D displacement tracking in x-direction for test A16-GA_0003.

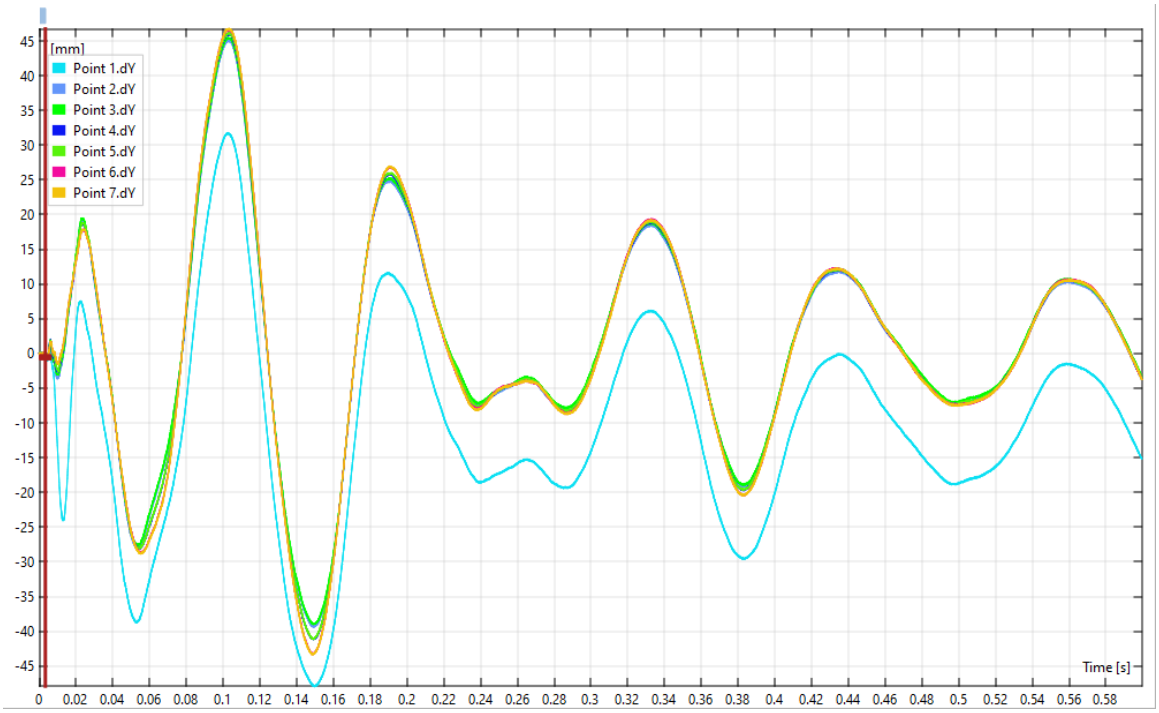



Figure 29. 2-D displacement tracking in y-direction for test A16-GA_0003.

Wing Testing Error

There are several potential sources of error that need to be addressed and quantified for wing testing. Error is separated into load cells and DIC below.

Load Cells. Force data collection is likely the biggest source of error in wing testing. General sources of error in the load cell system were outlined and presented earlier, therefore only sources of error specific to wing testing are outlined in table 8 and discussed below.

Table 8. Sources of error in load data for wing testing and effects on results.

| Source of Error | Effect on Results |
|---|---|
| Fixture Geometry | Binding at load cells |
| Loss of Pre-load | Reduction in peak loads |
| Wind Loading | Additional source of reaction forces |

- Fixture geometry. Although the fixtures were designed and machined to precise tolerances, there is a possibility that slight binding may have occurred at the bolted load cell c-channel interfaces during installation. If the bolts were off axis slightly, they could impede a flush connection between the fixture and the load bearing face of the cell and affect the strain gages response. To avoid this, load cells were pre-loaded and response tests were performed to ensure that the load cells responded accurately.
- Reduction in pre-load. Another contributing factor is the reduction of pre-load during the test sequence. During both tests, the impact was strong enough to jostle the bolt connections at the load cells slightly loose, reducing the pre-load

that was performed prior to testing. Due to this, load values past the initial peak response likely experienced a reduction in load.

- Wind Loading. One unfortunate consequence of outdoor testing, is that tests are subjected to wind. Due to the size of a wing, wind could have a greater impact on load cell outputs than other tests. The added leverage from the length of the wing only makes it more likely that small changes or gusts in wind could show up in load cell data. However, since tests were conducted with small amounts of wind present, load cell error from wind loading is likely negligent in comparison to other sources of error.

2-D DIC. Uncertainty in DIC measurements was quantified using the methods outlined earlier. Sources of error specific to wing testing are outlined in table 9 and discussed below.

Table 9. Sources of error in 2-D DIC for wing testing and effects on results.

| Source of Error | Effect on Results |
|---|---|
| Calibration | Increased measurement uncertainty |
| Tracking Dots | Loss of tracking |
| Out of Plane Motion | Increased uncertainty |
| Camera Setup | Loss of tracking |

- Calibration. Calibration for 2-D DIC was performed by inputting a known length of an object occupying the same plane as the QOI. Due to this, accuracy of DIC is largely dependent on the accuracy of the input length. For our testing, the distance between two pieces of masking tape on the wing tip was measured to the nearest 1/32”. This means that there is about 1/64” of error associated with this measurement, thus introducing an additional 1/64” (0.40 mm) of uncertainty to 2-

D DIC results. To reduce the error associated with calibration, a distance known to a higher degree of accuracy is required. This is one of the reasons why using a 3-D DIC system with a precision calibration artifact is advantageous.

- Tracking Dots. Tracking dots are another possible source for error since they are what GOM recognizes and keeps tabs on. During 2-D tests, only tracking dots specially designed by Trillion for DIC were used. Due to this, error in measurements caused by the tracking dots is believed to be very small compared to other sources.
- Out of Plane Motion. Out of plane motion will introduce error into any 2-D DIC measurements [13]. As the wing tip deflects, it will swing out an arc causing some small motion in the z-direction to occur. This will induce error in displacement data since the cameras system is recognizing motion in only two dimensions and motion in the z-direction has the largest influence on noise. To quantify error due to out of plane motion, the distance between tracking dots 4 and 6 was measured in GOM pre-impact and again at max displacement during the test sequence. For test A16-GA_0003 this measured out to be 166.04 mm and 166.22 mm respectively. The difference of 0.18 mm between the measurements is within the uncertainty calculated earlier, and not significant enough to greatly influence results. That being said, a small amount of error due to out of plane motion does exist.
- Camera Setup. Setup of the high speed camera could be a potential source for error if not done correctly. Factors such as frame rate, focus, and lighting could

influence results. High speed cameras were setup with professional help from Rock Mountain High Speed, so error due to camera setup is small in comparison to other sources.

Wing Testing Conclusions

Testing of a C-182B right wing showed that a collision with a UAV has the potential to be catastrophic. Both tests showed that level 3 structural damage will be sustained from a direct impact even at slower takeoff velocities. Cruising speed for a C-182B is around 140 kts [23], over 1.5 times the shot speeds in these tests. Though it is most likely for a collision to occur during take off or landing, if a collision occurred at cruising speed the result would likely be deadly. One can postulate that if a collision occurred at 1.5 times the speed, corresponding damage and force reacted through the wing would scale accordingly.

Peak loading at the attachment points proved to be lower than anticipated with a peak load of 6965 lbf. This can likely be attributed to how much the wing crumpled during impact. Higher capacity load cells were used to combat the added leverage of the wing, resulting in the lower resolution seen in load cell data. In turn, this lower resolution accounts for the increase of error in measurements. For future tests at similar velocities, 10k load cells would provide optimal resolution in measurements and increase the accuracy of results. However, at higher velocities capacity would need to be increased.

DIC data showed that the wing tip deflects upon impact, with a backward deflection of 49.7 mm in test A16-GA_0003. The amount of tip deflection and force

reacted through the attachments is likely to be highly dependent on two aspects of impact location, length from the wing base and proximity to ribs. The farther out on the wing the collision, the more leverage there is to amplify forces at the attachment points. Proximity of the impact to wing ribs is an important factor in that there is more structural resistance at the ribs than in between them. Basic impulse mechanics show that force is inversely proportional to time, meaning that the shorter the collision time the greater the impulse. It can be expected that impact duration would be shorter at rib collisions due to increased structural support there. Load cell data showed that the trailing edge attachment experienced compression while the other attachments experienced tension during the impact event. No signs of shearing were seen on the wing attachments, but shear loads on the pin could potentially cause failure at higher impact velocities. Further testing is needed to determine a threshold for failure at the attachment points.

Based on the results from these tests, there is a chance of catastrophic failure if a UAV were to impact a wing mid-flight. Test A16-GA_0003 likely showed maximum damage from a wing impact at low velocity due to the shots placement and the directness of the hit. While it is possible that a plane could land after such a collision, it is also possible that the planes aerodynamics could be altered enough to cause a crash. Testing showed that there is the potential for catastrophic failure from a wing hit. However, evaluation of additional crash scenarios would be required to confirm or deny.

## Cessna 182B Windscreen Impact Testing

The goal of windscreen testing was to collect and document impact data from both low speed (~90 knots) and high speed (~120 knots) UAV collisions with a Cessna 182-B windscreen. Eight tests were performed in total.

### Data Acquisition

For windscreen testing, data acquisition consisted of collecting load cell impact data at both the horizontal and vertical attachment points, high speed video of the collision from two angles, and 3-D DIC displacement data for the windscreen from a cockpit view. Impact force data was collected via eight of the Transducer Tech. THC-10k donut style load cells at the attachments. Horizontal load cells were preloaded to 1000 lbf pre-test and the vertical load cells were preloaded to 100 lbf. Data was sampled at 25 kHz and high speed video was captured at 10,000 fps. The 3-D DIC system was calibrated through the acrylic protective window for optical consistency, and data was collected at 50,000 fps. A combined approach of tracking dots and speckling pattern was used to collect deflections at points and as a surface respectively. Tracking dots were located in a 3-D model of the windscreen for each test by taking measurements from fixed locations on the windscreen. The test site layout, load cell numbering, and interior view of the windscreen is shown below in figures 30 – 32 respectively.

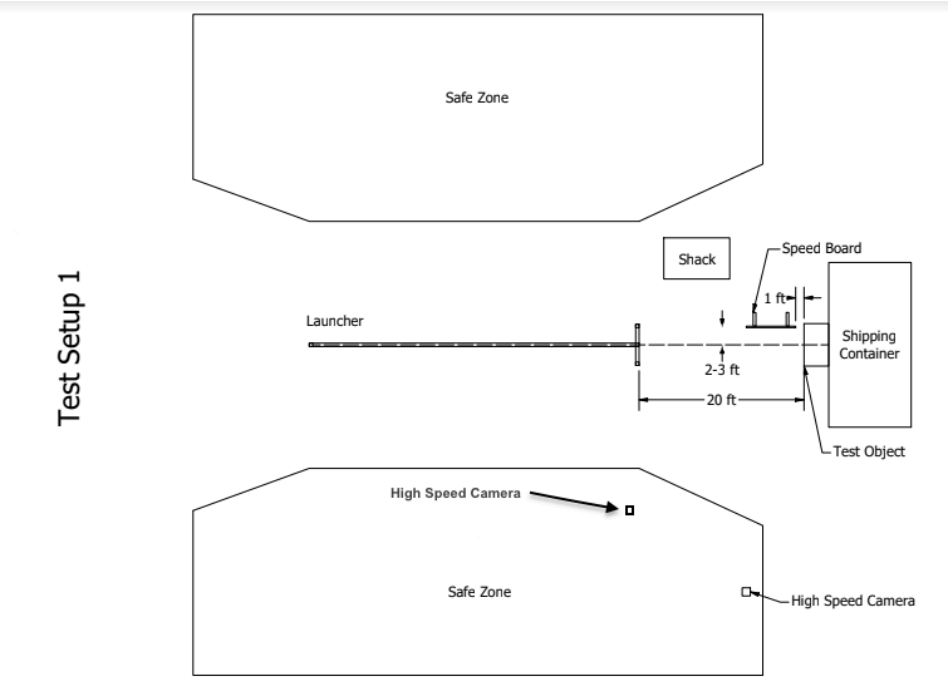



Figure 30. Test site layout for windscreen testing.

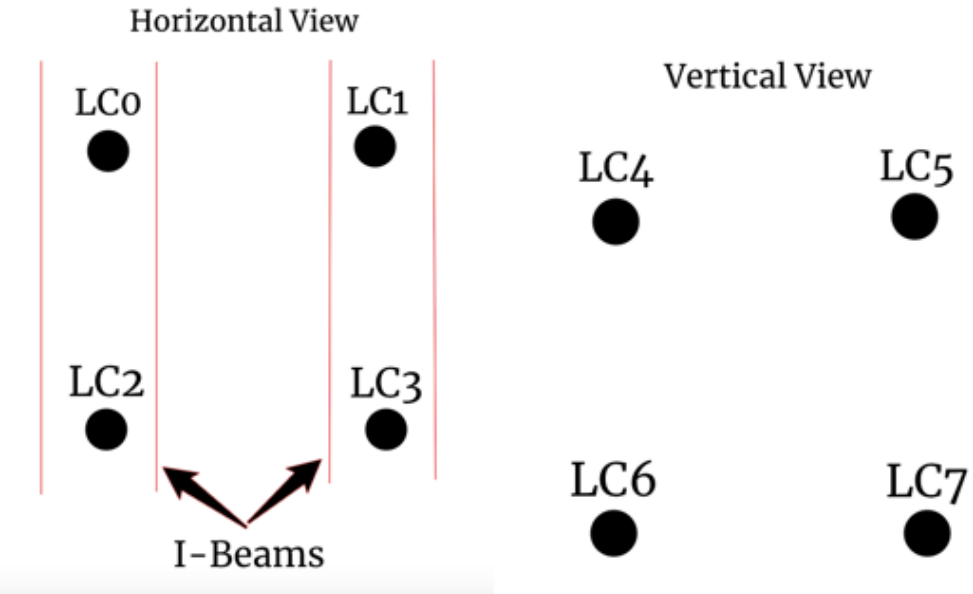



Figure 31. Load cell numbering for windscreen testing.



Figure 32. Interior view of windscreen with speckle pattern and tracking dots.

3-D DIC Windscreen Nomenclature

Tracking dots were placed around the edges of the cropped field of view of the DIC cameras. The numbering system for the dots goes from left to right in rows, starting at 1 and is shown in figure 33 below.

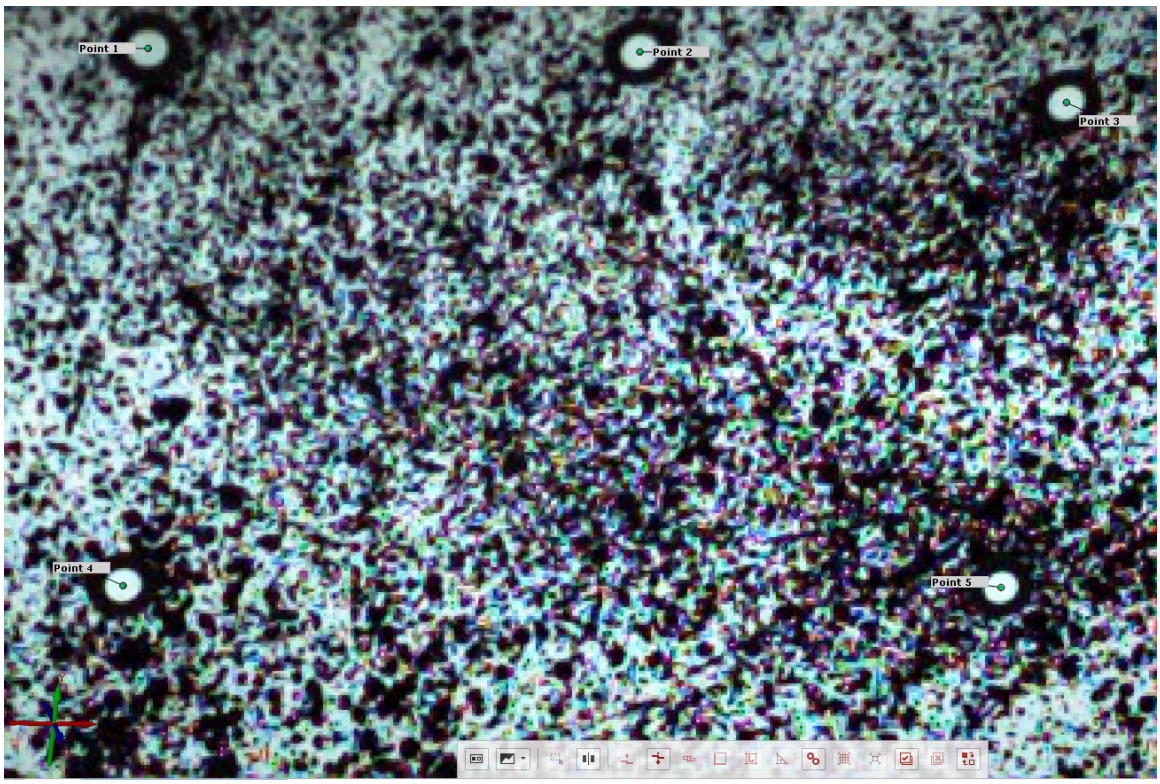


Figure 33. Point component numbering for windscreen testing from GOM.

Two coordinate systems were available for use in GOM, with the original coordinate system being derived from the camera calibration. The alternate coordinate system was created with a 3-2-1 alignment and is based on the geometry of the windscreen itself. It is relative to the placement of the point components and has the following definition.

- The z-axis is orthogonal to the plane defined by points 2, 4, and 5.
- The y-axis is orthogonal to the z-axis and the line defined by points 4 and 5.
- The x-axis is orthogonal to the y and z-axes and passes through point 4.

The alternate coordinate system will be used in analyzing results in GOM. All directions regarding DIC layout are referenced from a cockpit view.

Windscreen Test Results

Eight windscreen tests were conducted in total four windscreens. For tests that did not result in failure of the windscreen, the same windscreen was reused. Due to a combination of the launcher's inaccuracy at high speeds and the narrow target window of the windscreen, unimpeded collisions to the windscreen were only achieved for low velocity test shots. All high velocity shots clipped the protective steel plate as the drone tumbled towards the target, resulting in a compromised test. Results and data from unimpeded windscreen tests is shown in tables 10-13 below.

Table 10. Results and data from test A16-GA_0008.

| | | | | | | | | |
|---|---|---|---|---|---|---|---|---|
| A16-GA_0008 | UAV # | | Mass (g) | | Velocity (kts) | | Target | |
| | 16 | | 1188 | | 88 | | Center | |
| | Damage: Skid mark on center windscreen, elastic deformation only. | | | | | | | |
| | Remarks: Clean shot, high center windscreen | | | | | | | |
| | LC 0 (lbf) | LC 1 (lbf) | LC 2 (lbf) | LC 3 (lbf) | LC 4 (lbf) | LC 5 (lbf) | LC 6 (lbf) | LC 7 (lbf) |
| | 651 ± 91 | 623 ± 106 | 641 ± 93 | 795 ± 93 | 455 ± 87 | 402 ± 88 | 361 ± 92 | 434 ± 80 |
| | DIC Peak Location | | Deformation in x (mm) | | Deformation in y (mm) | | Deformation in z (mm) | |
| | Point 41 | | +0.164 ± 0.011 | | -4.341 ± 0.021 | | +23.951 ± 0.045 | |

Table 11. Results and data from test A16-GA_0009.

| | | | | |
|---|---|---|---|---|
| A16-GA_0009 | UAV # | Mass (g) | Velocity (kts) | Target |
| | 12 | 1157.3 | 87 | Center |
| | Damage: No observable damage | | | |
| | Remarks: Impact high, only one motor made contact / More points setting used for DIC | | | |

| | LC 0 (lbf) | LC 1 (lbf) | LC 2 (lbf) | LC 3 (lbf) | LC 4 (lbf) | LC 5 (lbf) | LC 6 (lbf) | LC 7 (lbf) |
|---|---|---|---|---|---|---|---|---|
| | 1023 ± 91 | 583 ± 107 | 828 ± 93 | 402 ± 93 | 493 ± 87 | 670 ± 88 | 136 ± 92 | 279 ± 80 |
| | DIC Peak Location | | Deformation in x (mm) | | Deformation in y (mm) | | Deformation in z (mm) | |
| | Point 21 | | +0.422 ± 0.013 | | -0.122 ± 0.028 | | +7.140 ± 0.053 | |

Table 12. Results and data from test A16-GA_0010.

| | UAV # | Mass (g) | Velocity (kts) | Target |
|---|---|---|---|---|
| | 22 | 1175.4 | 88 | Center |
| | Damage: Skid mark on center windscreen, elastic deformation only | | | |
| | Remarks: Direct hit on center windscreen / Pre load loss on LC #3 | | | |

| A16-GA_0010 | LC 0 (lbf) | LC 1 (lbf) | LC 2 (lbf) | LC 3 (lbf) | LC 4 (lbf) | LC 5 (lbf) | LC 6 (lbf) | LC 7 (lbf) |
|---|---|---|---|---|---|---|---|---|
| | 1373 ± 97 | 969 ± 110 | 883 ± 97 | 695 ± 99 | 287 ± 94 | 90 ± 94 | 1014 ± 98 | 959 ± 86 |
| | DIC Peak Location | | Deformation in x (mm) | | Deformation in y (mm) | | Deformation in z (mm) | |
| | Point 36 | | -0.107 ± 0.012 | | -0.132 ± 0.024 | | +48.672 ± 0.049 | |

Table 13. Results and data from test A16-GA_0011.

| | UAV # | Mass (g) | Velocity (kts) | Target |
|---|---|---|---|---|
| | 24 | 1194.3 | 103 | Center |
| | Damage: Small skid mark on high left windscreen | | | |
| | Remarks: Minimal collision, only motor #3 made contact | | | |

| A16-GA_0011 | LC 0 (lbf) | LC 1 (lbf) | LC 2 (lbf) | LC 3 (lbf) | LC 4 (lbf) | LC 5 (lbf) | LC 6 (lbf) | LC 7 (lbf) |
|---|---|---|---|---|---|---|---|---|
| | 843 ± 96 | 811 ± 110 | 661 ± 97 | 581 ± 99 | 496 ± 94 | 250 ± 94 | 348 ± 99 | 313 ± 86 |
| | DIC Peak Location | | Deformation in x (mm) | | Deformation in y (mm) | | Deformation in z (mm) | |
| | Point 3 | | -0.173 ± 0.013 | | -0.363 ± 0.028 | | +3.886 ± 0.055 | |

All windscreen tests that impacted the target unhindered resulted in minimal damage to the windscreen. No fractures occurred, and the only discernable damage on the windscreen was plastic residue deposited on the windscreen as the drone shell slid across it. Upon impact, the windscreen deflected inward and returned to its original form once the drone had glanced off. It is interesting to note however, that all but one of the tests that hit the plate fractured the windscreen and penetrated through. Test A16-GA_0010 resulted in the most accurate shot in the series, with the drone's center of mass perfectly centered on the windscreen. The UAV released on target, tumbling forward roughly 90° and rotating slightly to the right until impact. Motor #2 impacted first, soon followed by motor #1 and the center mass of the body. The impact can be seen below in figure 34.

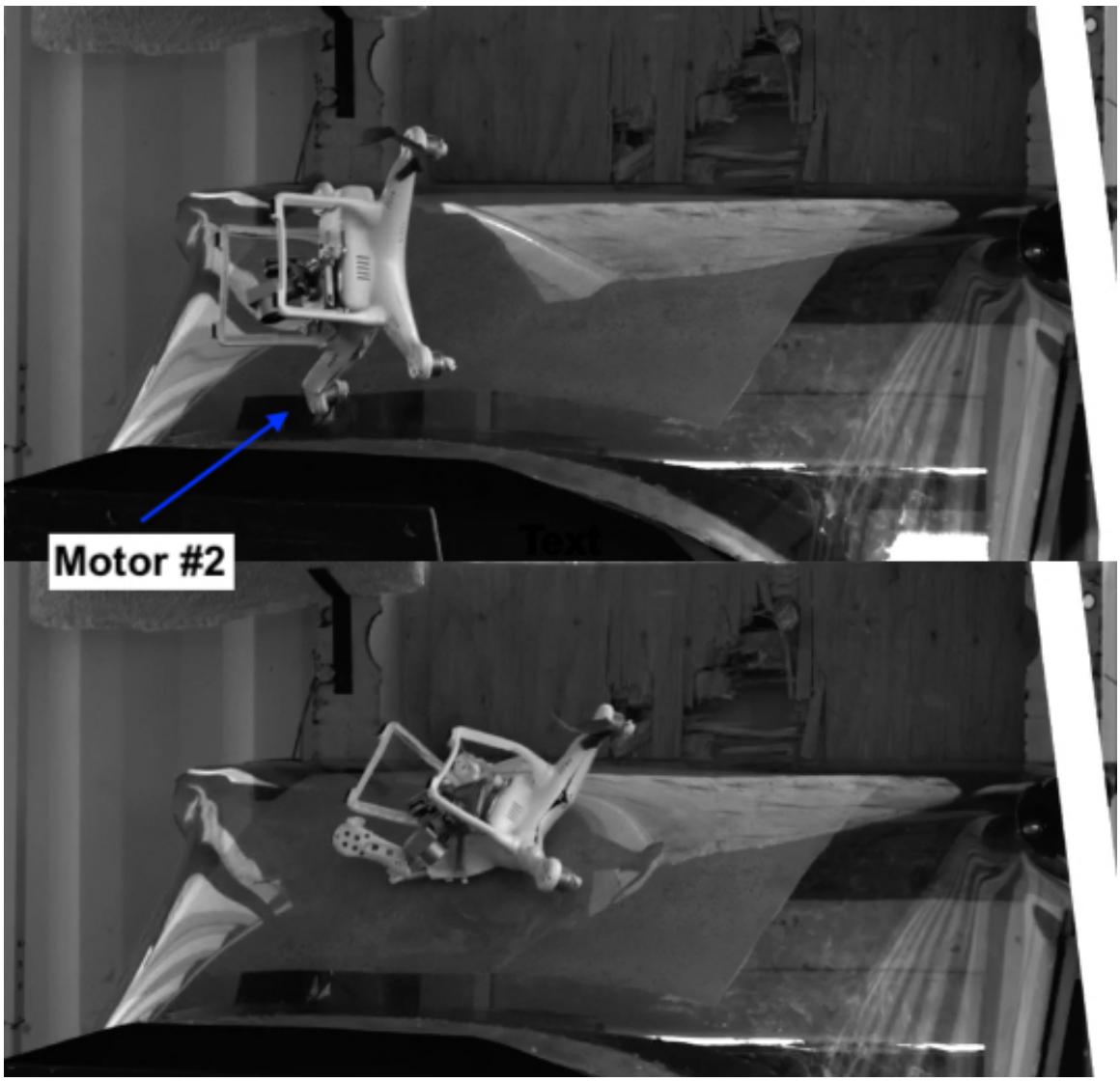



Figure 34. Crash sequence from test A16-GA_0010.

As seen above, the center mass of the UAV hit the center of the windscreen, causing significant elastic deformations to occur. Even with a direct hit, the windscreen again suffered only superficial damage. Similar to other tests, plastic residue from the drone components was transferred to the acrylic as the drone slide across the surface. Damage from test A16-GA_0010 is shown in figure 35 below.

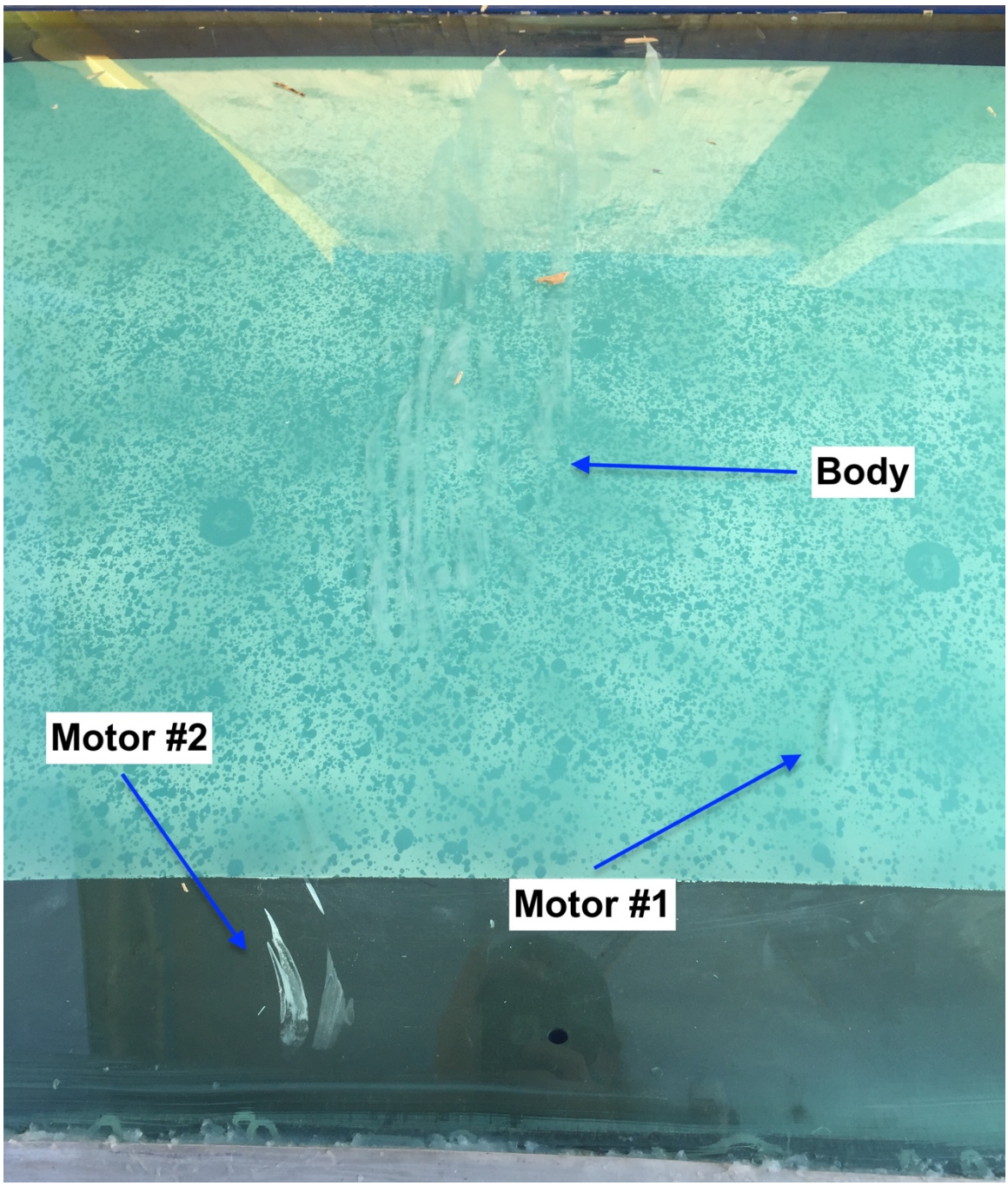



Figure 35. Damage from test A16-GA_0010.

Load cells captured reaction forces at each of the fixture interfaces and showed that for the majority of tests, the UAV's kinetic energy was distributed evenly through the structure. In some tests, significant loss of pre-load occurred at individual load cells.

As a result, there was likely an artificial reduction in peak loads in those cases. Force data from test A16-GA_0010 presented interesting results in the vertical direction, with load cells #6 and #7 reacting significantly more force than load cells #4 and #5. In the horizontal direction, reaction forces were distributed evenly. Reaction force plots are shown below in figure 36.

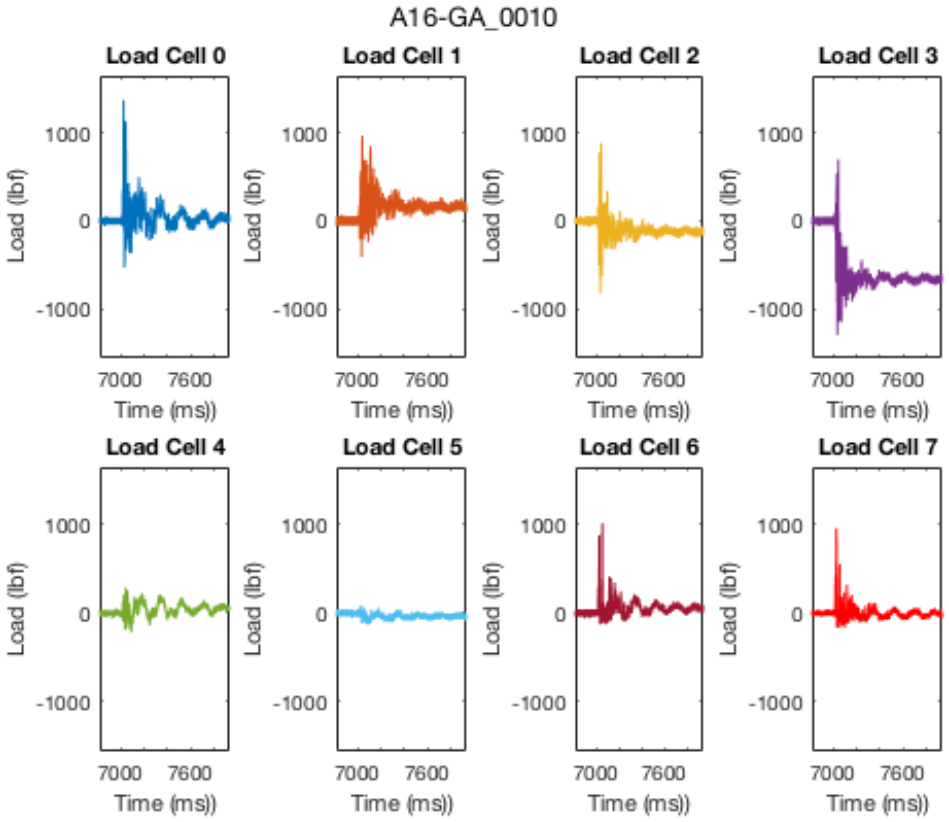



Figure 36. Load cell plots from Matlab for test A16-GA_0010.

The 3-D DIC system successfully captured windscreen deformations for each test at a high degree of accuracy. In several tests, the peak deformations of the windscreen were out of view of the cameras, resulting in maximum values occurring at the surface edges in GOM. For those tests, the deformation values presented are the maximum

values found at a facet points distance from the surface's edge in order to maintain accuracy. Test A16-GA_0010 was the best hit on a windscreen, and as a result the deformations recorded were significantly larger than in any other test, deflecting 48.672 mm in the z direction. Figure 37 shows the progression of the surface deformations throughout the impact. Plots and additional details for windscreen tests can be found in Appendix E.

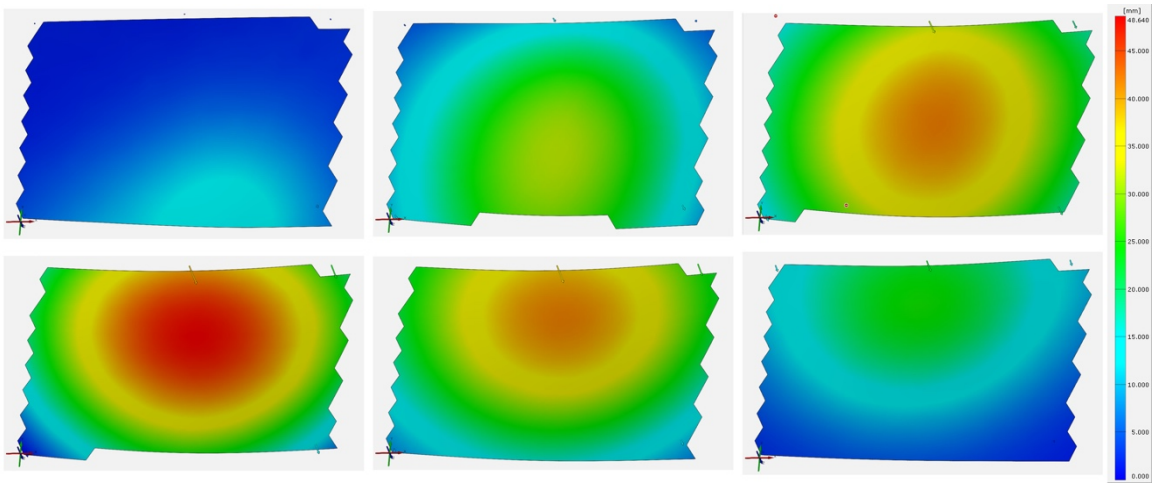



Figure 37. Deformation series of surface component in test A16-GA_0010.

Windscreen Testing Error

There are several sources of error that need to be addressed for windscreen testing. Error is separated into load cells and DIC below.

Load Cells. General sources of uncertainty in the data acquisition system were detailed earlier, and are shown with results. Sources of error in load measurements specific to windscreen testing are outlined in table 14 below and discussed.

Table 14. Sources of error in load cell data in windscreen testing and effects on results.

| Source of Error | Effect on Results |
|---|---|

| | |
|---|---|
| Fixture Binding | Reduction of peak loading and pre-load loss |
| Table Feet to Ground Interface | Reduction of peak loading |
| Off Axis Loading | Skewed results |
| Loss of Pre-Load | Reduction of peak loading |

- Fixture Binding. Fixture binding and slip proved to be a problem throughout windscreen testing. In several tests, pre-load was lost due to bolt binding as the fixture was assembled and pre-loaded. As can be seen in some of the load cells plots, loads drop sharply indicating a loss of pre-load. In tests where this occurred, there is a large increase in peak load uncertainty as it is difficult to tell whether the drop in load occurred after or during impact. Fixture binding in windscreen testing was likely a result of small amounts of mismatch between the holes on the fixture and holes on the I-beams, resulting in bolts not being totally perpendicular to the face of the I-beam flange when they were tightened. In addition to loss of pre-load, fixture binding may have also have impeded deflections of the load cell surface, in turn leading to recorded peak loads being reduced.
- Table Feet and Ground Interface. To create a rigid boundary condition, square cement pads were laid into the ground underneath each table leg at the test site. Pads were placed several weeks prior to testing to allow them to settle, but there is still the possibility that the pads were driven into the ground further during testing. This source of error is likely small, but would result in a reduction in peak loading.

- Off Axis Loading. Another source of error associated with the concrete pads is that they were likely not totally perpendicular to the table legs. When the pads were laid, they were made to be as level as possible. However, due to being outdoors, the pads may have shifted over time.
- Reduction in Pre-Load. Due to forces reacted through the fixture during collisions, several of the nut-bolt connections loosened over time during the test sequence. Both the bolts in the table feet and bolts connecting to the I-beams showed reductions in pre-load. To combat this, double locking nuts were used for bolt connections in test A16-GA_0009 on. The double locking nuts reduced pre-load loss from vibrations, but did not totally solve the problem. As a result, loss of pre-load was potentially a large source of error for results following the initial peak.

3-D DIC. Variance error was quantified for each test using the methods outlined earlier, and was presented with results. Additional sources of error in 3-D DIC measurement specific to windscreen testing are outlined in table 15 and discussed below.

Table 15. Sources of error in 3-D DIC for windscreen testing and effects on results.

| Source of Error | Effect on Results |
|---|---|
| Vibrations | Skewed results after first displacement peak |
| Ballistic Screen | Loss of calibration quality and increased variance error |
| Bias Errors | Skewed results |

- Vibrations. Error due to vibrations is one of the largest sources in windscreen testing. The camera bar holding the cameras was anchored to the floor of the shipping container in order to obtain a cockpit view of the windscreen as it

deformed. During each test sequence, a large shockwave of vibrations was sent through the container. As a result, the camera system does not remain perfectly steady throughout oscillations after the impact, causing increased uncertainty in measurements. However, the majority of vibrational error affects only the reverberations seen in the windscreen after the collision. Since the main quantity of interest is peak displacements, vibrations are likely a negligible source of error in peak measurements as the shipping container hasn't felt the main force of the UAV's impact yet.

- Protective Ballistic Screen. In order to protect the high speed camera system from collision debris, a new 3/8" extruded acrylic sheet was mounted in front of the cameras before calibration and testing each day. The addition of the acrylic in front of the cameras slightly obstructs the clarity of the cameras field of view, reducing the quality of the images captured. In turn, this results in a lower quality system calibration, decreasing by about 100% with the introduction of the ballistic screen. Even still, for almost all tests, calibration quality metrics were within the upper reaches of the systems acceptable range. As dust collects and settles on the ballistic screen over time, clarity is further impeded leading to an increased noise floor and difficulty in GOM tracking the speckle pattern at standard accuracy. To combat this, dust off was used to clear off the window before each test, but improvements to noise uncertainty were small. For tests where the same setup and windscreen was used multiple times, noise uncertainty increased for each test.

- Bias Errors. Another source of error in DIC measurements is bias error from camera drift, heating up of the cameras over time, small vibrations, and camera movement [13]. Bias errors are difficult to quantify since the true value being measured in often unknown. One metric for estimating bias error is studying how the mean values of static images change over time. A mean that changes over time can indicate the presence of bias errors. No bias errors were detected using this method in any 3-D DIC results. However, bias errors may still exist and must be acknowledged.

Windscreen Testing Conclusions

Windscreen testing showed that there is potential for catastrophic results if a Phantom 3 quadcopter impacts the windscreen of a Cessna 182B during flight. That being said, it is difficult to draw absolute conclusions without further testing. For low velocity impacts around 90 kts, testing showed only superficial damage. At most, damage consisted of skid marks of plastic residue imparted on the windscreen by the drone shell. The windscreen did however show significant elastic deformation on impacts in the center of the windscreen, deflecting almost 49 mm during test A16-GA_0010 and roughly 24 mm in test A16-GA_0008. In all tests, the UAV retained a significant portion of its kinetic energy post impact. This is mostly due to the angle of the windscreen, glancing the UAV up and over into the backstop. Given this, the severity of such a collision is low and would not likely result in a downed plane. The chances of such a collision occurring however, are very small given the fact that the UAV would have to pass through the spinning prop of the plane unscathed. The most likely case

would be the UAV impacting the prop, and debris or sections of it impacting the windscreen rather than the fully in tact drone. Further testing would be needed to evaluate the severity of a UAV to prop collision.

One of the goals of windscreen testing was to provide data to NIAR for FE model validation. As a result, successful tests were defined as the UAV impacting the windscreen fully in tact with its path unaltered. At high velocity speeds, we were unable to achieve a successful test given the narrow target window and a reduction in launcher accuracy with increased speed. On all high speed tests the projectile either missed the target high, or released just low resulting in one arm of the UAV impacting the protective plate in front of the fixture. Interestingly, all but one of these tests resulted in failure of the windscreen. Details on tests where the UAV impacted the plate on its approach can be found in the appendix. For all of these tests, the tip of one arm caught the plate, accelerating the spin of the drone until it impacted and penetrated the lower half of the windscreen. All yielded very similar results, implying that impact location may be an important determining factor in whether or not the windscreen fails. The lower portion of the windscreen has the steepest angle ~ 50° so it would make sense that a hit lower on the windscreen would result in a larger transfer of energy than the upper portion. It is difficult to draw any conclusions about whether a fragmented UAV has a higher chance of causing failure than one that is in tact at time of collision. It is worth noting however that for every test that penetration occurred, the body of the UAV had begun to split at time of impact.

To draw additional conclusions about the severity of UAV to windscreen impacts and calculate a threshold for failure, more testing is needed. Due to accuracy limitations with the UAV launcher, optimal results for model validation could only be obtained for low velocity testing. Testing showed that low velocity impacts cause minimal damage to C-182B windscreens, with only elastic deformations being detected. However, damage was likely dependent on impact location, with a greater potential for failure on the lower edge of the windscreen. To draw further conclusions, a launcher setup with greater precision is required.

## Cessna 182B Tilted Windscreen Penetration Test

To capture an unimpeded windscreen penetration, a special windscreen test was performed. The goal of this test was to capture a penetrating windscreen impact with high speed footage only and document the damage. In order to increase the likelihood of a direct hit to the windscreen, the target window was opened up by tilting the shipping container forward by 20° during the test. As a result, load cell and DIC data collection was not possible and only high speed footage was to be captured. Test site layout was identical to normal windscreen testing. The windscreen fixture was mounted to the I-beams, the table was then removed, and the whole container tipped forward with a winch. Test setup can be seen in figure 38 below.




Figure 38. Test setup for tilted windscreen penetration test.

Tilted Windscreen Testing Results

For test A16-GA_0014, UAV # 26 was used with a mass of 1178.4 g. Measured at the I-beams, the tilt of the container was 20.2°, increasing the target window significantly. The UAV was launched with a velocity of 86 knots, and impacted the center of the windscreen. The collision can be seen in figure 39 below.

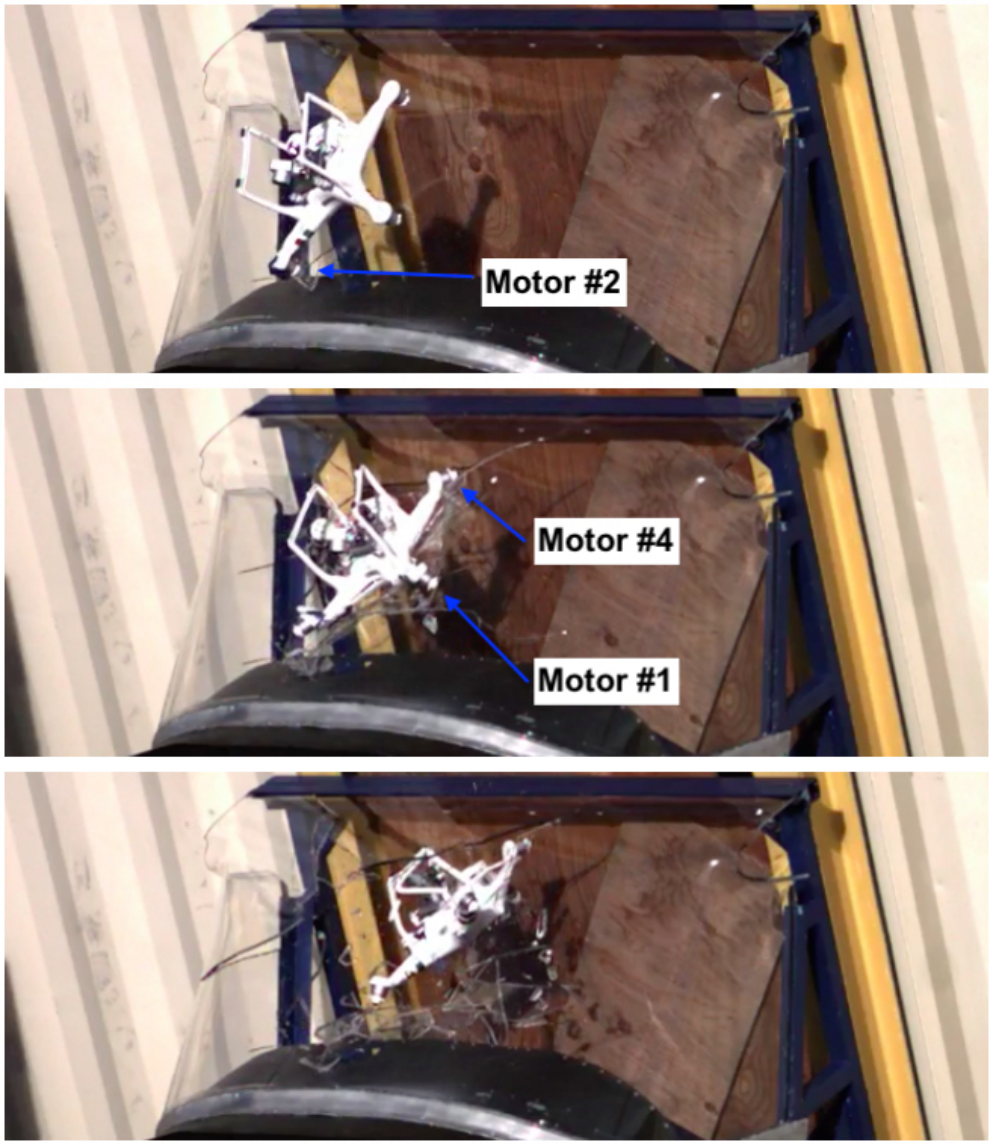



Figure 39. Crash sequence for test A16-GA_0014.

After release from the launcher, the drone tumbled forwards about 100°, and impacted the center of the windscreen with the top of motor #2 first, followed by motor #1, motor #4, then the rest of the body. Upon impact, a fracture occurred at each of the motor contact points. The UAV passed clean through the windscreen and impacted the

backstop. Interestingly, three distinct notches were present where motors #2, #3, and #4 passed through the windscreen. Damage can be seen in figure 40 below.

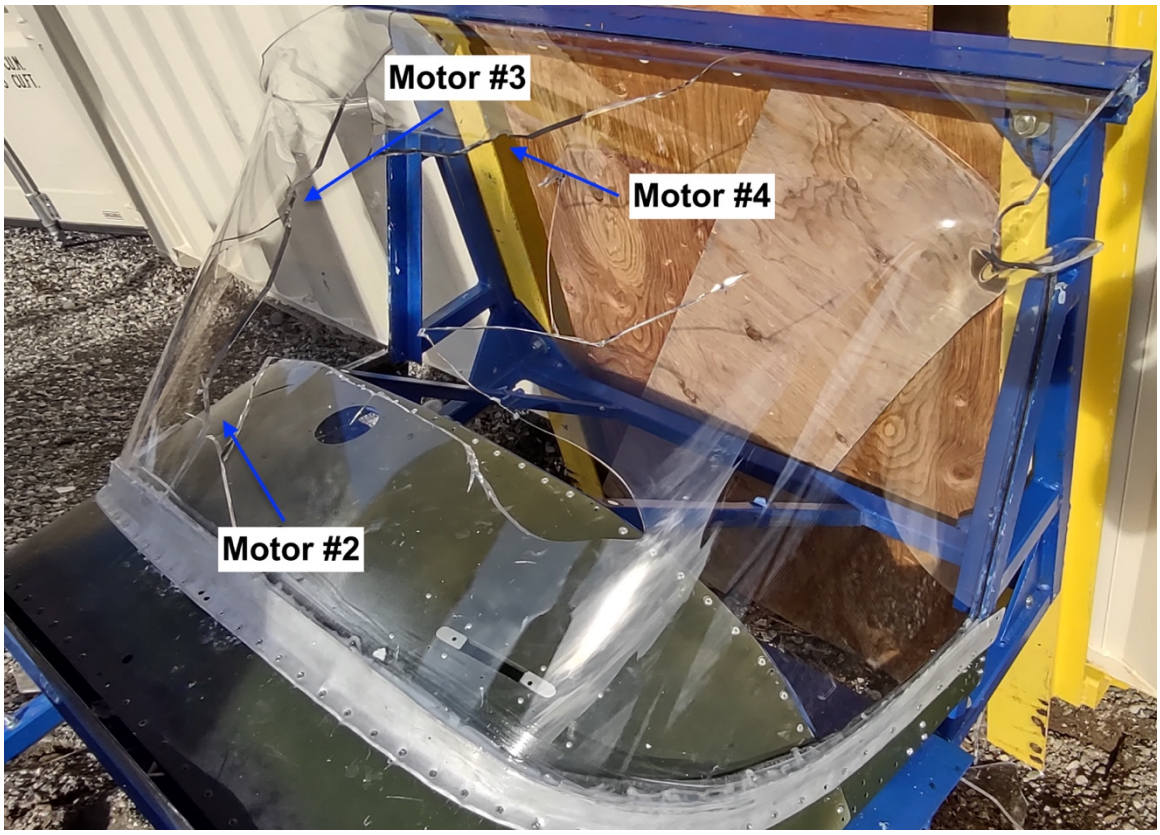



Figure 40. Damage from penetration test A16-GA_0014.

Windscreen Penetration Test Conclusions

Tilted windscreen testing showed that penetration of the windscreen is possible at lower impact speeds. Although these tests were not representative of in flight geometry, they provide useful insight into factors that can influence whether or not penetration occurs. It is clear that the chances of failure in the acrylic increase as the windscreen becomes more vertical, potentially corroborating the results seen in the full scale windscreen tests. Orientation of the UAV may also be a factor that affects penetration.

Failure occurred at each of the motor contact points upon impact, suggesting that a direct hit with the motor first may increase chances of failure. That being said, motor to windscreen collisions in full scale tests did not always cause a fracture so it seems that the largest factors influencing penetration are likely the location of the hit and momentum of the projectile. Given that the test setup is not representative of in flight geometry, it is difficult to use these results to assess the danger of an in flight collision. These results do however shed some light on factors that may influence penetration, but more testing would be needed to draw any hard conclusions.

# SUMMARY AND CONCLUSIONS

UAS are more popular now than ever before, and it is crucial to understand the risks they pose to other aircraft occupying the same airspace. In order to evaluate these risks, ASSURE was created to determine the severity of air to air collisions involving UAS. Due to the high cost of full scale testing, finite element models (NIAR) are to be used in conjunction with full scale test results to validate and aid in development. Once a model is proven to be accurate, it can then be adapted for other collision cases thus saving money and reducing the need for additional testing. As part of the project, Montana State University was contracted to develop and carry out component level testing for C-182B single prop planes. This work is the continuation of Forrest Arnold's masters thesis, in which a windscreen material model and a full scale testing facility was created.

In order to carry out component level testing, test fixtures along with representative CAD models were developed to mimic the in flight geometry of the plane for each component. Fixtures were designed to allow for force and displacement data to be collected at critical points in the structure. Fixtures for mounting struts, wings, and windscreens were developed and incorporated into the test facility for use with the UAV launcher. Reaction forces along with displacement data and high speed video were successfully captured for each test, and collision severity was evaluated for each test article.

Measurement uncertainty was found for all data acquisition systems used in testing. By quantifying uncertainty, the trustworthiness of results was evaluated and data

from these tests can be meaningfully compared to those from other research projects. Results from uncertainty analysis showed that for most tests, load results were accurate within ~100 lbf for 10k load cells and ~500 lbf for 50k load cells. For DIC, 2-D analysis showed that results were accurate within 0.45mm. For 3-D DIC, analysis showed that most results were accurate within 0.01mm. Although the true values of results are likely within these bounds, additional sources of error in testing were outlined and may have influenced results.

Cessna 182B component level impact testing showed that there is potential for catastrophic failure if a plane were to impact a Phantom 3 quadcopter either mid flight or at takeoff or landing. Strut testing showed that there is cause for concern if impacted. When hit by a UAV at ~ 120 knots, struts showed light structural damage, consisting of small deformations in the aluminum and scratches to the paint. Although the deformations seen were small, there is the potential for local buckling to occur at the dents when the strut is under a compressive load. Due to the small number of tests conducted, there is not enough evidence to make hard conclusions about the severity of the damage recorded. Additional testing would be required to determine if the deformations seen may result in buckling failure of the strut during flight.

Wings proved to have a high potential for catastrophic failure. Testing showed that significant damage would be sustained from a direct hit with a UAV at takeoff velocities of ~ 95 knots. Major structural deformation and tearing of the wing skin occurred from a direct hit, making this scenario a cause for concern. Using the severity

criteria developed by NIAR for their wing testing, level 3 damage was sustained in all tests making wings a primary area for concern in an air to air collision.

Windscreen testing proved to be the most difficult given the small target window. Due to underperformance of the launcher, neither a high velocity or penetrating hit was able to be obtained without the UAV hitting adjacent structure on its approach. Several hits at lower speeds of ~ 90 knots were recorded but did not penetrate, instead deflecting off the top edge of the windscreen and retaining significant kinetic energy after impact. Damage in these tests consisted of elastic deformations to the windscreen and skid marks of plastic residue imparted on the windscreen by the drone shell. No permanent structural damage was observed in tests where the UAV made its approach unimpeded. In the three tests where failure of the windscreen did occur, the UAV impacted adjacent structure just before the windscreen, causing the loss of an arm and slight separation to occur in the UAV body. All of these impacts occurred in the lower half of the windscreen where its slope is steepest, indicating a possible correlation between impact location and failure. Windscreen testing showed that there is potential for catastrophic failure, possibly increasing in likelihood if impacted on the lower portion of the windscreen.

To collect footage of a windscreen penetration with the UAV path unaltered, a special test was performed at ~ 85 knots with only high speed footage collected and the fixture tilted forwards to increase the target window. The UAV penetrated clean through the center of the windscreen, further indicating that windscreen gradient affects whether failure occurs.

Experimental results and CAD models from component level testing were shared with NIAR for use in FE model validation and development. Using the test fixture CAD models created at MSU combined with models developed at NIAR from 3-D scanned aircraft components, test scenarios were created for wing and windscreens. Using the high speed video, damage, reaction forces, and displacement data for reference, FE models were evaluated and tweaked by the engineers at NIAR until results matched closely. Side by side comparisons between the FE models and test footage are shown in figures 41- 43 below, videos of the simulations can be found in the supplementary files.

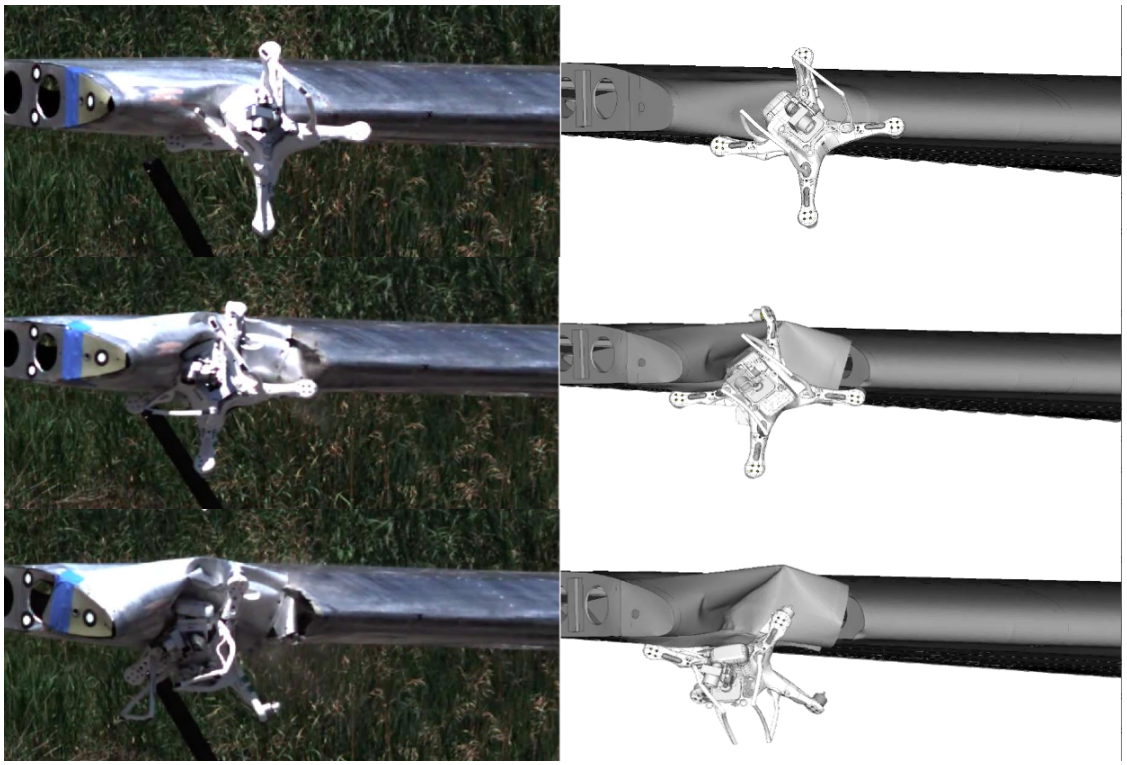


Figure 41. A16-GA_0003 collision footage side by side with FE model from NIAR [27].

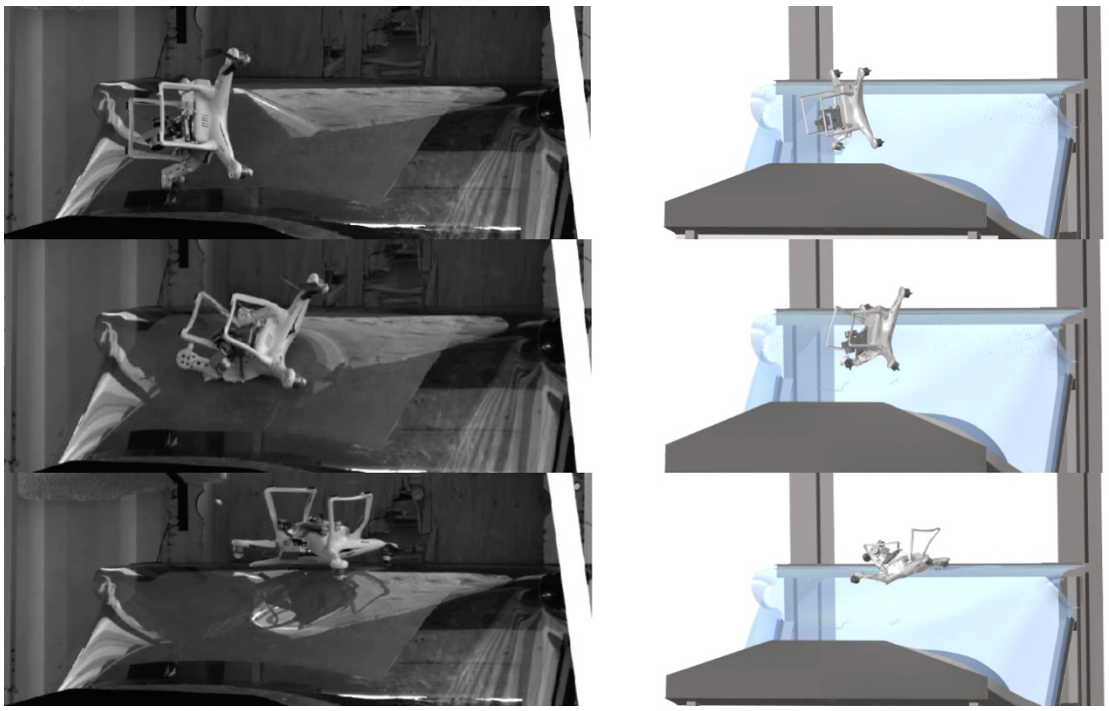


Figure 42. A16-GA_0010 collision footage side by side with FE model from NIAR [27].

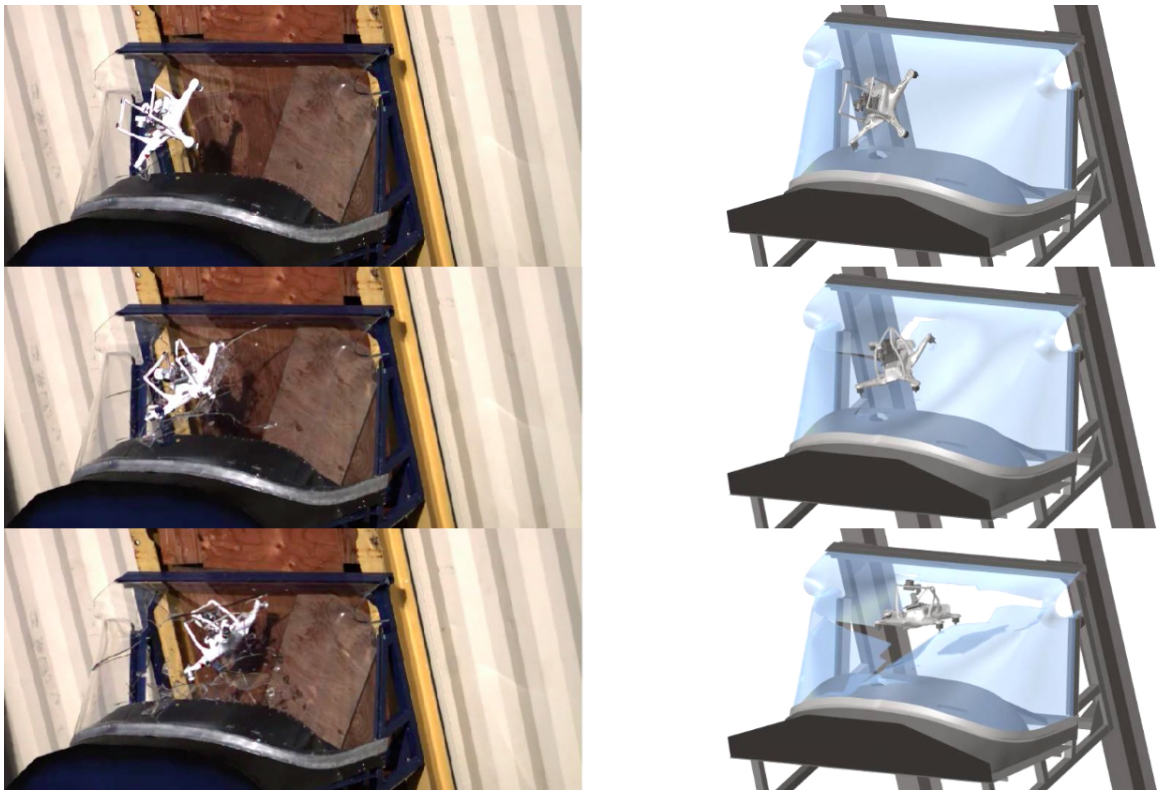


Figure 43. A16-GA_0014 collision footage side by side with FE model from NIAR [27].

As seen in figures 41-43, test results for both wings and windscreens were successfully recreated with FE models to a high degree of accuracy. With models confirmed, new test scenarios may be analyzed without the need for additional full scale testing. The results from simulations of alternate crash scenarios will further shed light on the severity of air to air collisions between UAV and single-prop aircraft. Using these results, officials can make more informed policy and regulatory decisions regarding air space safety. These decisions will be crucial in maintaining a safe and controlled airspace as UAS become more prevalent.

# FUTURE WORK

Montana State University's research contribution to ASSURE's A16 airborne collision work was completed May 2021. However, there is still more work to be done in evaluating the severity of air to air collisions between UAS and aircraft. Now that data from testing has confirmed the FE models developed at NIAR, additional impact scenarios will need to be simulated and evaluated to better characterize damage potential. Other C-182B impact scenarios to be analyzed include: alternate wing locations, tailpieces, control surfaces, and a spinning prop. Furthermore, collisions between other models of popular UAS will need to be developed and analyzed.

# REFERENCES CITED

[1] Lykou, G., Moustakas, D., & Gritzalis, D. (2020). Defending Airports from UAS: A Survey on Cyber-Attacks and Counter-Drone Sensing Technologies. *Sensors (Basel, Switzerland)*, *20*(12), 3537. https://doi.org/10.3390/s20123537

[2] Drone market to grow from $22.5 billion in 2020 to Over $42.8 billion by 2025, at a CAGR of 13.8% - ResearchAndMarkets.com. (2020, July 21). Retrieved February 22, 2021, from https://www.businesswire.com/news/home/20200721005593/en/Drone-Market-to-Grow-from-22.5-Billion-in-2020-to-Over-42.8-Billion-by-2025-at-a-CAGR-of-13.8---ResearchAndMarkets.com#:~:text=According%20to%20the%20Drone%20Market,at%20a%20CAGR%20of%2013.8%25.

[3] Werner, C. (2019, April 09). The challenges and potential dangers of drones. Retrieved February 22, 2021, from https://www.govloop.com/community/blog/the-challenges-and-potential-dangers-of-drones/

[4] U.S.Cong. (n.d.). *FAA Reauthorization Act of 2018* [Cong. H.R.302 from 115th Cong., 2nd sess.]. Retrieved February 22, 2021, from https://www.congress.gov/115/bills/hr302/BILLS-115hr302enr.pdf.

[5] Unmanned aircraft Systems (UAS). (2021, February 05). Retrieved February 22, 2021, from https://www.faa.gov/uas/

[6] ASSURE About Us. (n.d.). Retrieved February 24, 2021, from https://www.assureuas.org/about.php

[7] G. Olivares, L. Gomez, J. Espinosa de los Monteros, R. Baldridge, C. Zinzuwadia and T. Aldag, "Volume II - UAS Airborne Collision Severity Evaluation - Quadcopter," July 2017. [Online]. Available: http://www.assureuas.org/projects/deliverables/a3/Volume%20II%20-%20UAS%20Airborne%20Collision%20Severity%20Evaluation%20-%20Quadcopter.pdf.

[8] D. S. Cairns and G. Johnson, "Volume I - UAS Airborne Collision Severity - Projectile and Target Definitions," 16 December 2016. [Online]. Available: http://www.assureuas.org/projects/deliverables/a3/Volume%20I%20UAS%20Airborne%20Collision%20Severity%20Projectile%20and%20Target%20Definition.pdf.

[9] Arnold, F., 2020, “CESSNA 182B WINDSCREEN MATERIAL MODEL DEVELOPMENT AND FULL SCALE UAS TO AIRCRAFT IMPACT TESTING FACILITY”, M.S. thesis, M&IE, Montana State University.

[10] Momentum change and impulse. (n.d.). Retrieved February 24, 2021, from https://www.physicsclassroom.com/class/momentum/Lesson-1/Momentum-and-Impulse-Connection#:~:text=In%20a%20collision%2C%20objects%20experience,speed%20and%20thus%20his%20momentum.

[11] Trent, D. (n.d.). Strain gauge load cell basics. Retrieved February 24, 2021, from https://www.800loadcel.com/load-cell-and-strain-gauge-basics.html

[12] Kopczynski, T. (n.d.). Five Factors That Can Affect Your Weighing System's Accuracy. Retrieved January 14, 2021, from https://www.hardysolutions.com/tenants/hardy/documents/5FactorsA.pdf

[13] International Digital Image Correlation Society, Jones, E.M.C. and Iadicola, M.A. (Eds.) (2018). A Good Practices Guide for Digital Image Correlation. https://doi.org/10.32720/idics/gpg.ed1/print.format.

[14] Pickerd, V. (2013). *Optimisation and Validation of the ARAMIS Digital Image Correlation System for use in Large-scale High Strain-rate Events* (Australia, Department of Defense, Defense Science and Technology Organisation). Fishermans Bend, Victoria, Australia: Maritime Division Defence Science and Technology Organisation.

[15] *GOM Correlate Professional V8 SR1 Manual Basic* [PDF]. (2015). Braunschweig, Germany: GOM mbh.

[16] THROUGH HOLE DONUT LOAD CELL (2.00 O.D.) COMPRESSION ONLY. (n.d.). Retrieved March 1, 2021, from https://www.transducertechniques.com/thc-load-cell.aspx

[17] A. Farr, M. Mercer, and L. O'Rourke, *FAA Wing/Strut Testing Fixture Technical Addendum,* Montana State University, 2020.

[18] A. Farr, M. Mercer, and L. O'Rourke, *FAA Drone Wing Testing Fixture Final Report,* Montana State University, 2020.

[19] THROUGH HOLE DONUT LOAD CELL (3.00 O.D.) COMPRESSION ONLY. (n.d.). Retrieved January 15, 2021, from https://www.transducertechniques.com/thd-load-cell.aspx

[20] *Cessna Model 182 Illustrated Parts Manual* [Pamphlet]. (1972). Wichita, Kansas: Cessna Aircraft Company, Commercial Aircraft Division.

[21] Dadouche, A., Greer, A., Galeote, B., Breithaupt, T., Vidal, C., & Gould, R. (2020). *Drone impact assessment on aircraft structure: Windshield and leading edge testing and analysis* (Vol. 2, Tech.). National Research Council of Canada. Aerospace Research Centre. doi:https://doi.org/10.4224/40001907

[22] "DataSheet NI 9205," 4 July 2017. [Online]. Available: https://www.ni.com/pdf/manuals/378020a_02.pdf.

[23] Can you lead Planephd.com to be an industry game-changer? (n.d.). Retrieved January 21, 2021, from https://planephd.com/wizard/details/229/CESSNA-182B-Skylane-specifications-performance-operating-cost-valuation

[24] By, Everett. 2014. "Noise and Drift in Load Cells." *Phidgets*. May 8. https://phidgets.wordpress.com/2014/05/12/noise-and-drift-in-load-cells/.

[25] Thorsten Siebert, Thomas Becker, Karsten Splitthof, Isabell Neumann, René Krupka, "High-speed digital image correlation: error estimations and applications," Opt. Eng. 46(5) 051004 (1 May 2007) https://doi.org/10.1117/1.2741217

[26] BK Precision. (2014). *Data Sheet, Triple Output Power Supplies Models 1672 & 1673*. https://bkpmedia.s3.amazonaws.com/downloads/datasheets/en-us/167x_datasheet.pdf.

[27] Olivares, G., et all, "UAS Airborne Collision Severity Evaluation – General Aviation", ASSURE A16 Report, To be Published 2021

[28] Houliara, Sotiria & Karamanos, Spyros. (2011). Buckling of Thin-Walled Long Steel Cylinders Subjected to Bending. Journal of Pressure Vessel Technology. 133. 011201. 10.1115/1.4002902.

[29] Çerik, Burak & Cho, Sang-Rai. (2013). Residual strength of damaged stiffened cylinders under combined axial compression and radial pressure.

[30] "Raise of the Drones. Managing the Unique Risks Associated with Unmanned Aircraft Systems", Alliance Global Corporate & Specialty, 2016.

[31] FAA Advisory Circular AC 107-2, "Small Unmanned Aircraft System (sUAS)", Washington, DC, 2016.

[32] Dalamagkidis, K., Valavanis, K., and Piegl, L. A., On Integrating Unmanned Aircraft Systems into the National Airspace System, 2 nd ed., Springer Netherlands, 2012.

[33] Lum, C. W., and Waggoner, B., "A Risk Based Paradigm and Model for Unmanned Aerial Systems in the National Airspace", Infotech@Aerospace Conferences, 2011-1424, AIAA, St. Louis, MO, 2011.

[34] McGeer, T., Newcome, L., and Vagners, J., "Quantitative Risk Management as a Regulatory Approach to Civil UAVs", International Workshop on UAV Certification, 1999.

[35] Civil Aviation Safety Authority, "Potential Damage Assessment of a Mid-Air Collision with a Small UAV", Technical Report, 2013.

[36] Jimenez, H., Mavris, D., Hoffman, D., Mines, J., and O'Sullivan, S., "A Survey of Evaluation Methods for Unmanned Aircraft Risk and Safety to Third Parties", Report, Federal Aviation Administration, 2015.

[37] Meng Xianghao, Yingjun Sun, Jingyu Yu, Zhongbin Tang, Jun Liu, Suo Tao and Yulong Li. 2018 Dynamic Response of the Horizontal Stabilizer During UAS Airborne Collision [J] *International Journal of Impact Engineering*

[38] Yongjie1, Z., Zhiwen1, L., Yingjie1, H., Kang1, C., Yafeng2, W., Yazhou2, G., … Xiaochuan2, L. (2021, February 1). *A Review of Impact Tests of Light and Small UAV*. Journal of Physics: Conference Series. https://iopscience.iop.org/article/10.1088/1742-6596/1786/1/012039/meta.

[39] Reu, P. L., & Miller, T. J. (2008). The application of high-speed digital image correlation. The Journal of Strain Analysis for Engineering Design, 43(8), 673–688. https://doi.org/10.1243/03093247JSA414

[40] Authority, C. A. S. (2013). *Potential damage assessment of a mid-air collision with a small UAV*. Technical Report.

[41] Jenkins, D., & Vasigh, B. (2013). *The economic impact of unmanned aircraft systems integration in the United States*. Association for Unmanned Vehicle Systems International (AUVSI).

[42] Pan, Bing & Yu, Liping & Yang, Yongqi & Song, Weidong & Guo, Licheng. (2016). Full-field transient 3D deformation measurement of 3D braided composite panels during ballistic impact using single-camera high-speed stereo-digital image correlation. Composite Structures. 157. 10.1016/j.compstruct.2016.08.017.

[43] Weibel, R. E., & Hansman, R. J. (2006, November 21). Safety Considerations for Operation of Unmanned Aerial Vehicles in the National Airspace System. https://dspace.mit.edu/handle/1721.1/34912.

# APPENDICES

# APPENDIX A

## TESTING LAUNCH DATA

Table 16. Launch data from testing.

| Test # | Date | UAV # | UAV Mass (g) | Velocity (knots) | Orientation At Impact | | |
|---|---|---|---|---|---|---|---|
| | | | | | Nose Up Positive | Right Up Positive | CCW Positive (From Above) |
| A16-GA_0001 | 7/7/20 | 1 | 1186.4 | 129 | -5 | -15 | 75 |
| A16-GA_0002 | 7/21/20 | 10 | 1173.9 | 116 | -135 | 30 | -15 |
| A16-GA_0003 | 8/4/20 | 5 | 1175.3 | 94 | -45 | 30 | -15 |
| A16-GA_0004 | 8/4/20 | 6 | 1181.8 | 98 | 190 | -10 | -15 |
| A16-GA_0005 | 9/4/20 | 11 | 1175.4 | 110 | / | / | / |
| A16-GA_0006 | 9/11/20 | 20 | 1168.3 | 110 | / | / | / |
| A16-GA_0007 | 9/18/20 | 18 | 365 | 71 | / | / | / |
| A16-GA_0008 | 9/18/20 | 16 | 1188 | 88 | 180 | 15 | 15 |
| A16-GA_0009 | 9/18/20 | 12 | 1157.3 | 87 | 190 | -45 | -15 |
| A16-GA_0010 | 10/2/20 | 22 | 1175.4 | 88 | -100 | 30 | -15 |
| A16-GA_0011 | 10/2/20 | 24 | 1194.3 | 103 | 170 | 30 | 15 |
| A16-GA_0012 | 10/2/20 | 17 | 1176.6 | 105 | / | / | / |
| A16-GA_0013 | 11/6/20 | 25 | 1176.1 | 81 | 180 | -90 | -15 |
| A16-GA_0014 | 12/8/20 | 26 | 1178.4 | 86 | -45 | 45 | -15 |

# APPENDIX B

## TEST FIXTURE DRAWINGS AND MATERIAL LISTS

Strut Testing Fixture

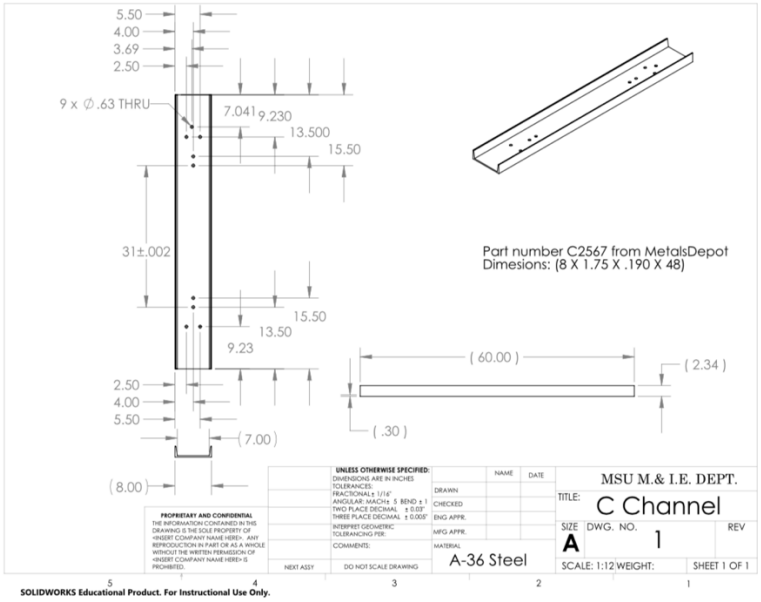



Figure 44. Engineering drawing of c-channel for strut testing fixture from Capstone Technical Addendum [17].

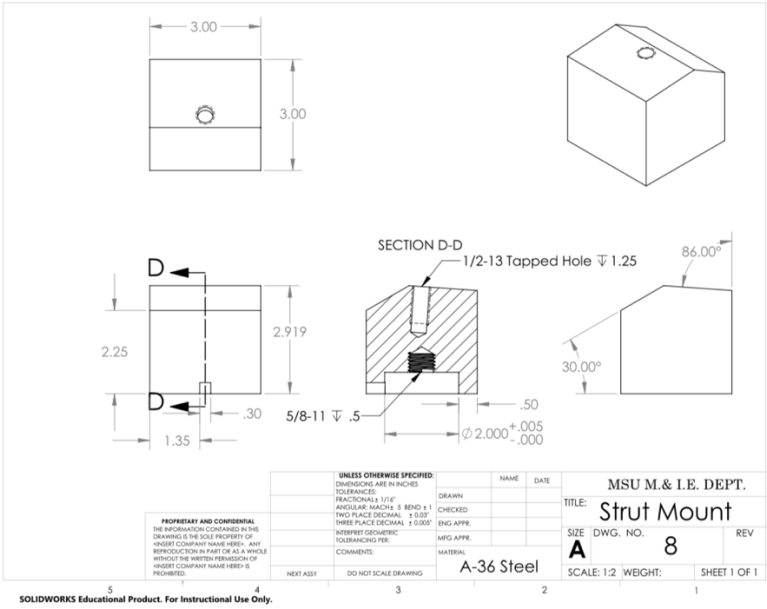



Figure 45. Engineering drawing of strut mount for strut testing fixture from Capstone Technical Addendum [17].

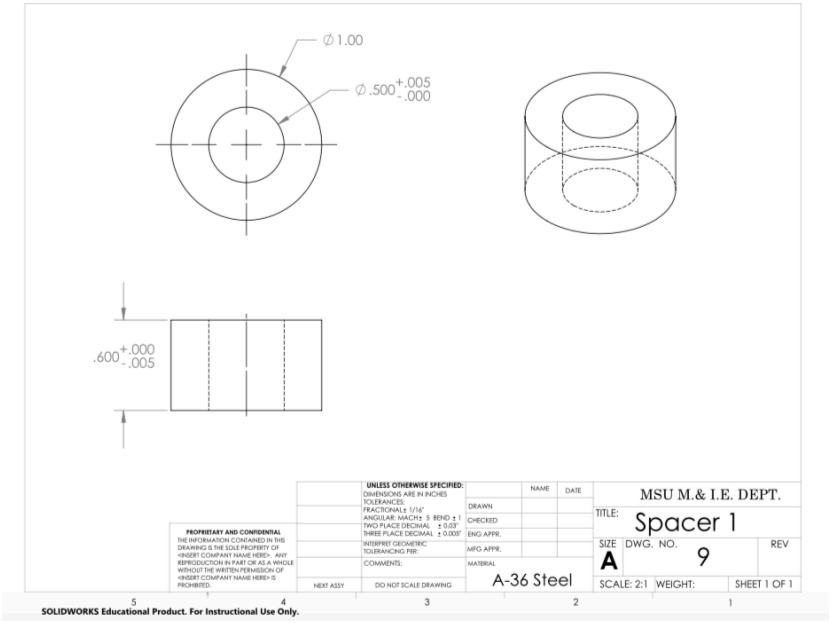



Figure 46. Engineering drawing of spacer 1 for strut testing fixture from Capstone Technical Addendum [17].

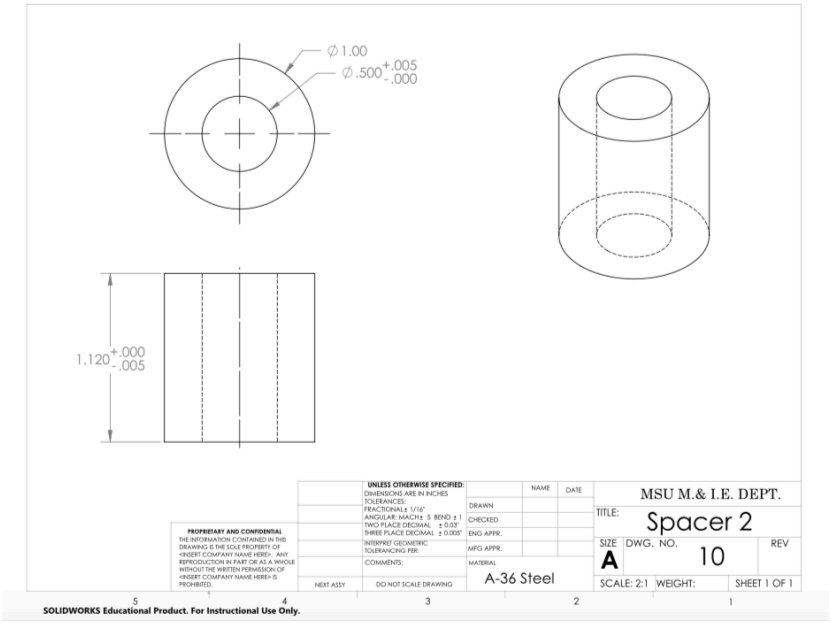



Figure 47. Engineering drawing of spacer 2 for strut testing fixture from Capstone Technical Addendum [17].

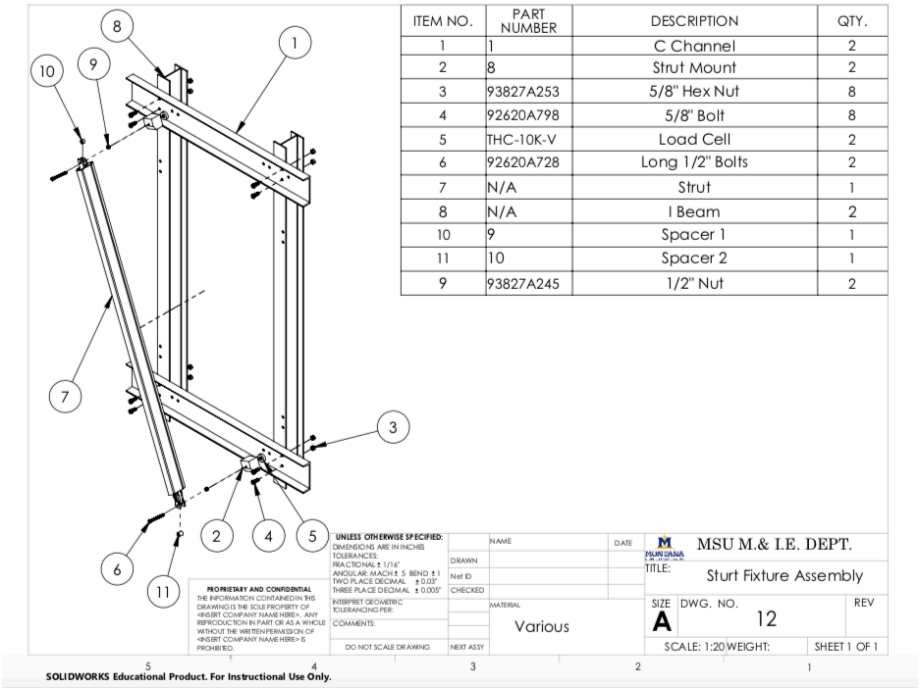



Figure 48. Engineering drawing of strut fixture assembly from Capstone Technical Addendum [17].

Wing Testing Fixture

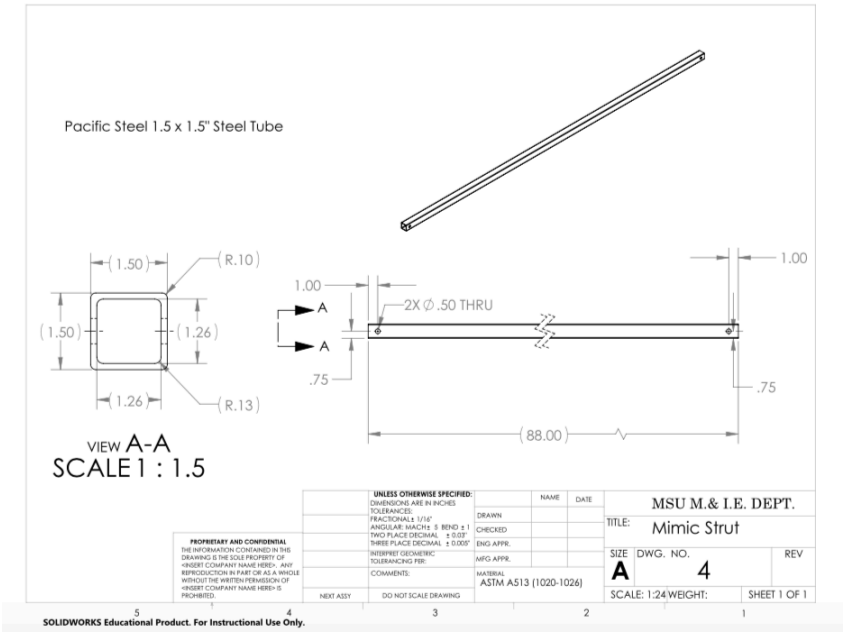



Figure 49. Engineering drawing of mimic strut for wing testing fixture from Capstone Technical Addendum [17].

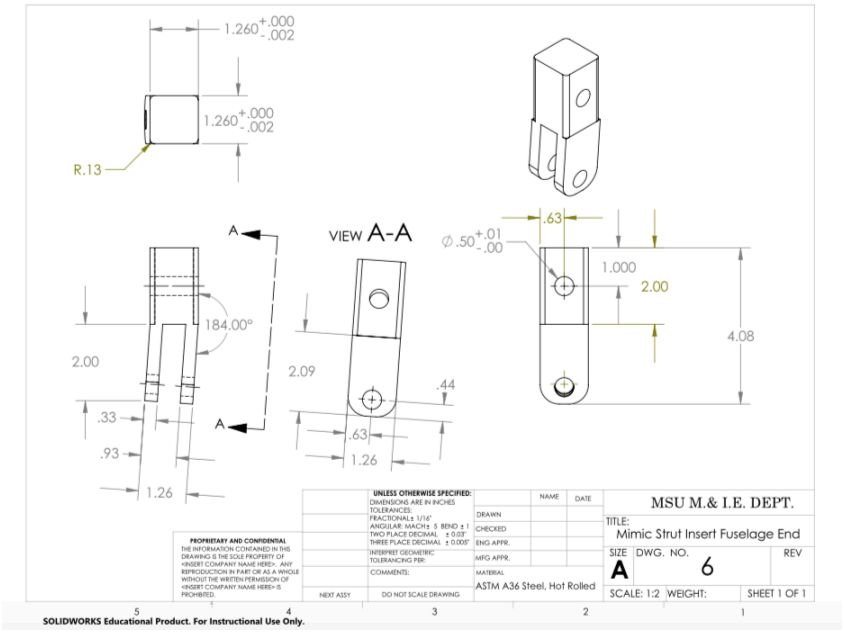



Figure 50. Engineering drawing of mimic strut insert at fuselage end for wing testing fixture from Capstone Technical Addendum [17].

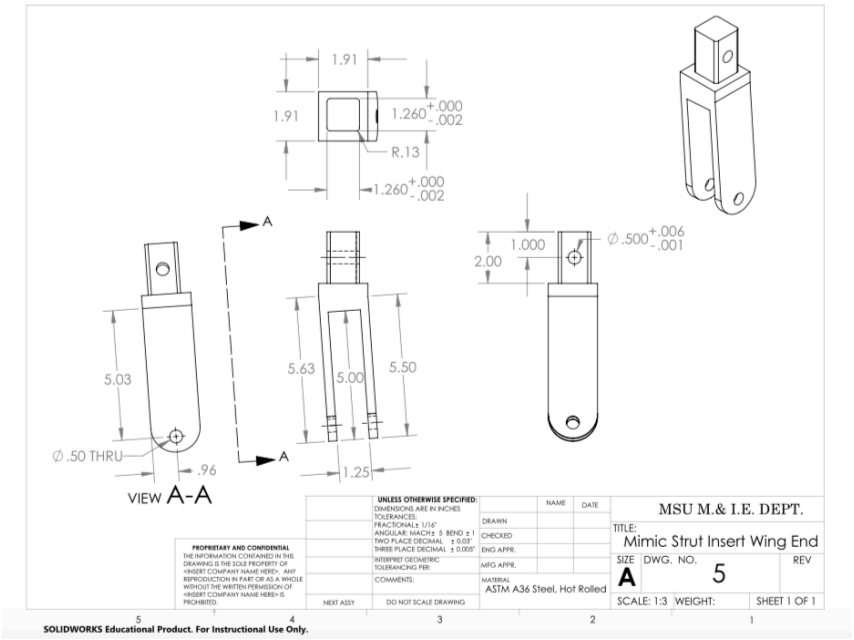



Figure 51. Engineering drawing of mimic strut insert at wing end for wing testing fixture from Capstone Technical Addendum [17].

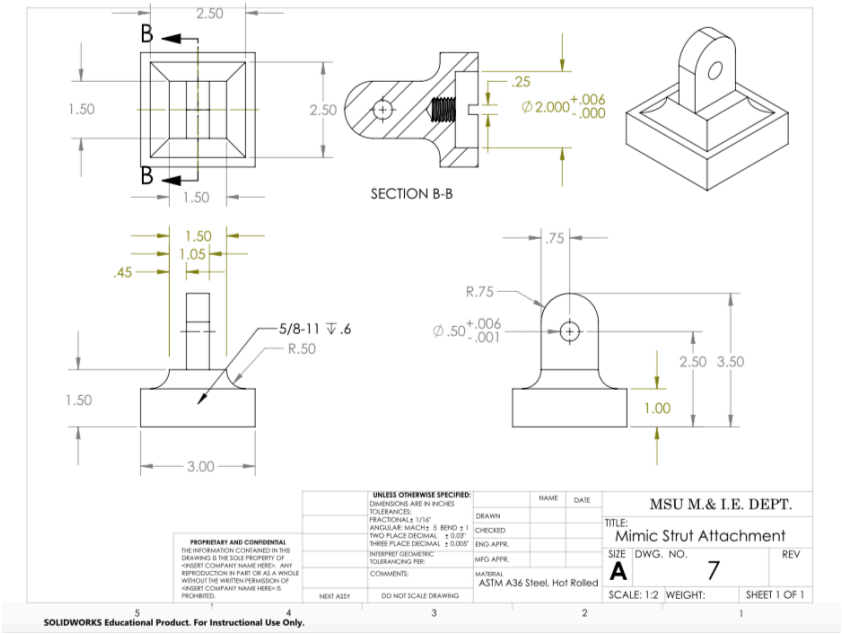



Figure 52. Engineering drawing of mimic strut attachment at c-channel for wing testing fixture from Capstone Technical Addendum [17].

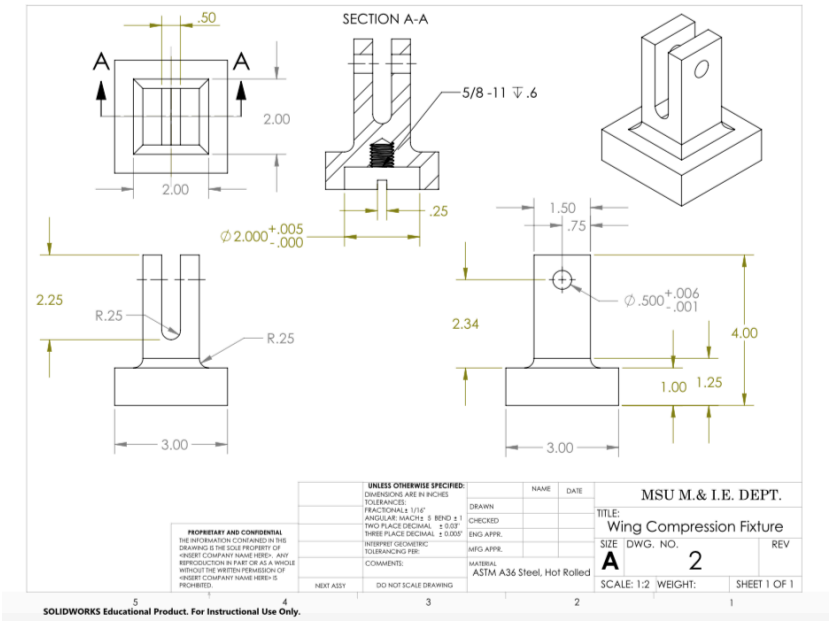



Figure 53. Engineering drawing of wing to c-channel attachment at trailing edge for wing testing fixture from Capstone Technical Addendum [17].

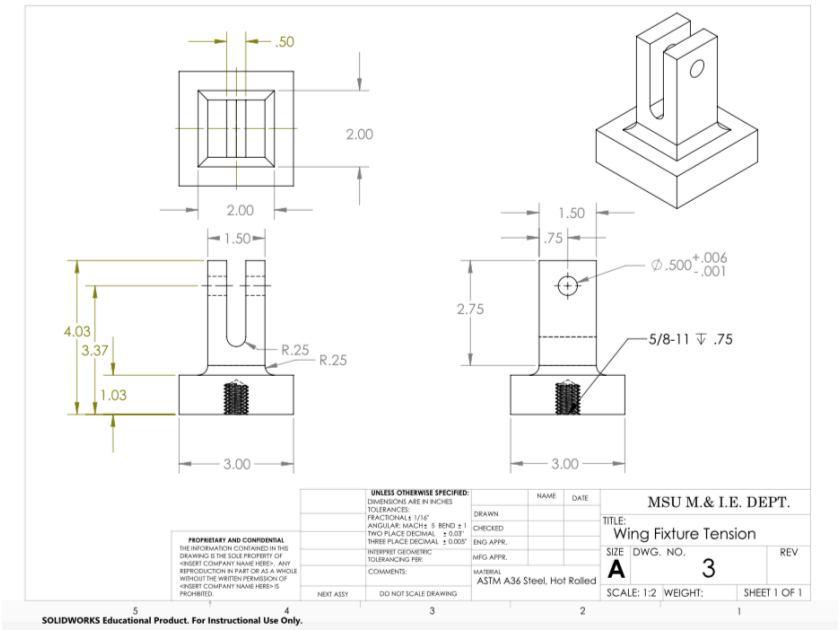
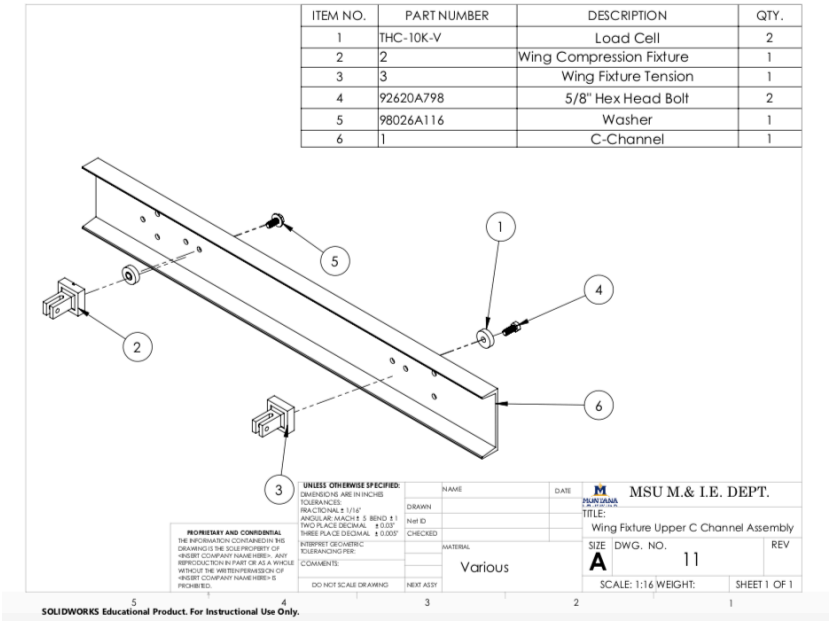


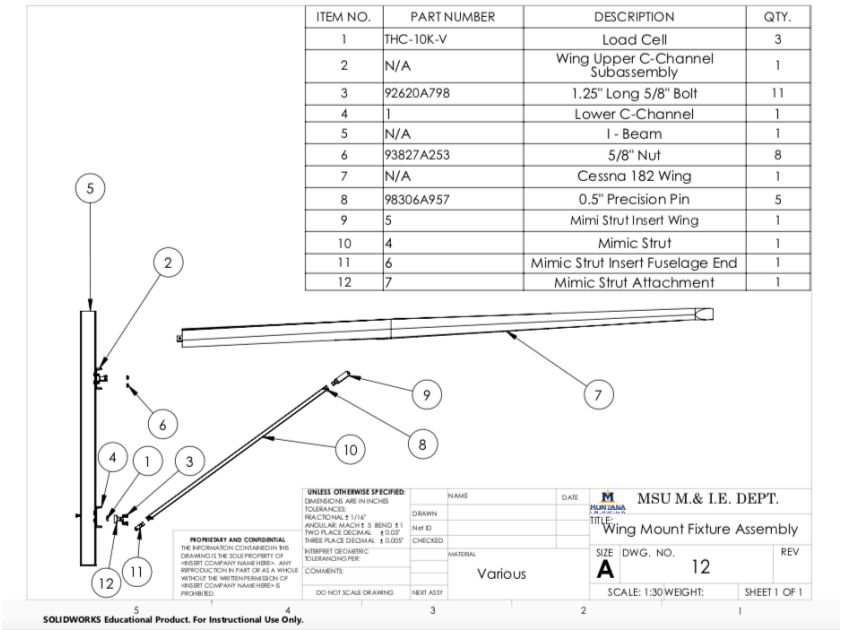

Figure 54. Engineering drawing of wing to c-channel attachment at leading edge for wing testing fixture from Capstone Technical Addendum [17].



| ITEM NO. | PART NUMBER | DESCRIPTION | QTY. |
|---|---|---|---|
| 1 | THC-10K-V | Load Cell | 2 |
| 2 | 2 | Wing Compression Fixture | 1 |
| 3 | 3 | Wing Fixture Tension | 1 |
| 4 | 92620A798 | 5/8" Hex Head Bolt | 2 |
| 5 | 98026A116 | Washer | 1 |
| 6 | 1 | C-Channel | 1 |



Figure 55. Engineering drawing of upper c-channel assembly for wing testing fixture from Capstone Technical Addendum [17].



| ITEM NO. | PART NUMBER | DESCRIPTION | QTY. |
|---|---|---|---|
| 1 | THC-10K-V | Load Cell | 3 |
| 2 | N/A | Wing Upper C-Channel Subassembly | 1 |
| 3 | 92620A798 | 1.25" Long 5/8" Bolt | 11 |
| 4 | 1 | Lower C-Channel | 1 |
| 5 | N/A | I - Beam | 1 |
| 6 | 93827A253 | 5/8" Nut | 8 |
| 7 | N/A | Cessna 182 Wing | 1 |
| 8 | 98306A957 | 0.5" Precision Pin | 5 |
| 9 | 5 | Mimi Strut Insert Wing | 1 |
| 10 | 4 | Mimic Strut | 1 |
| 11 | 6 | Mimic Strut Insert Fuselage End | 1 |
| 12 | 7 | Mimic Strut Attachment | 1 |



Figure 56. Engineering drawing of full wing mount fixture assembly from Capstone Technical Addendum [17].

# APPENDIX C

## STRUT TESTING CRASH SEQUENCES AND PLOTS

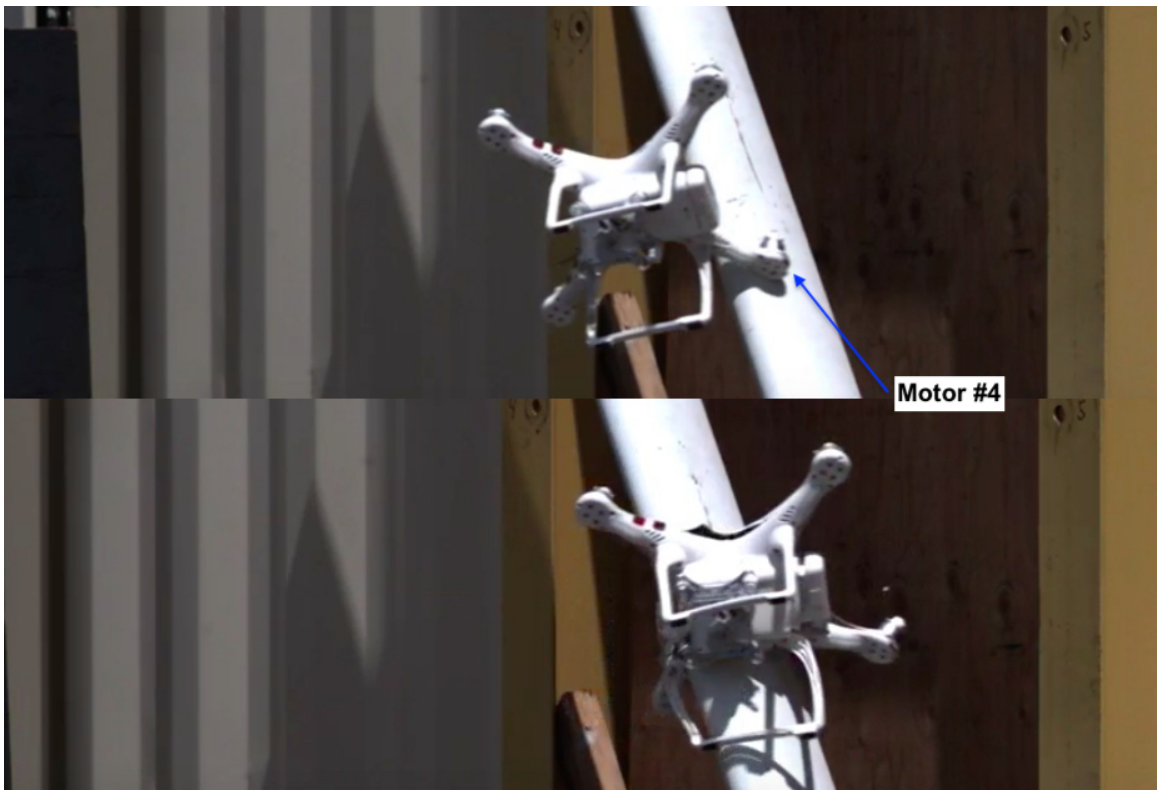



Figure 57. Impact orientation crash sequence of UAV # 1 in test A16-GA_0001.

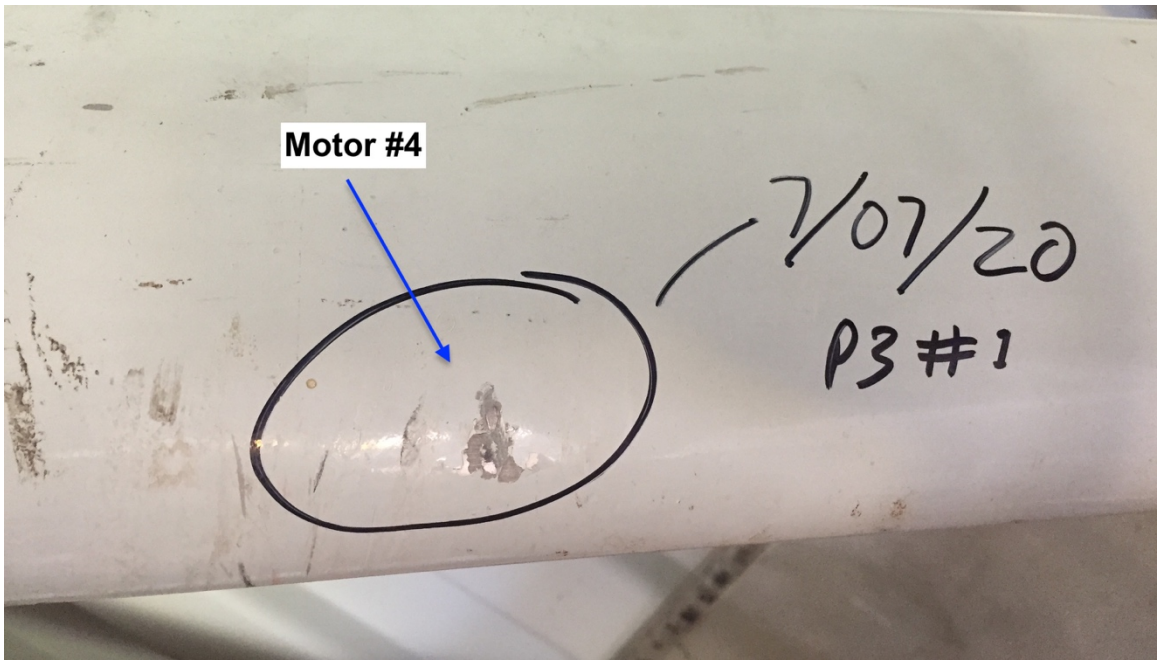



Figure 58. Damage from test A16-GA_0001.

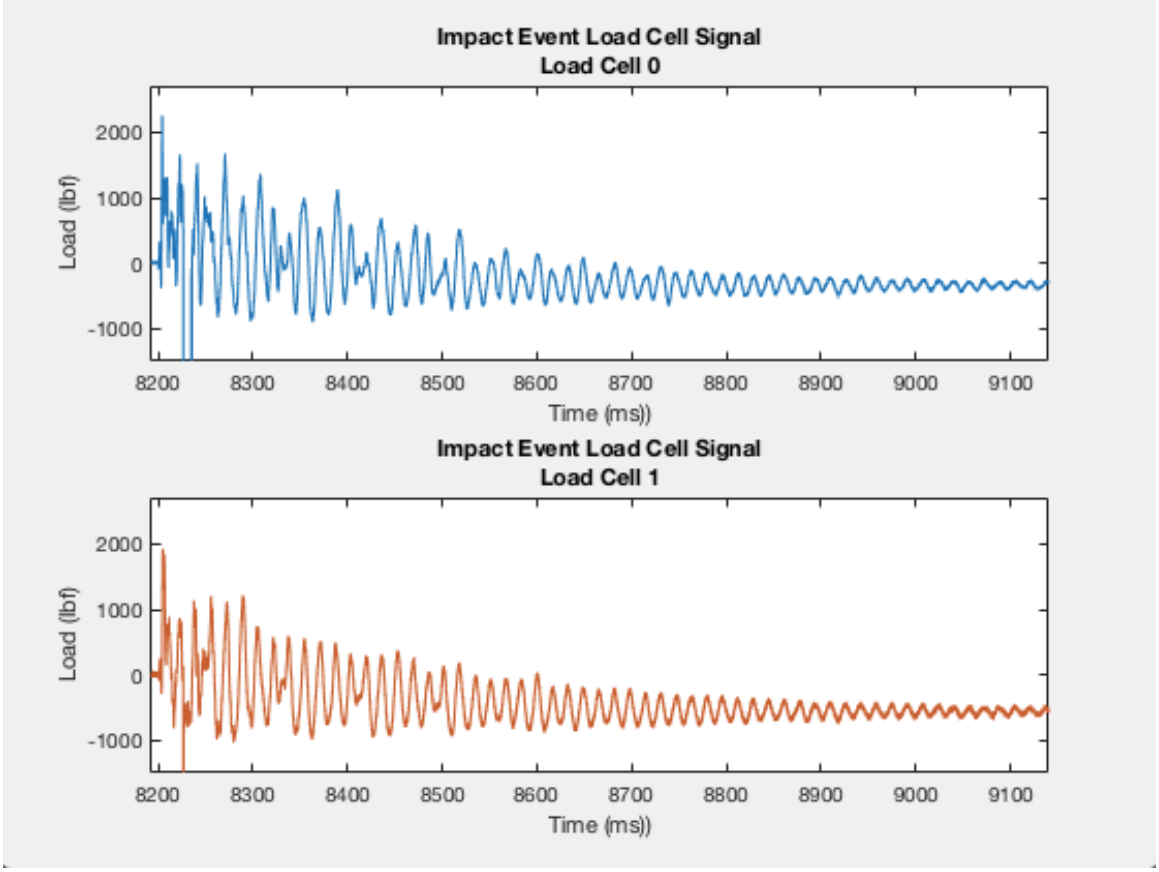



Figure 59. Load cell output from Matlab for test A16-GA_0001.

# APPENDIX D

## WING TESTING CRASH SEQUENCES AND PLOTS




Figure 60. Impact orientation and crash sequence of UAV # 6 in test A16-GA_0004.

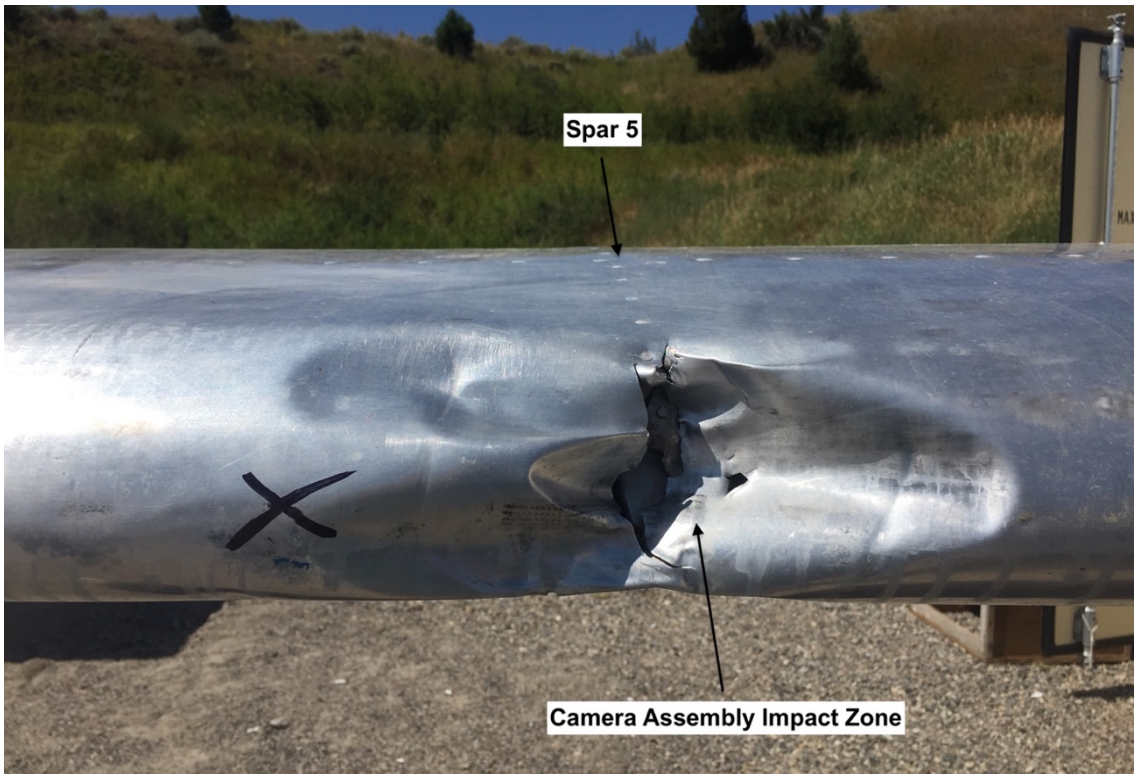



Figure 61. Damage from test A16-GA_0004.

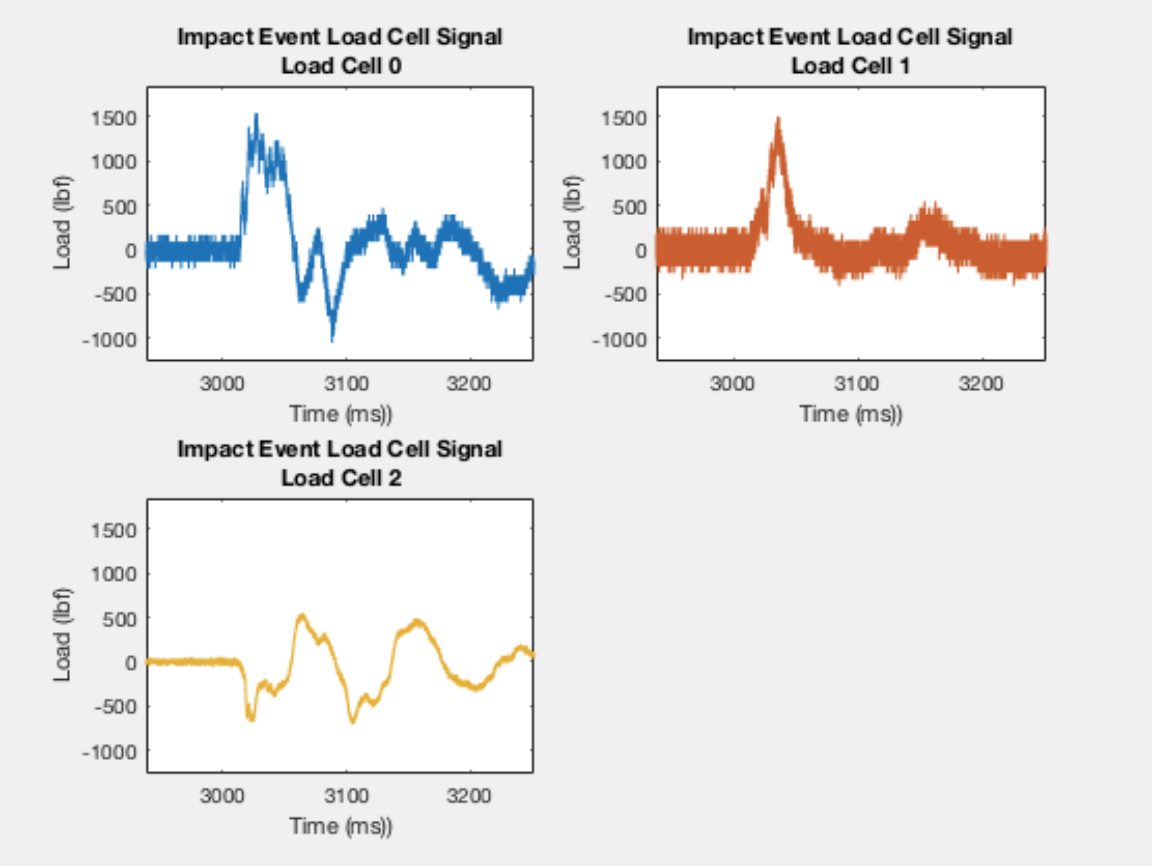



Figure 62. Load cell output from Matlab for test A16-GA_0004.

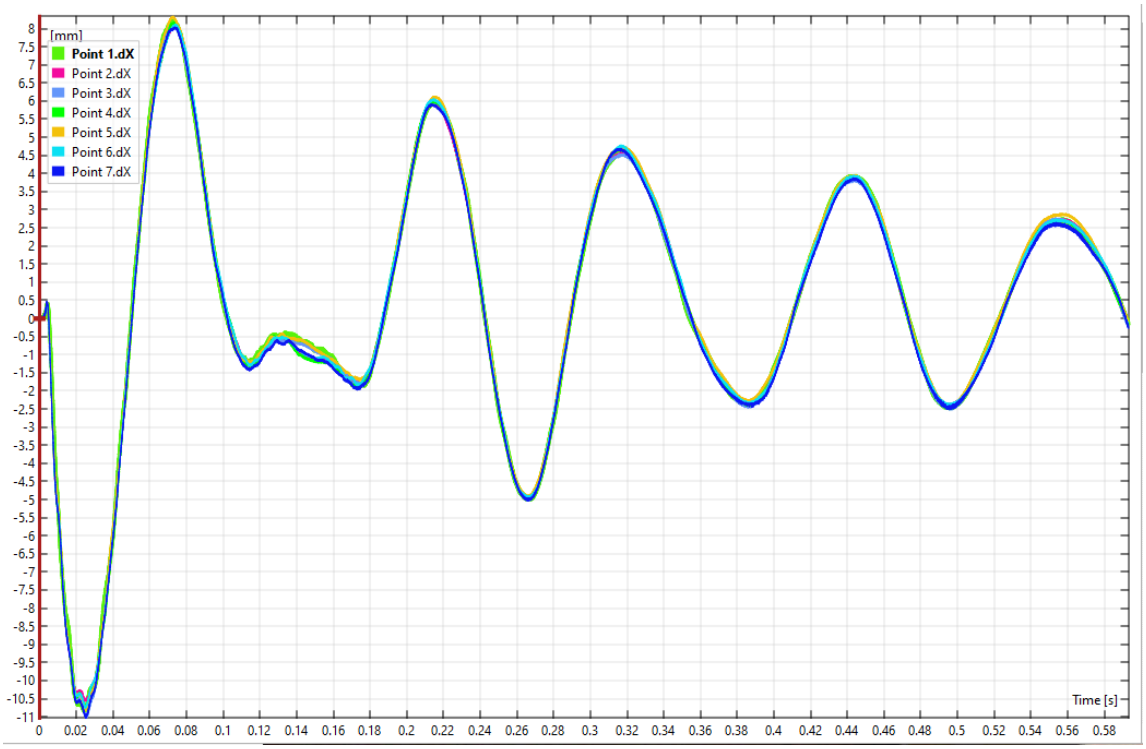



Figure 63. 2-D displacement tracking in x-direction for test A16-GA_0004.

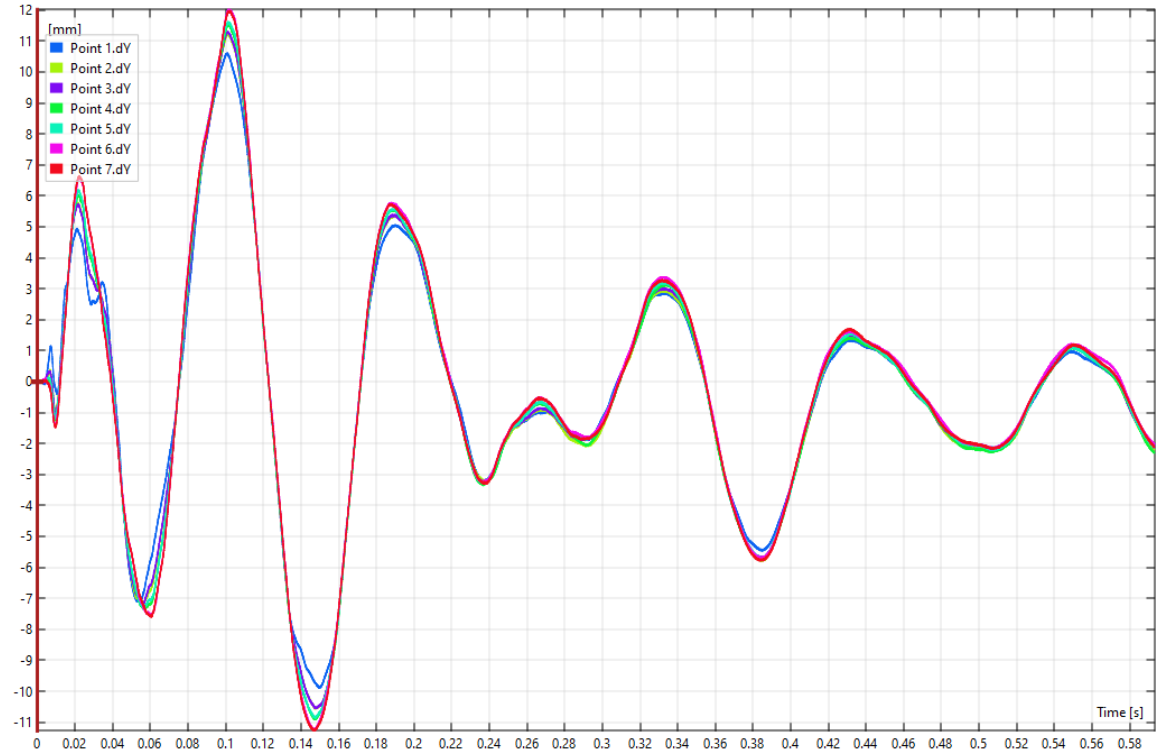



Figure 64. 2-D displacement tracking in y-direction for test A16-GA_0004.

# APPENDIX E

## WINDSCREEN TESTING CRASH SEQUENCES AND PLOTS

A16-GA_0005

Table 17. Results from test A16-GA_0005.

| | | | | | | | | |
|---|---|---|---|---|---|---|---|---|
| A16-GA_0005 | UAV # | | Mass (g) | | Velocity (kts) | | Target | |
| | 11 | | 1175.4 | | 110 | | Center | |
| | Damage: Failure and penetration of windscreen | | | | | | | |
| | Remarks: Drone arm clipped plate | | | | | | | |
| | LC 0 (lbf) | LC 1 (lbf) | LC 2 (lbf) | LC 3 (lbf) | LC 4 (lbf) | LC 5 (lbf) | LC 6 (lbf) | LC 7 (lbf) |
| | 910 ± 91 | 968 ± 108 | 869 ± 93 | 767 ± 94 | 299 ± 88 | 139 ± 88 | 540 ± 81 | 823 ± 92 |
| | DIC Peak Location | | Deformation in x (mm) | | Deformation in y (mm) | | Deformation in z (mm) | |
| | Point 4 | | +0.424 ± 0.015 | | +0.940 ± 0.033 | | +4.134 ± 0.069 | |

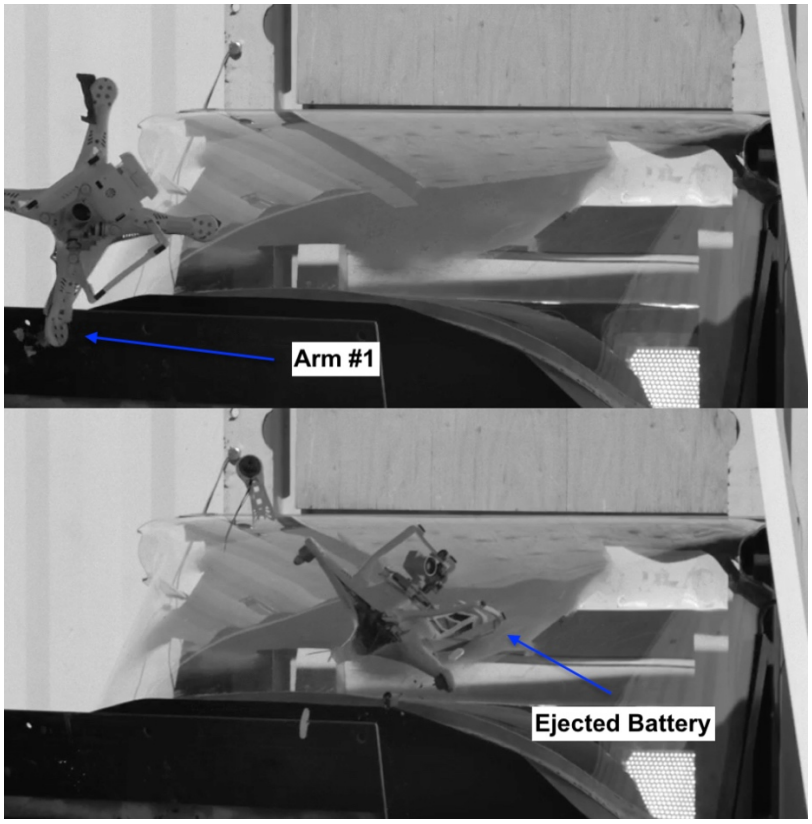



Figure 65. Clipping and impact orientation of UAV #11 in test A-16-GA_0005.



Figure 66. Damage from test A16-GA_0005.

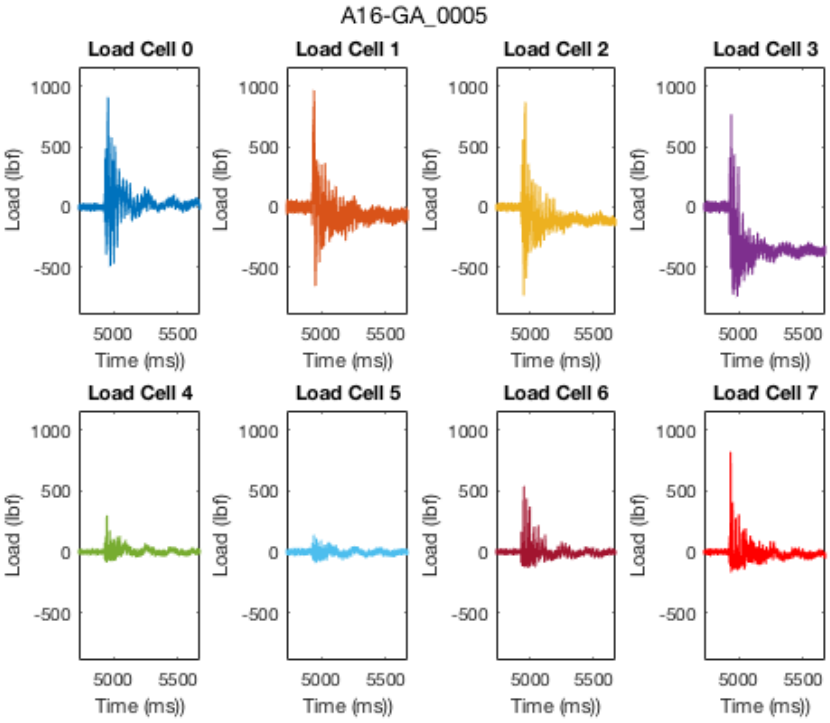



Figure 67. Load cell output from Matlab for test A-16-GA_0005.

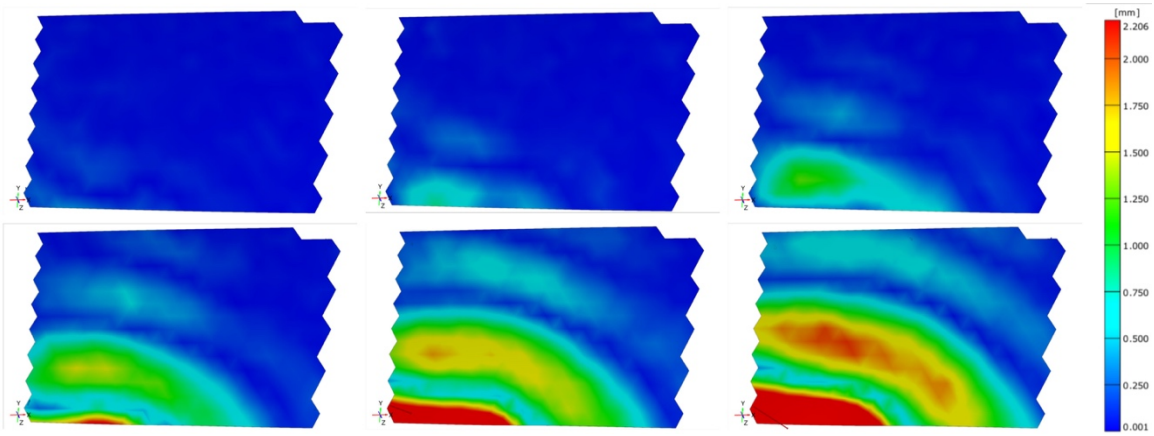



Figure 68. Deformation series of surface component in test A16-GA_0005.

A16-GA_0006

Table 18. Results from test A16-GA_0006.

| | | | | | | | | |
|---|---|---|---|---|---|---|---|---|
| A16-GA_0006 | UAV # | | Mass (g) | | Velocity (kts) | | Target | |
| | 20 | | 1168.3 | | 110 | | Center | |
| | Damage: Failure and penetration of windscreen | | | | | | | |
| | Remarks: Drone arm clipped plate | | | | | | | |
| | LC 0 (lbf) | LC 1 (lbf) | LC 2 (lbf) | LC 3 (lbf) | LC 4 (lbf) | LC 5 (lbf) | LC 6 (lbf) | LC 7 (lbf) |
| | 1499 ± 97 | 751 ± 111 | 945 ± 97 | 496 ± 99 | 198 ± 94 | 138 ± 94 | 209 ± 98 | 85 ± 85 |
| | DIC Peak Location | | Deformation in x (mm) | | Deformation in y (mm) | | Deformation in z (mm) | |
| | Point 17 | | -2.343 ± 0.014 | | +1.988 ± 0.030 | | +14.093 ± 0.076 | |

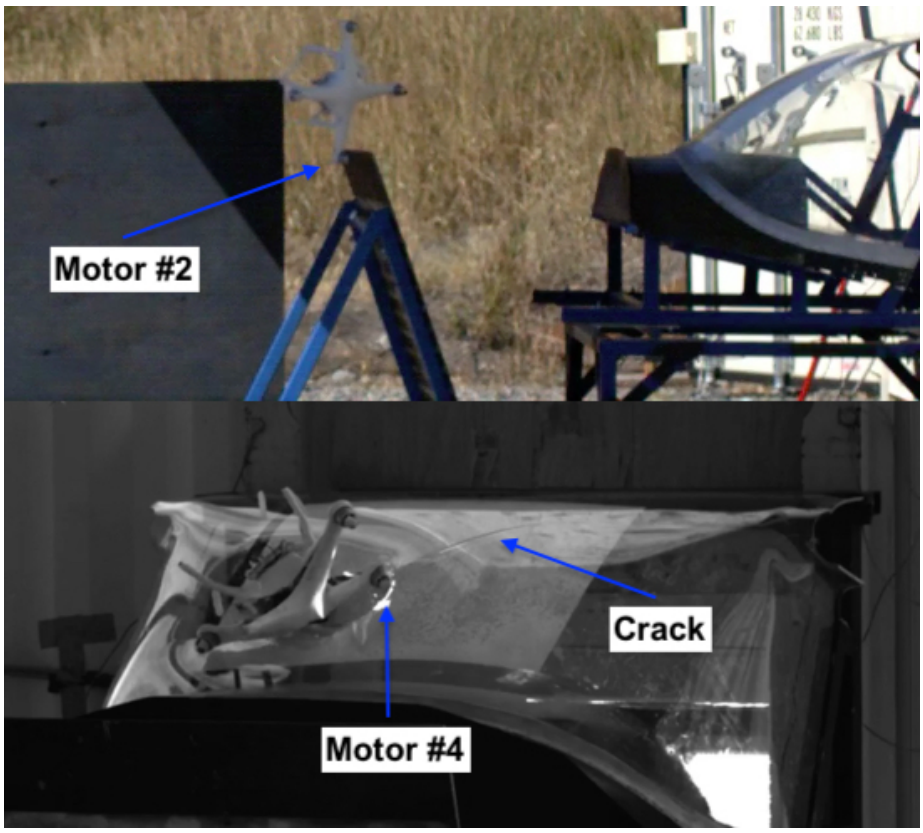



Figure 69. Clipping and impact orientation of UAV #20 in test A-16-GA_0006.

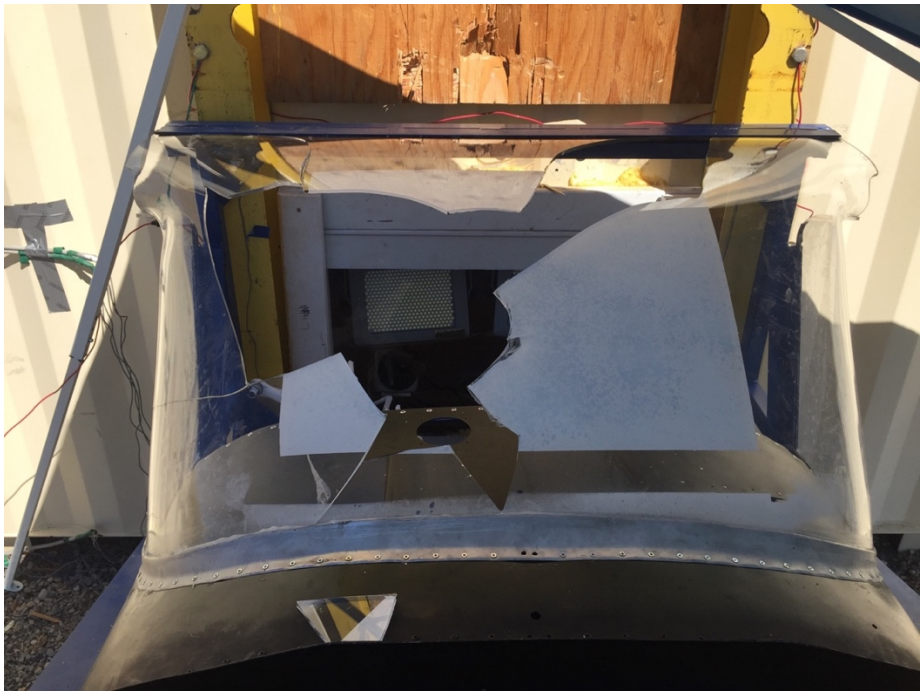


Figure 70. Damage from test A16-GA_0006.

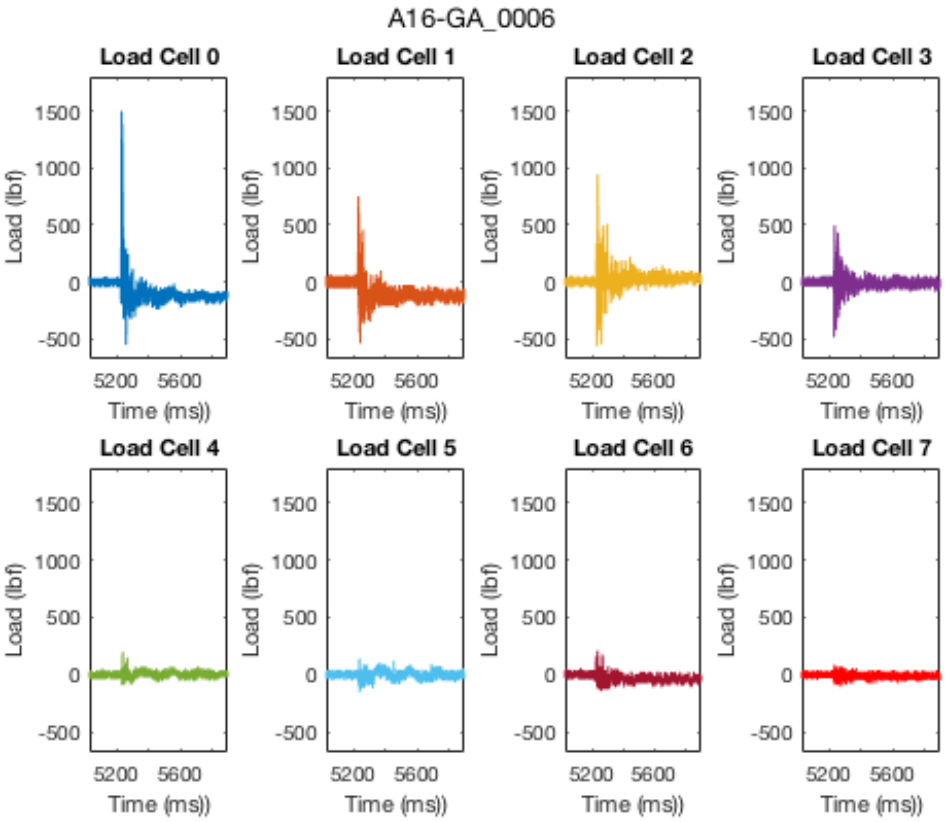



Figure 71. Load cell output from Matlab for test A16-GA_0006.

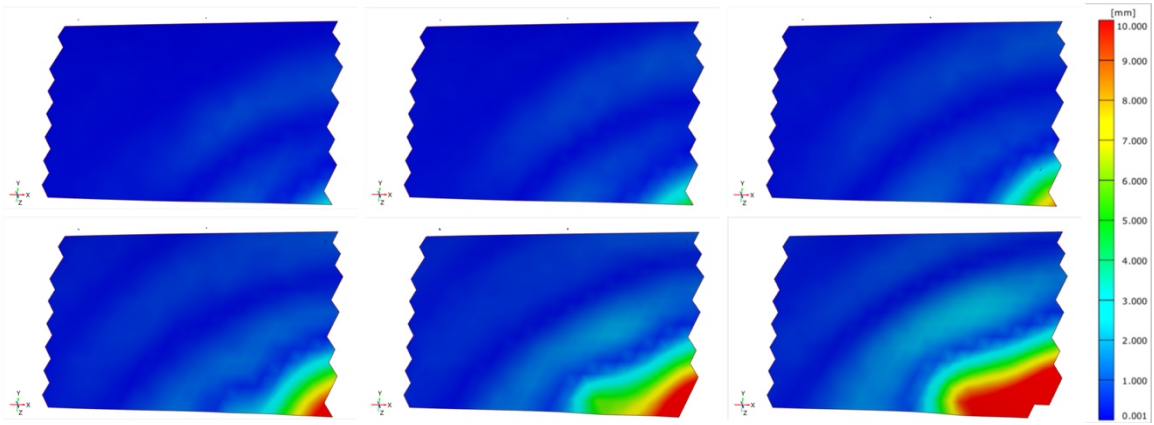



Figure 72. Deformation series of surface component in test A16-GA_0006.

A16-GA_0007

Table 19. Results from test A16-GA_0007.

| | | | | | | | | |
|---|---|---|---|---|---|---|---|---|
| A16-GA_0007 | UAV # | | Mass (g) | | Velocity (kts) | | Target | |
| | 18 | | 362 (battery) | | 71 (battery) | | Center | |
| | Damage: Skid mark on lower windscreen, elastic deformation only | | | | | | | |
| | Remarks: Drone clipped plate upon entry, battery ejected and was the only substantial object to impact windscreen | | | | | | | |
| | LC 0 (lbf) | LC 1 (lbf) | LC 2 (lbf) | LC 3 (lbf) | LC 4 (lbf) | LC 5 (lbf) | LC 6 (lbf) | LC 7 (lbf) |
| | 489 ± 91 | 234 ± 107 | 896 ± 93 | 672 ± 93 | 172 ± 87 | 180 ± 88 | 484 ± 91 | 480 ± 80 |
| | DIC Peak Location | | Deformation in x (mm) | | Deformation in y (mm) | | Deformation in z (mm) | |
| | Point 17 | | -0.303 ± 0.014 | | +0.536 ± 0.025 | | +9.2 ± 0.055 | |

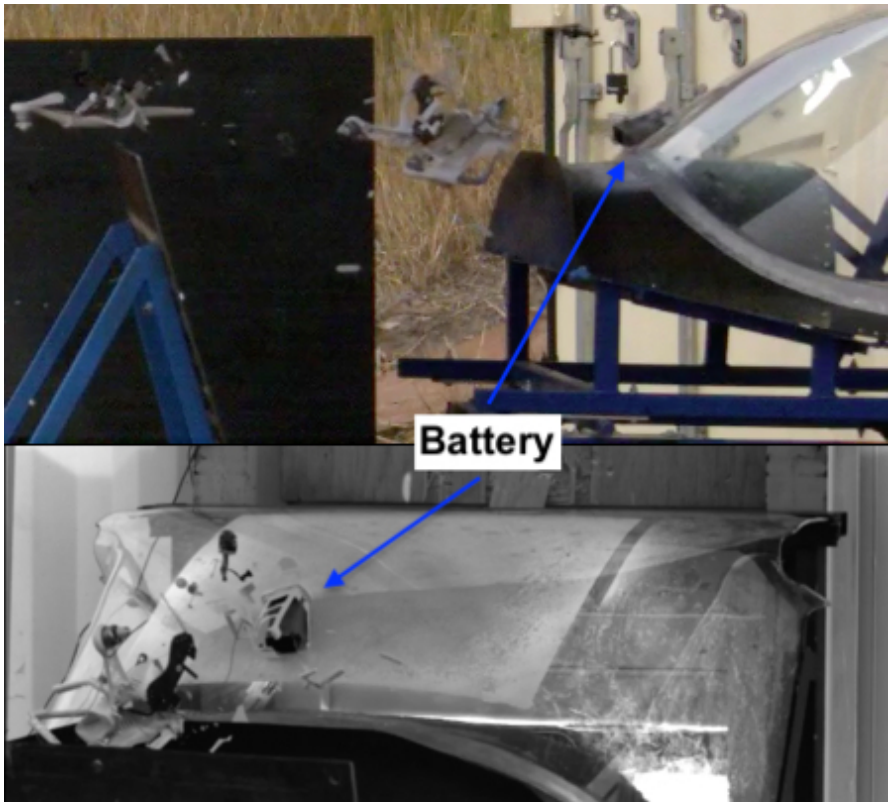



Figure 73. Stills from high speed footage of test A16-GA_0007.



Figure 74. Damage from battery in test A16-GA_0007.

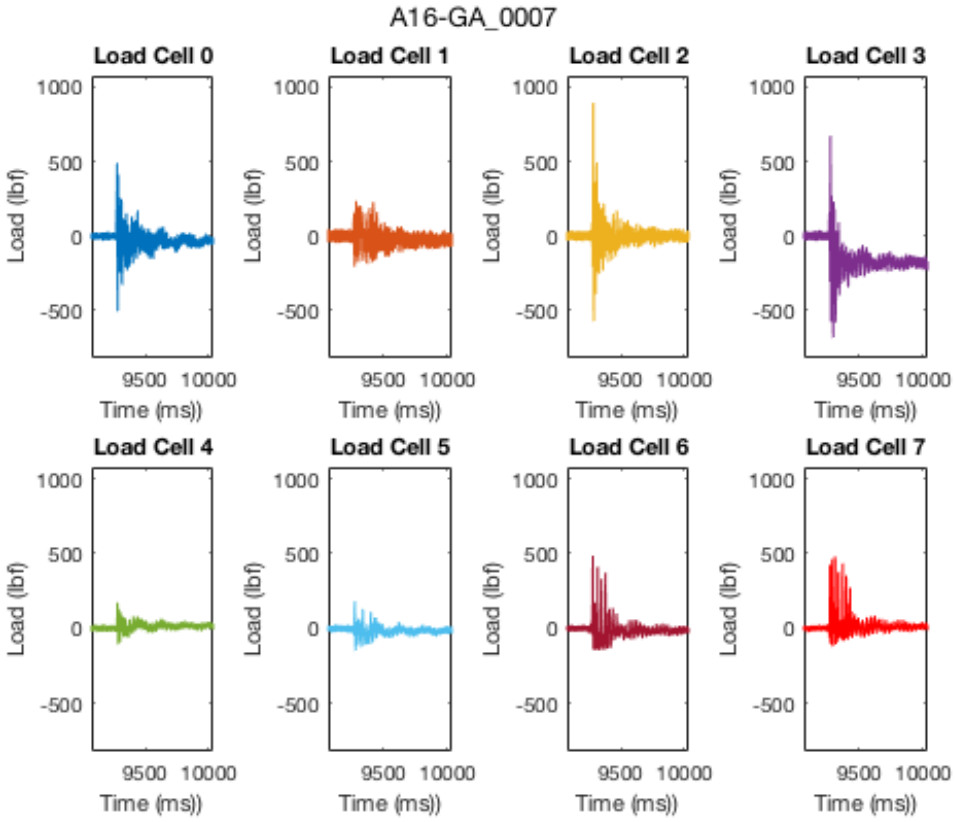



Figure 75. Load cell plots from Matlab for test A16-GA_0007.

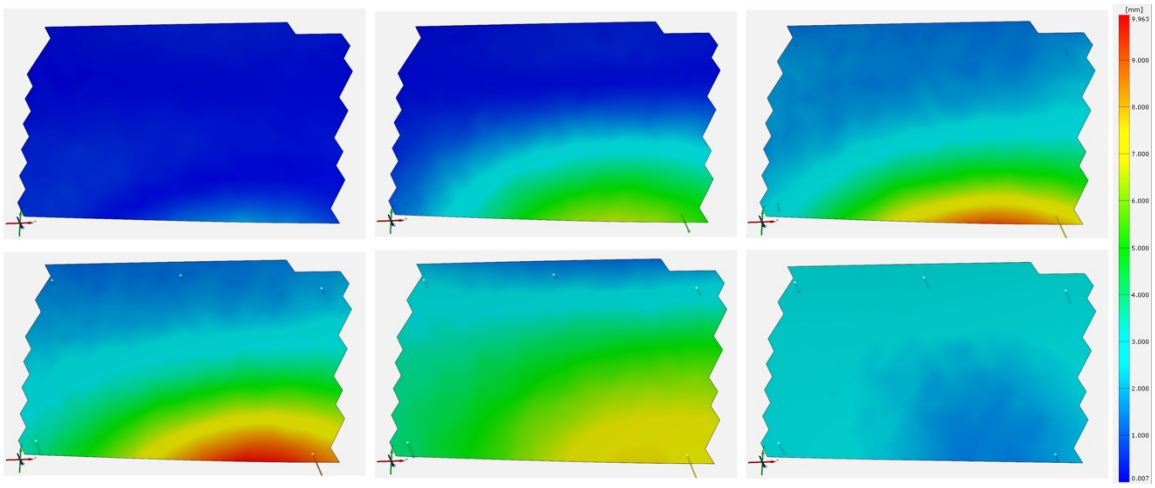


Figure 76. Deformation series of surface component in test A16-GA_0007.

A16-GA_0008

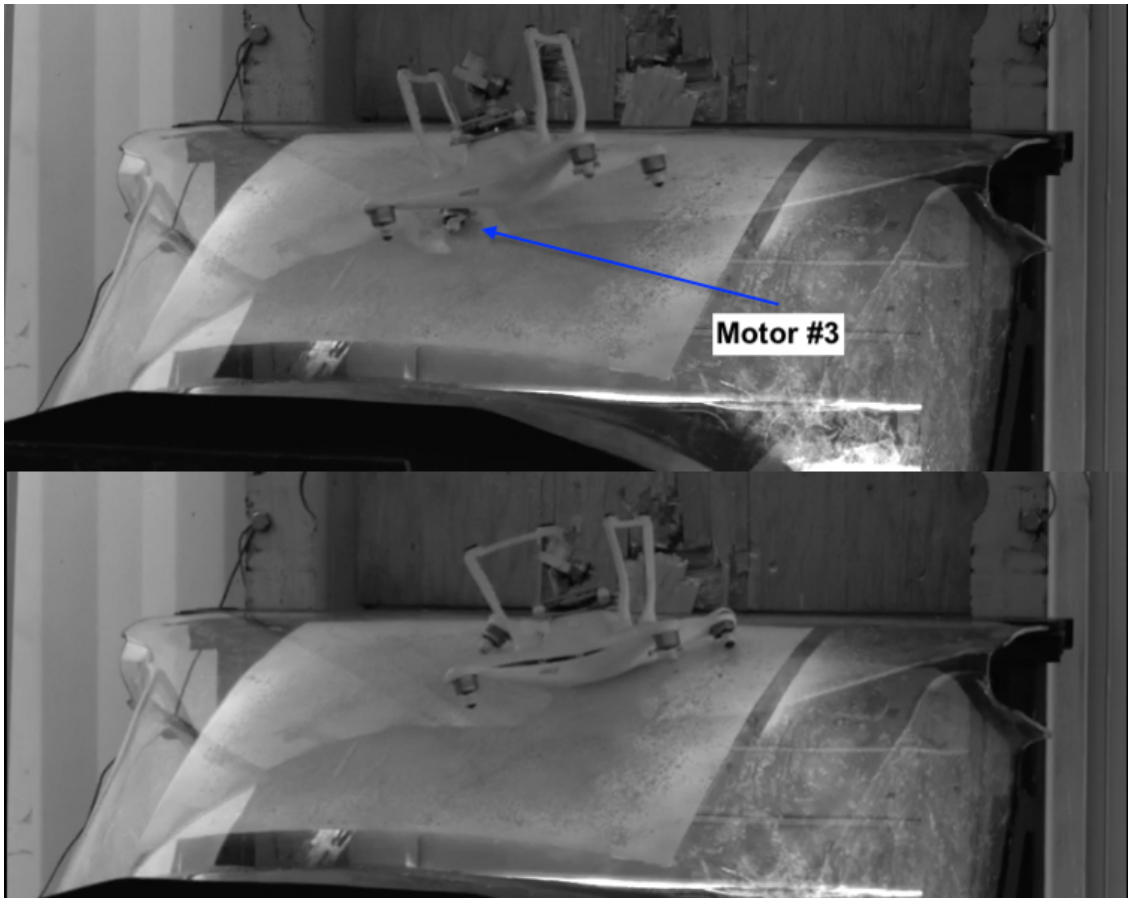



Figure 77. UAV #16 at beginning and middle of impact in test A16-GA_0008.

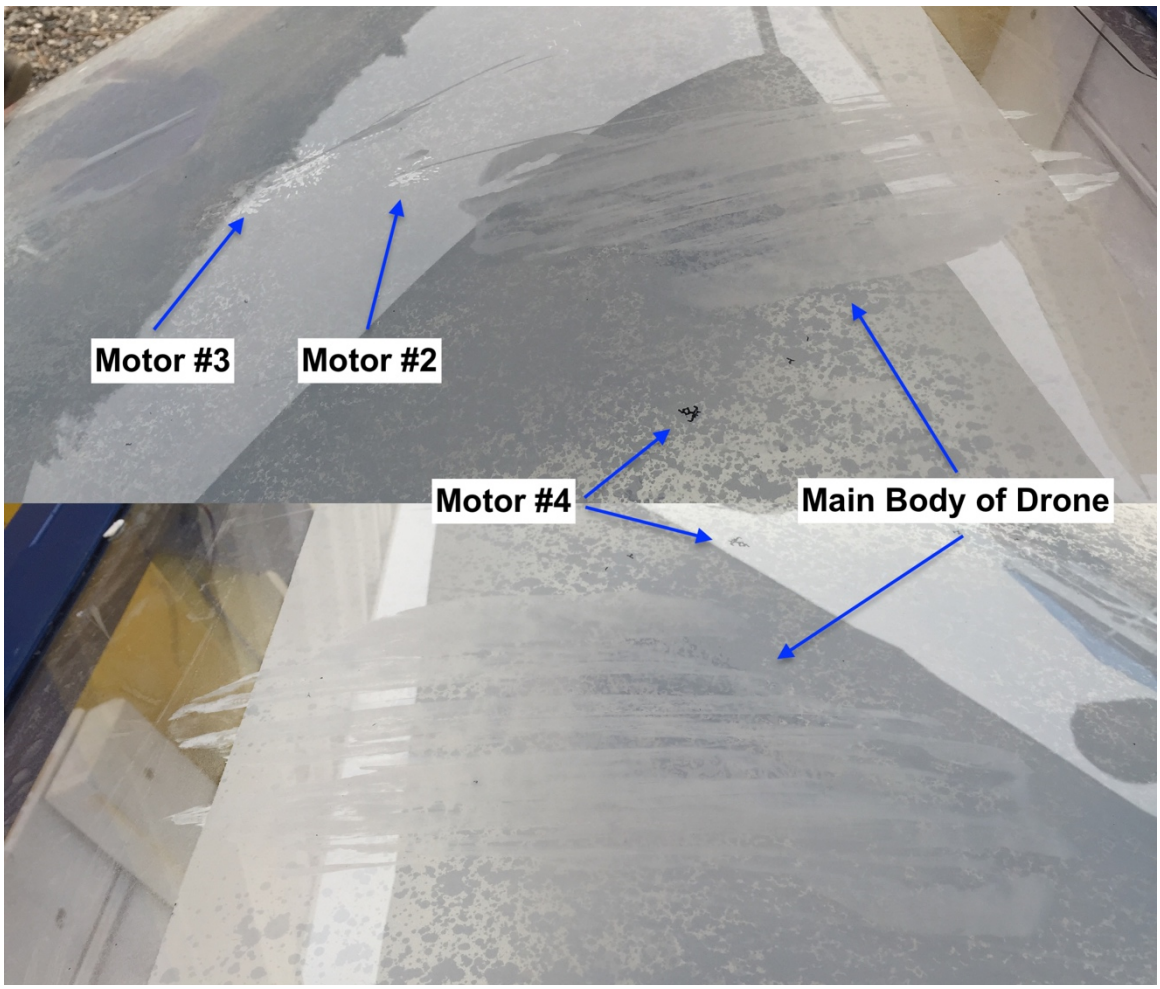



Figure 78. Damage from test A16-GA_0008.

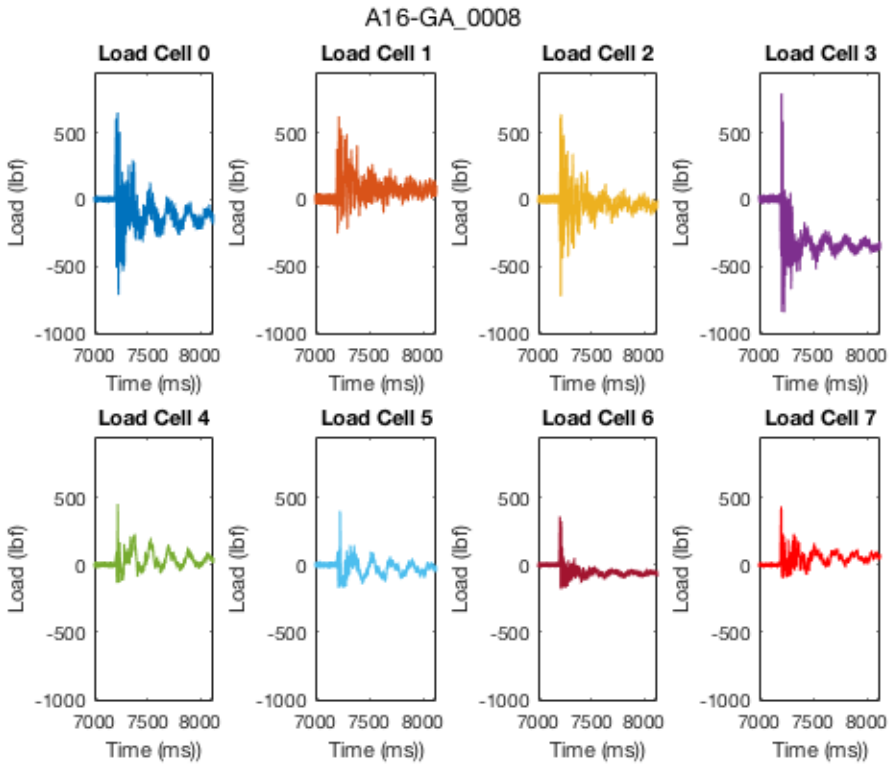



Figure 79. Load cell plots from Matlab for test A16-GA_0008.

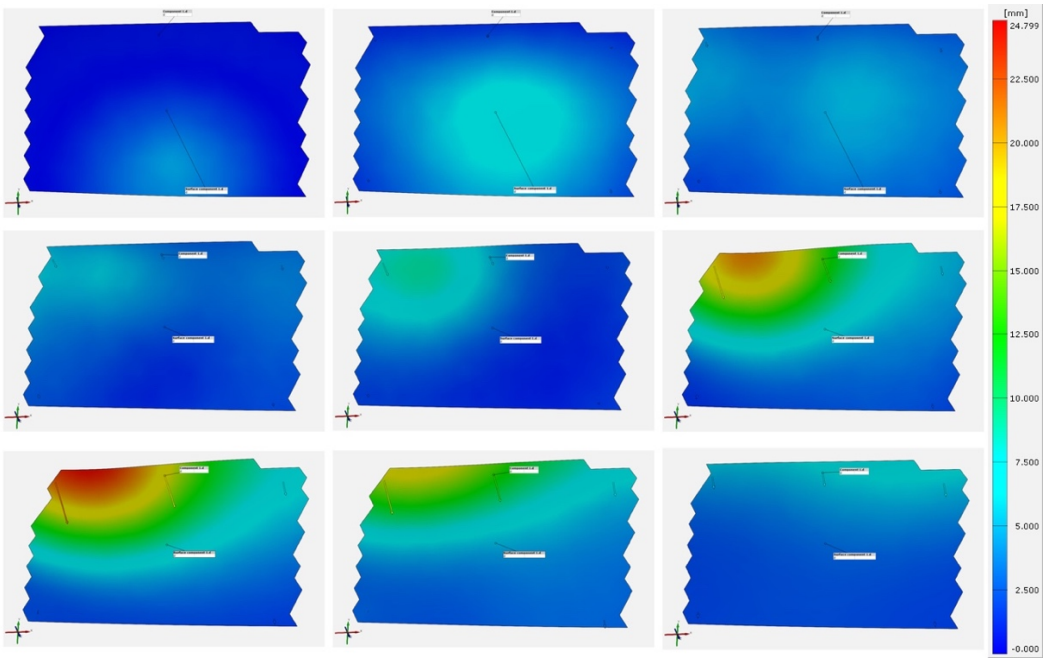



Figure 80. Deformation series for test A16-GA_0008. The top three images show deformation #1 from motor #3 and the other images depict deformation #2.

A16-GA_0009

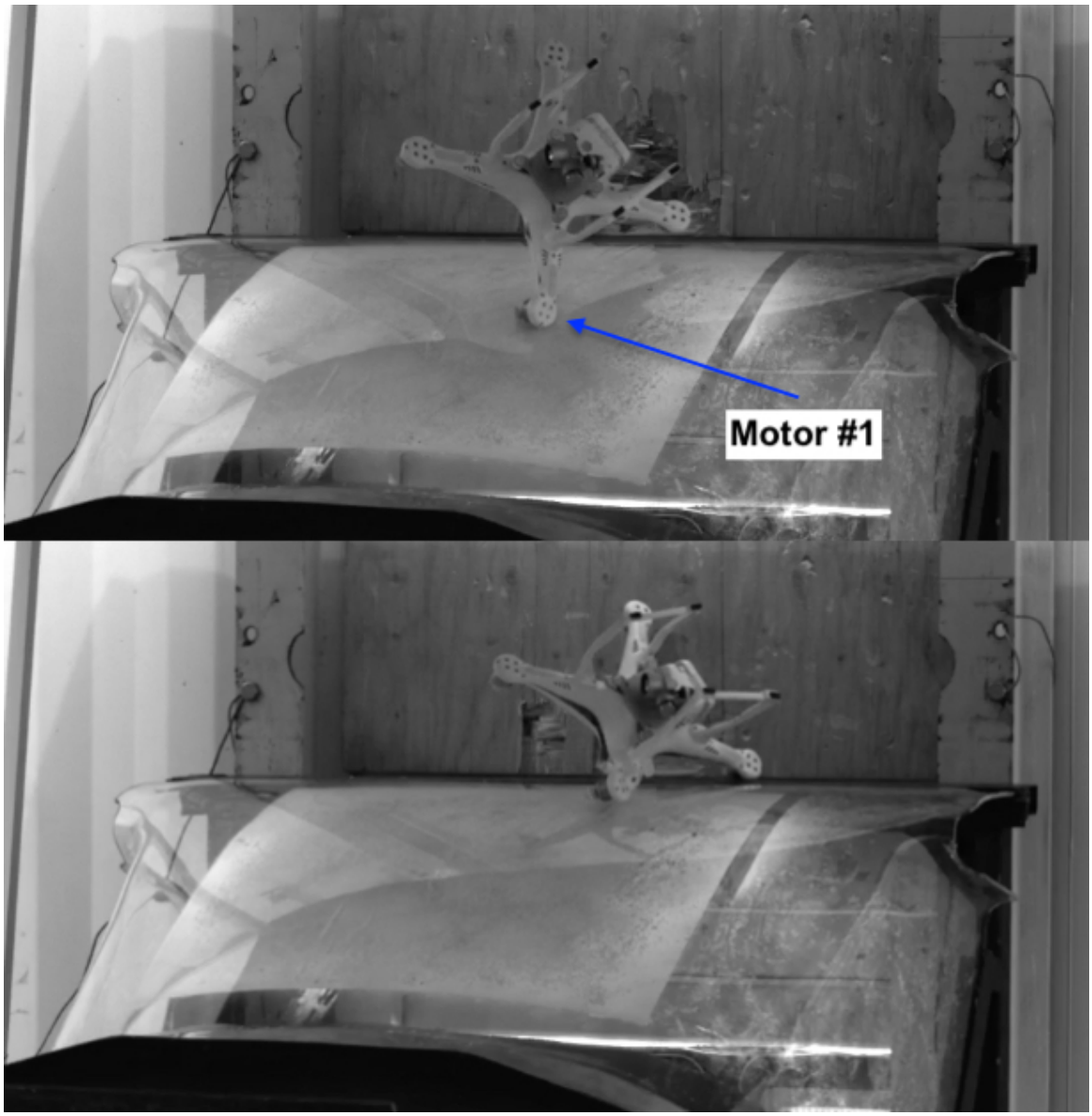



Figure 81. Impact orientation and crash sequence for test A16-GA_0009.

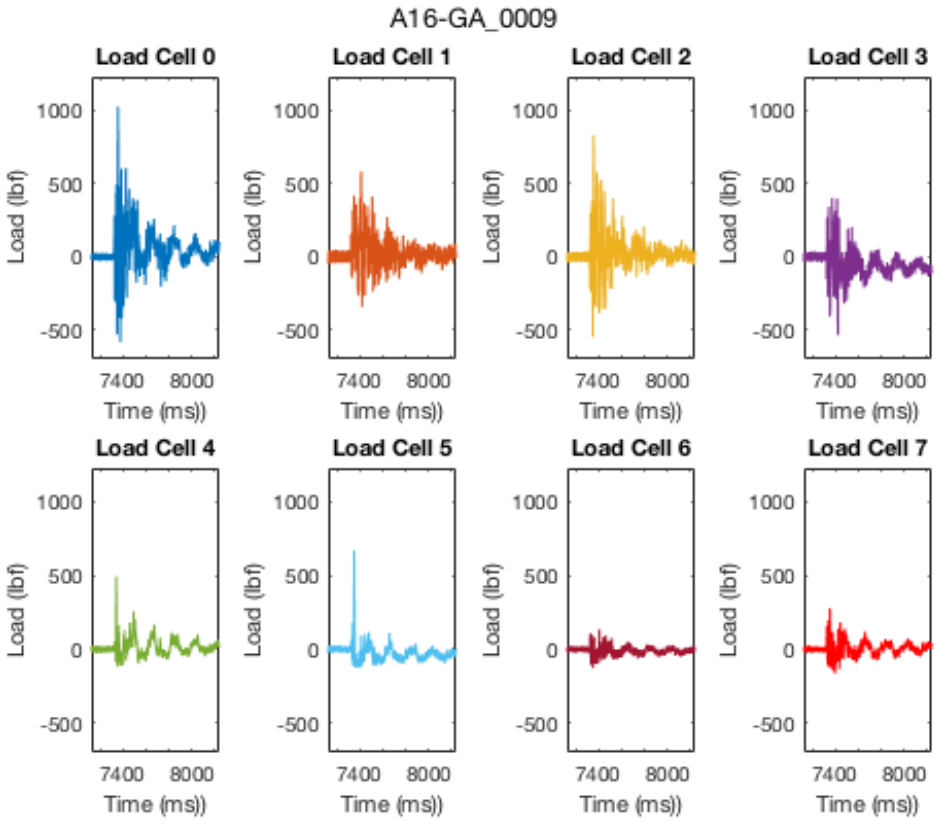



Figure 82. Load cell plots from Matlab for test A16-GA_0009.

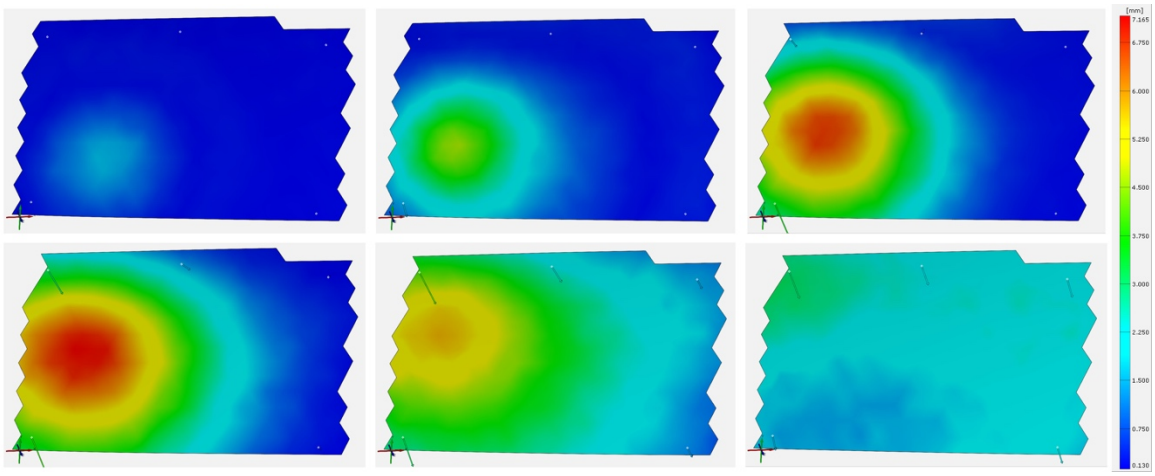


Figure 83. Deformation series of surface component in test A16-GA_0009.

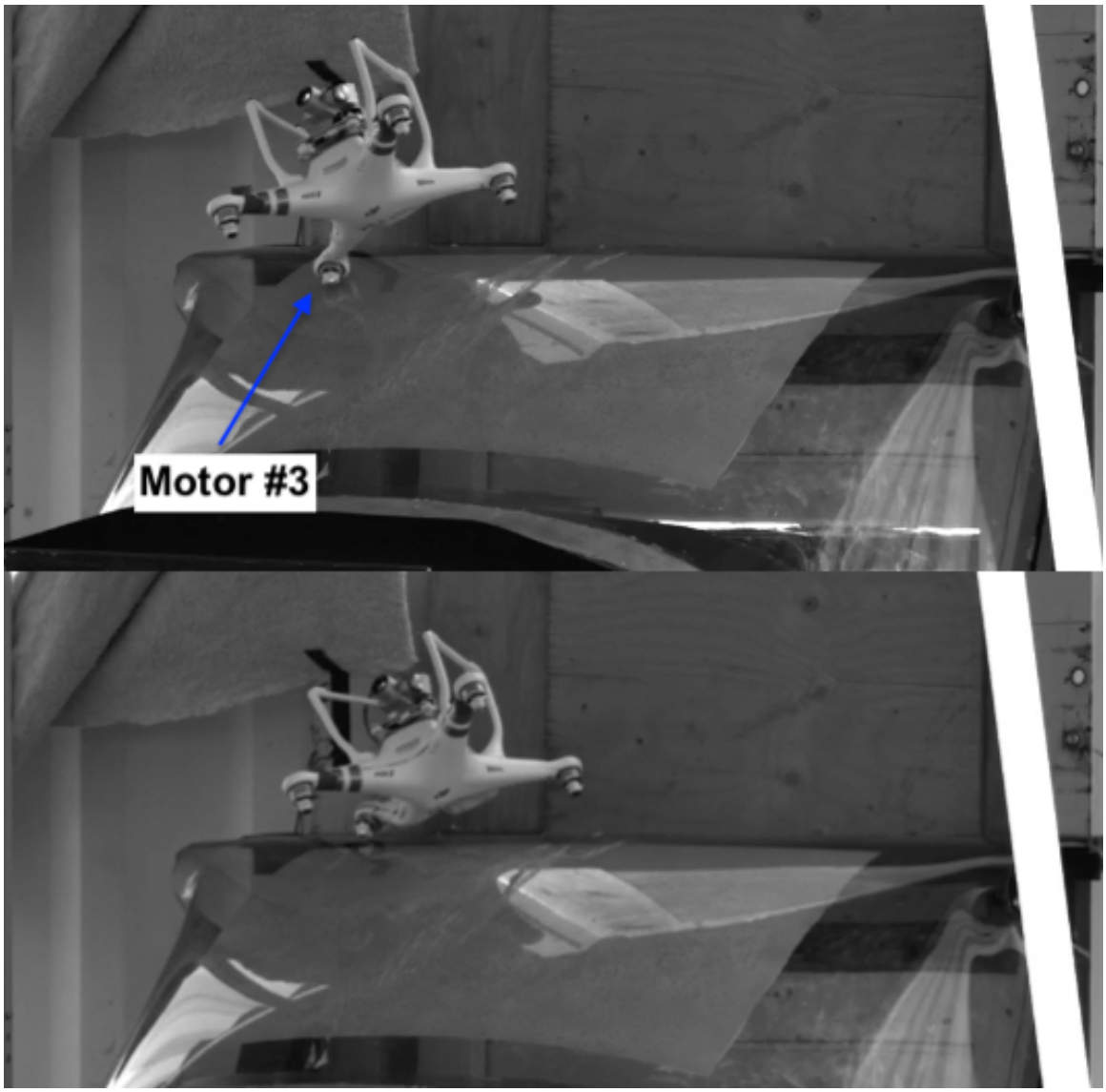



Figure 84. UAV impact orientation for test A16-GA_0011.

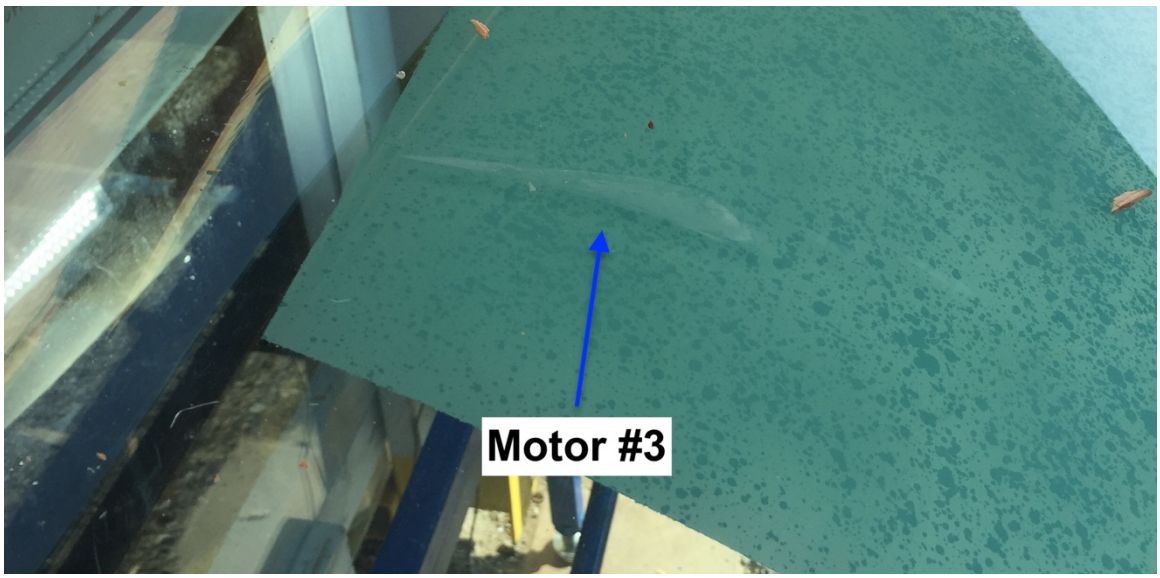



Figure 85. Damage from windscreen test A16-GA_0011.

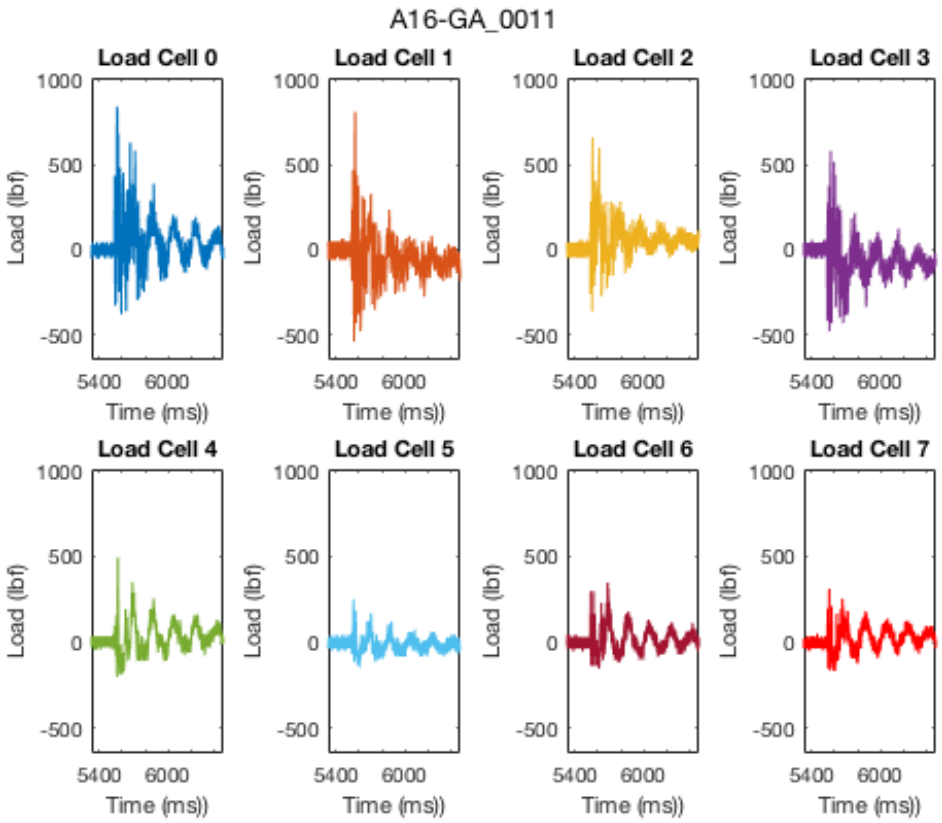



Figure 86. Load cell plots from Matlab for test A16-GA_0011.

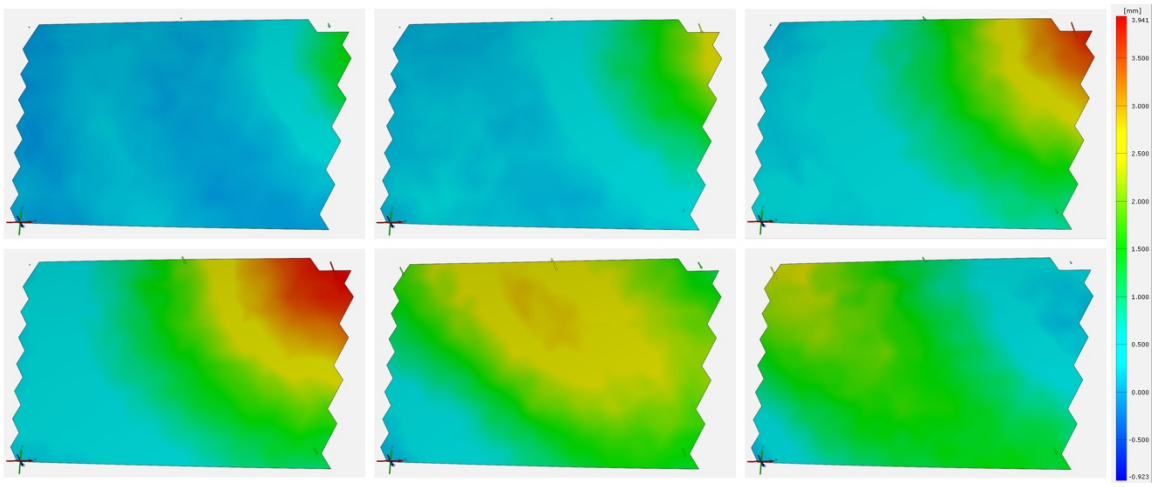


Figure 87. Deformation series of surface component in test A16-GA_0011.

A16-GA_0012

Table 20. Results from test A16-GA_0012.

| | | | | | | | | |
|---|---|---|---|---|---|---|---|---|
| A16-GA_0012 | UAV # | | Mass (g) | | Velocity (kts) | | Target | |
| | 17 | | 1176.6 | | 105 | | Center | |
| | Damage: Failure and penetration of windscreen | | | | | | | |
| | Remarks: Drone arm clipped plate / LC 0 connection cut | | | | | | | |
| | LC 0 (lbf) | LC 1 (lbf) | LC 2 (lbf) | LC 3 (lbf) | LC 4 (lbf) | LC 5 (lbf) | LC 6 (lbf) | LC 7 (lbf) |
| | 1539 ± 97 | 429 ± 111 | 660 ± 97 | 556 ± 99 | 248 ± 94 | 250 ± 94 | 271 ± 98 | 364 ± 85 |
| | DIC Peak Location | | Deformation in x (mm) | | Deformation in y (mm) | | Deformation in z (mm) | |
| | Point 17 | | -2.343 ± 0.013 | | +1.988 ± 0.032 | | +14.093 ± 0.061 | |

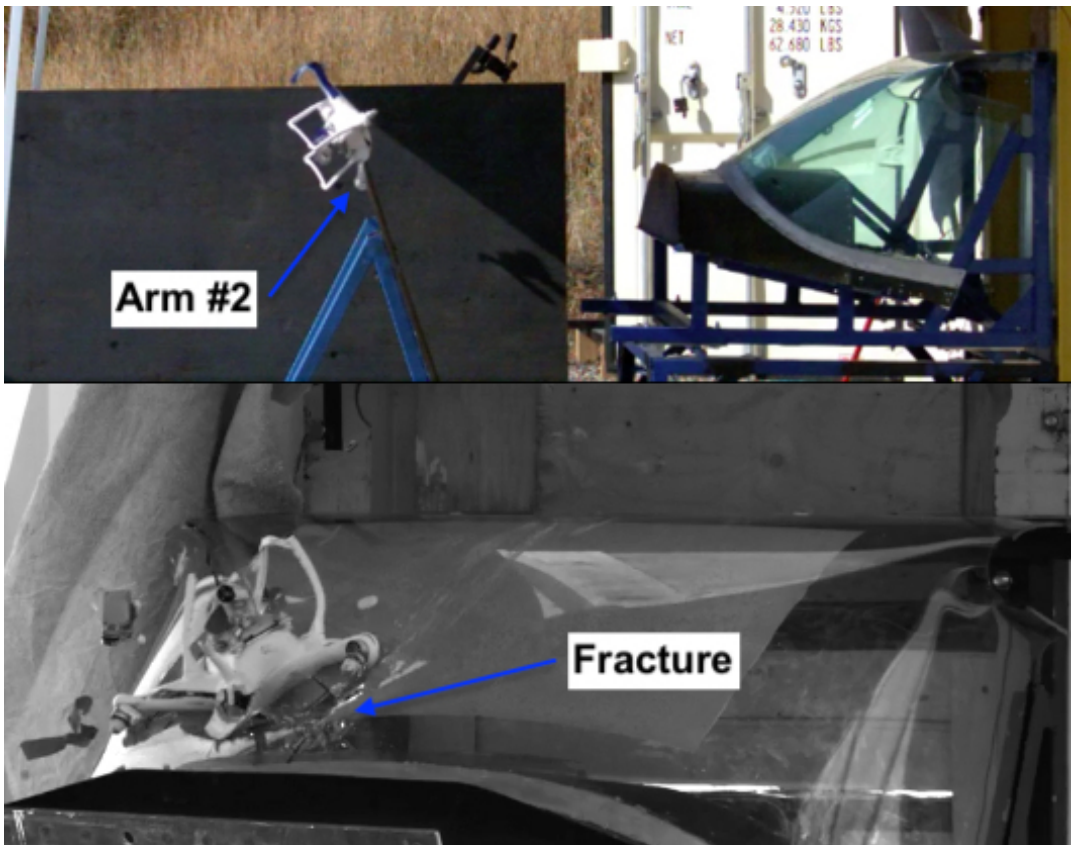



Figure 88. Crash sequence for test A16-GA_0012.



Figure 89. Damage from test A16-GA_0012.

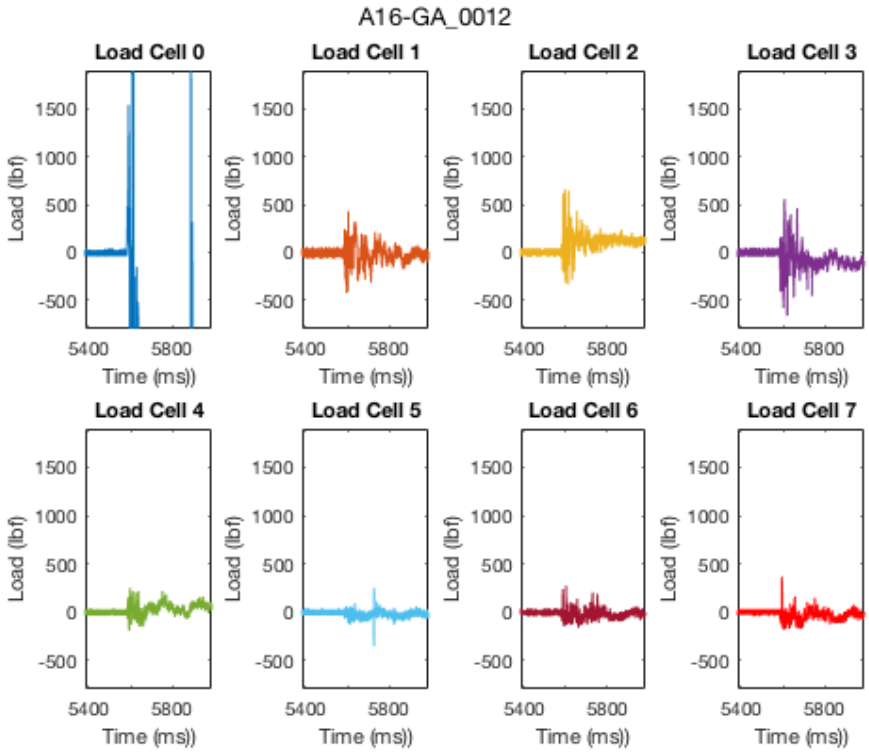



Figure 90. Load cell output from Matlab for test A16-GA_0012.

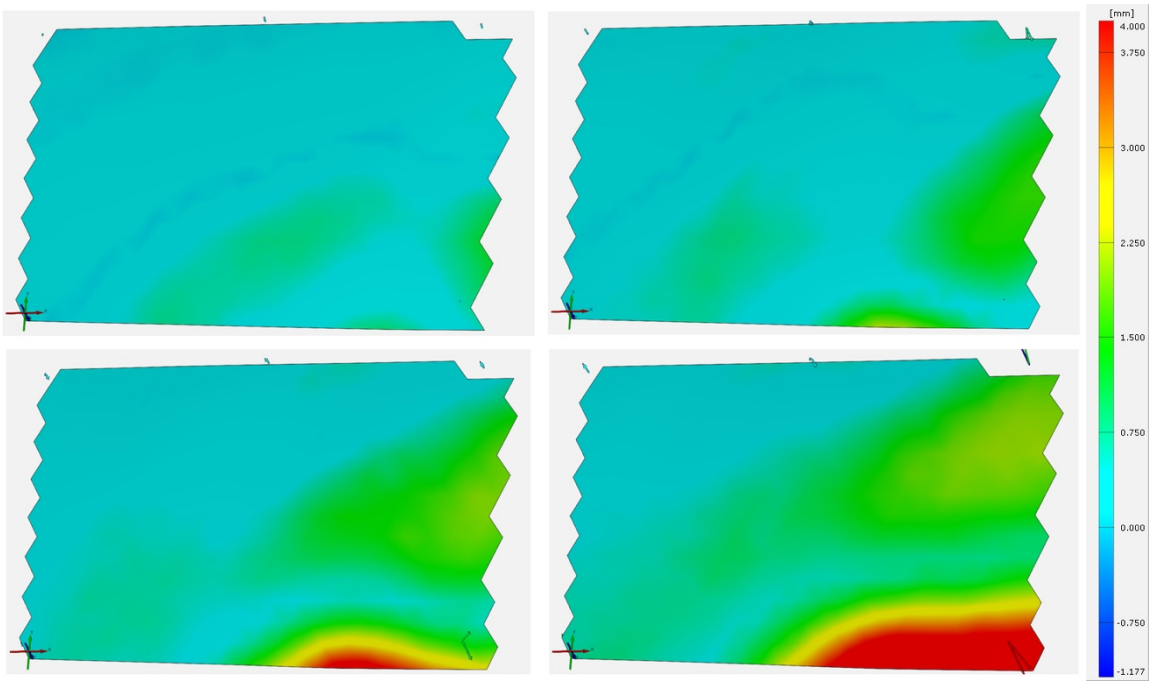



Figure 91. Deformation series of surface component in test A16-GA_0012 up until first visible fracture.

# APPENDIX F

## WINDSCREEN DIC DISPLACEMENT PLOTS

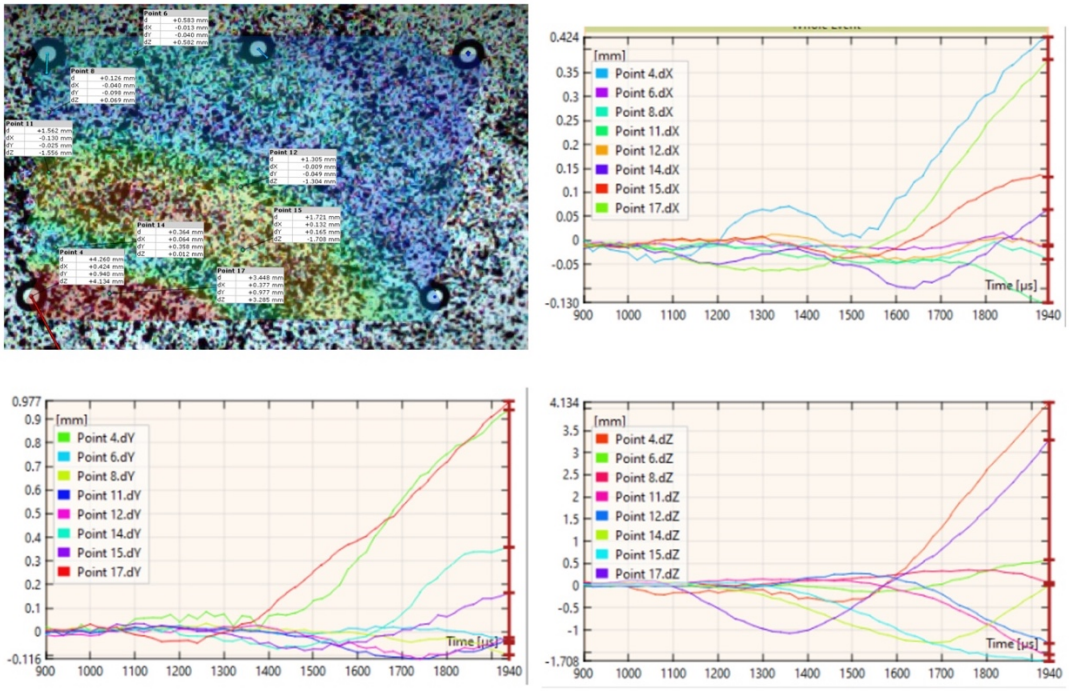



Figure 92. DIC point locations and displacement plots for test A16-GA_0005.

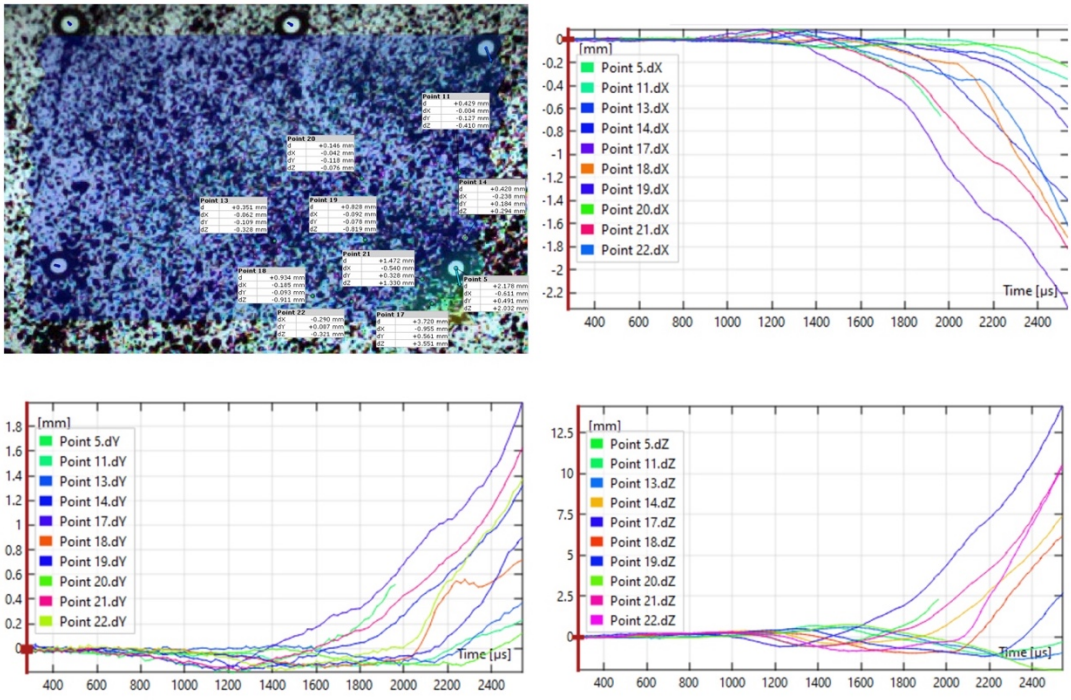



Figure 93. DIC point locations and displacement plots for test A16-GA_0006.

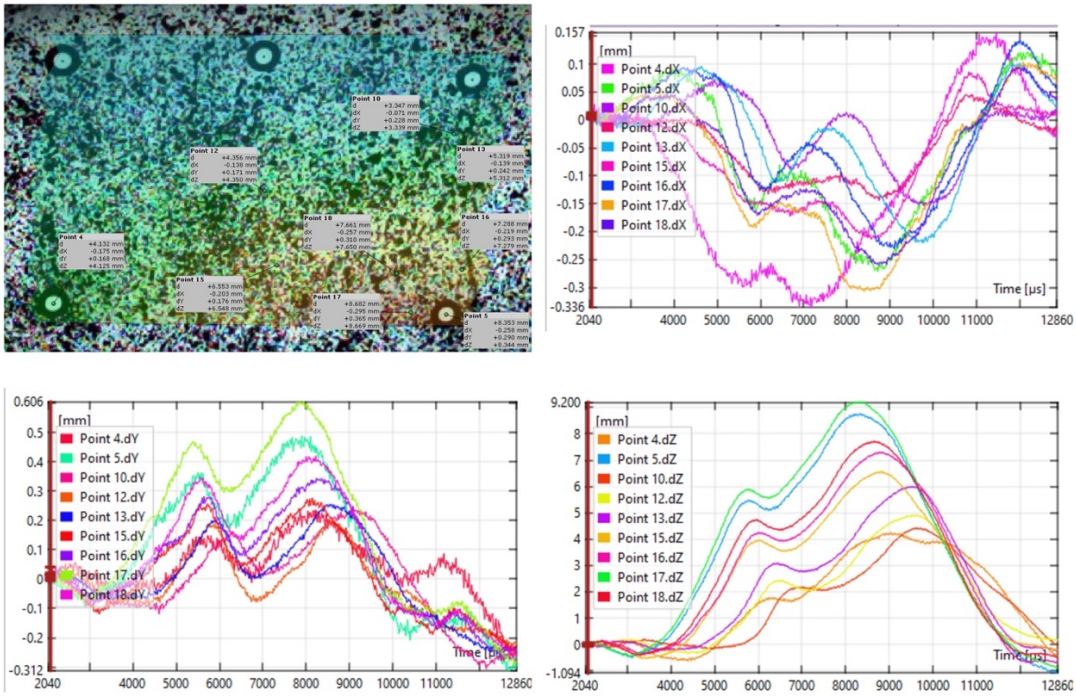



Figure 94. DIC point locations and displacement plots for test A16-GA_0007.

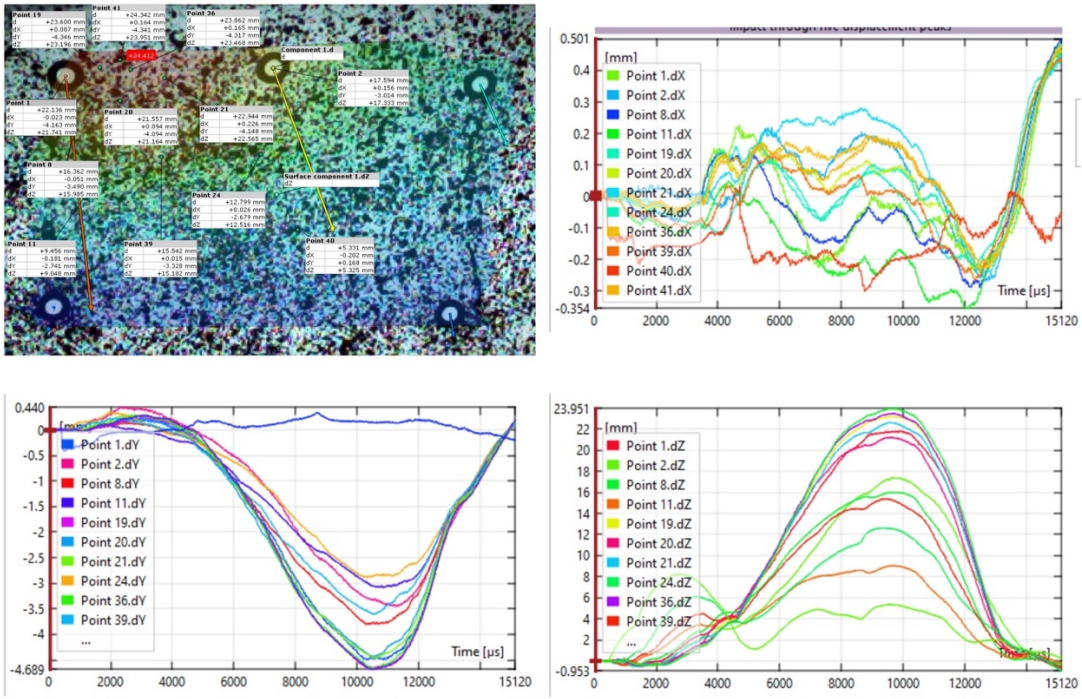



Figure 95. DIC point locations and displacement plots for test A16-GA_0008.

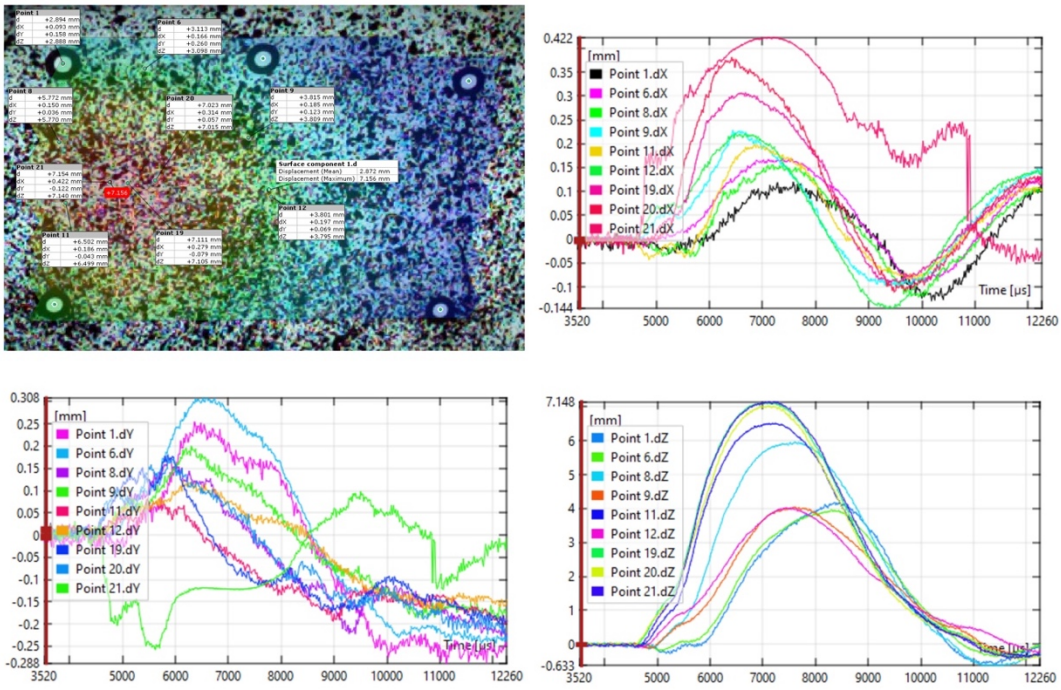



Figure 96. DIC point locations and displacement plots for test A16-GA_0009.

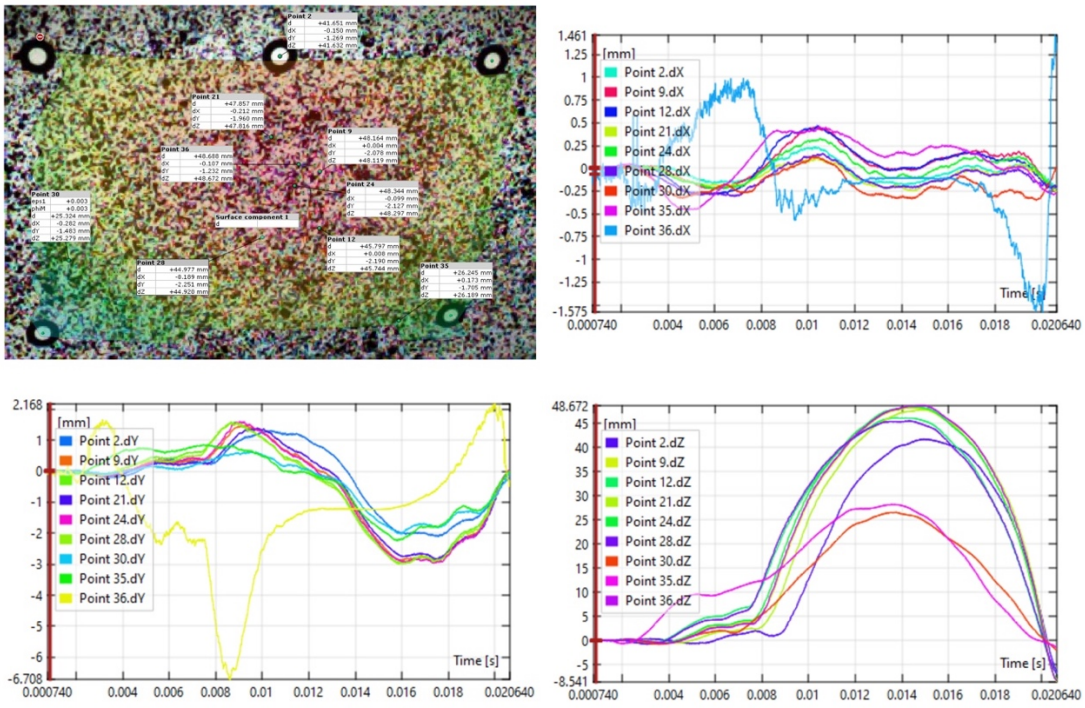



Figure 97. DIC point locations and displacement plots for test A16-GA_0010.

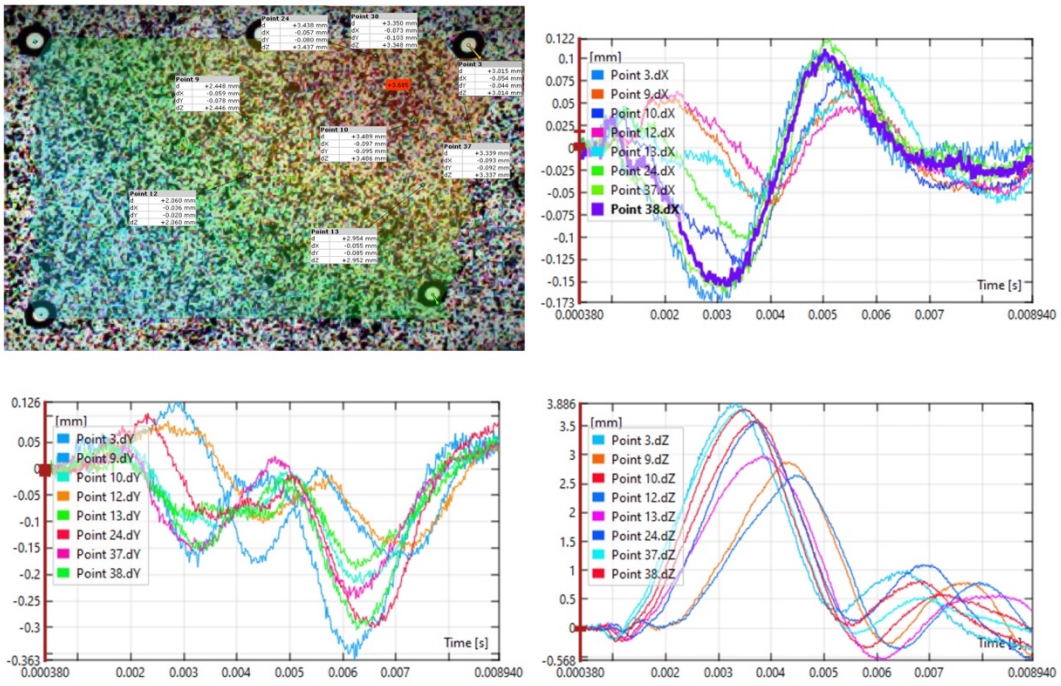



Figure 98. DIC point locations and displacement plots for test A16-GA_0011.

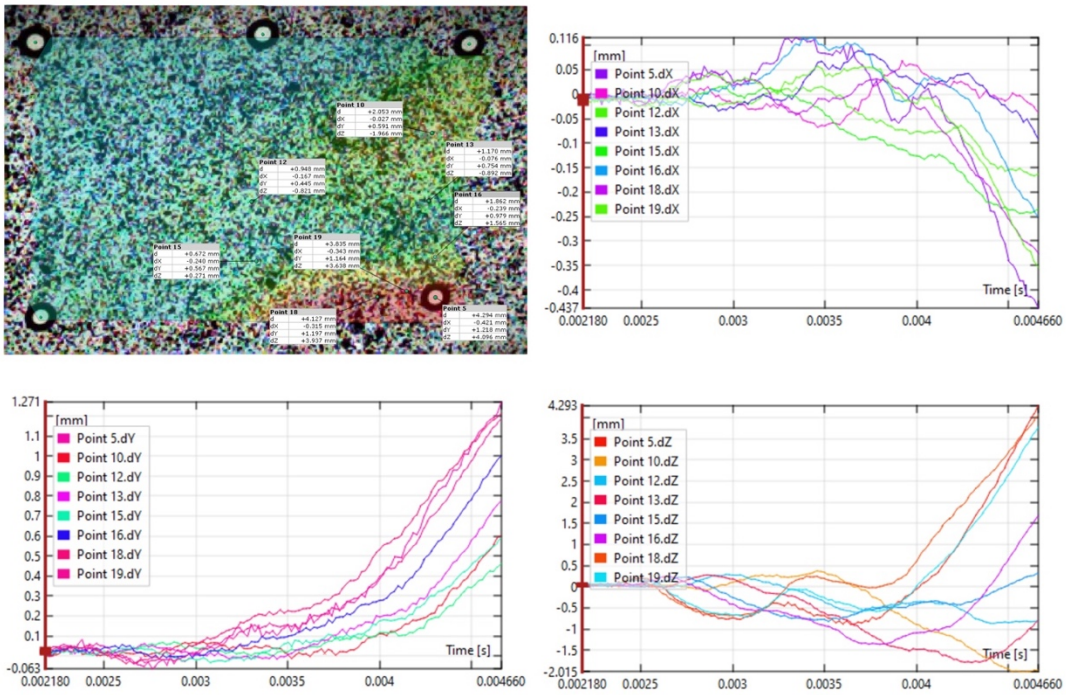


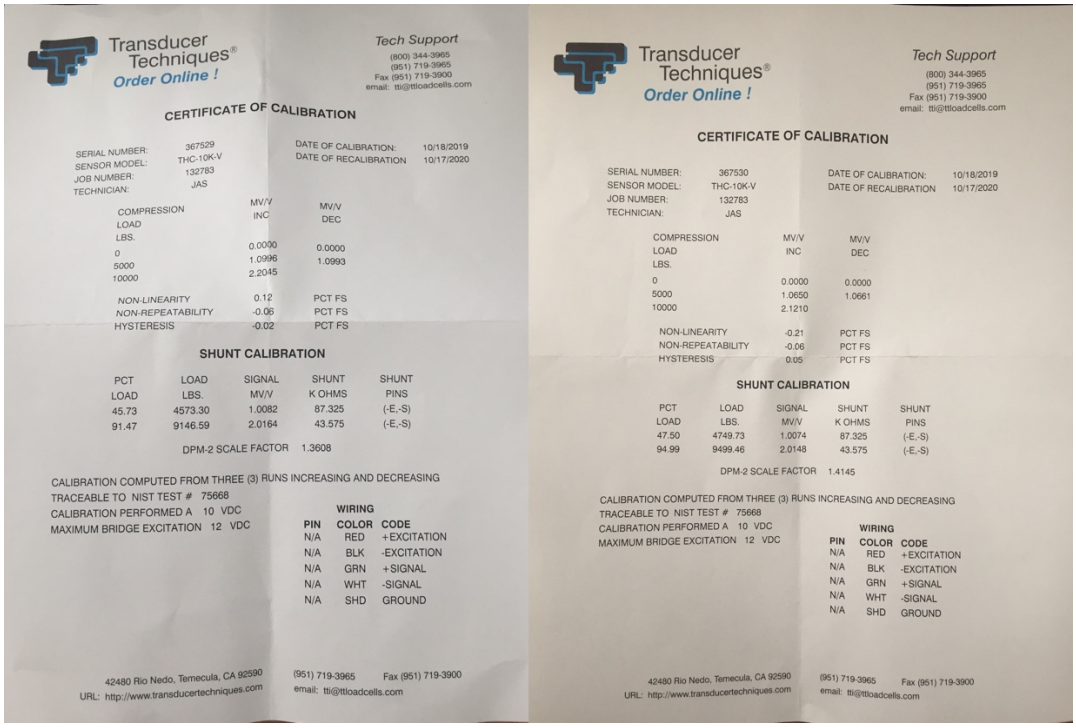

Figure 99. DIC point locations and displacement plots for test A16-GA_0012.

# APPENDIX G

## LOAD CELL USAGE AND CALIBRATION CERTIFICATES

Table 21. Load cell numbering system, test usage, and equipment.

| Load Cell Model | Load Cell Serial # | Load Cell # | Test | Load Cell # | Position # |
|---|---|---|---|---|---|
| THC-10K-V | 367529 | 0 | A-16-GA_0001 | 0,1 | 0,1 |
| THC-10K-V | 367530 | 1 | A-16-GA_0002 | 2,3 | 0,1 |
| THC-10K-V | 369720 | 2 | A-16-GA_0003 | 11,12,8 | 0,1,2 |
| THC-10K-V | 367531 | 3 | A-16-GA_0004 | 11,12,8 | 0,1,2 |
| THC-10K-V | 369721 | 4 | A-16-GA_0005 | 8,1,2,3,4,5,10,9 | 0,1,2,3,4,5,6,7 |
| THC-10K-V | 367532 | 5 | A-16-GA_0006 | 8,1,2,3,4,5,9,10 | 0,1,2,3,4,5,6,7 |
| THC-10K-V | 369722 | 6 | A-16-GA_0007 | 8,1,2,3,4,5,9,10 | 0,1,2,3,4,5,6,7 |
| THC-10K-V | 369723 | 7 | A-16-GA_0008 | 8,1,2,3,4,5,9,10 | 0,1,2,3,4,5,6,7 |
| THC-10K-V | 373742 | 8 | A-16-GA_0009 | 8,1,2,3,4,5,9,10 | 0,1,2,3,4,5,6,7 |
| THC-10K-V | 373743 | 9 | A-16-GA_0010 | 8,1,2,3,4,5,9,10 | 0,1,2,3,4,5,6,7 |
| THC-10K-V | 373744 | 10 | A-16-GA_0011 | 8,1,2,3,4,5,9,10 | 0,1,2,3,4,5,6,7 |
| THD-50K-V | 299982 | 11 | A-16-GA_0012 | 8,1,2,3,4,5,9,10 | 0,1,2,3,4,5,6,7 |
| THD-50K-V | 299983 | 12 | | | |
| Equipment | | | | | |
| NI-9205 DAQ | | | | | |
| NI cDAQ-9174 | | | | | |
| BK Precision 1672 | | | | | |



Transducer Techniques®
Order Online !

Tech Support
(800) 344-3965
(951) 719-3965
Fax (951) 719-3900
email: tti@ttloadcells.com

CERTIFICATE OF CALIBRATION

SERIAL NUMBER: 367529
SENSOR MODEL: THC-10K-V
JOB NUMBER: 132783
TECHNICIAN: JAS

DATE OF CALIBRATION: 10/18/2019
DATE OF RECALIBRATION 10/17/2020

| COMPRESSION LOAD LBS. | MV/V INC | MV/V DEC |
|---|---|---|
| 0 | 0.0000 | 0.0000 |
| 5000 | 1.0996 | 1.0993 |
| 10000 | 2.2045 | |
| NON-LINEARITY | 0.12 | PCT FS |
| NON-REPEATABILITY | -0.06 | PCT FS |
| HYSTERESIS | -0.02 | PCT FS |

SHUNT CALIBRATION

| PCT LOAD | LOAD LBS. | SIGNAL MV/V | SHUNT K OHMS | SHUNT PINS |
|---|---|---|---|---|
| 45.73 | 4573.30 | 1.0082 | 87.325 | (-E,-S) |
| 91.47 | 9146.59 | 2.0164 | 43.575 | (-E,-S) |

DPM-2 SCALE FACTOR 1.3608

CALIBRATION COMPUTED FROM THREE (3) RUNS INCREASING AND DECREASING
TRACEABLE TO NIST TEST # 75668
CALIBRATION PERFORMED A 10 VDC
MAXIMUM BRIDGE EXCITATION 12 VDC

WIRING

| PIN | COLOR | CODE |
|---|---|---|
| N/A | RED | +EXCITATION |
| N/A | BLK | -EXCITATION |
| N/A | GRN | +SIGNAL |
| N/A | WHT | -SIGNAL |
| N/A | SHD | GROUND |

42480 Rio Nedo, Temecula, CA 92590
URL: http://www.transducertechniques.com
(951) 719-3965 Fax (951) 719-3900
email: tti@ttloadcells.com

Transducer Techniques®
Order Online !

Tech Support
(800) 344-3965
(951) 719-3965
Fax (951) 719-3900
email: tti@ttloadcells.com

CERTIFICATE OF CALIBRATION

SERIAL NUMBER: 367530
SENSOR MODEL: THC-10K-V
JOB NUMBER: 132783
TECHNICIAN: JAS

DATE OF CALIBRATION: 10/18/2019
DATE OF RECALIBRATION 10/17/2020

| COMPRESSION LOAD LBS. | MV/V INC | MV/V DEC |
|---|---|---|
| 0 | 0.0000 | 0.0000 |
| 5000 | 1.0650 | 1.0661 |
| 10000 | 2.1210 | |
| NON-LINEARITY | -0.21 | PCT FS |
| NON-REPEATABILITY | -0.06 | PCT FS |
| HYSTERESIS | 0.05 | PCT FS |

SHUNT CALIBRATION

| PCT LOAD | LOAD LBS. | SIGNAL MV/V | SHUNT K OHMS | SHUNT PINS |
|---|---|---|---|---|
| 47.50 | 4749.73 | 1.0074 | 87.325 | (-E,-S) |
| 94.99 | 9499.46 | 2.0148 | 43.575 | (-E,-S) |

DPM-2 SCALE FACTOR 1.4145

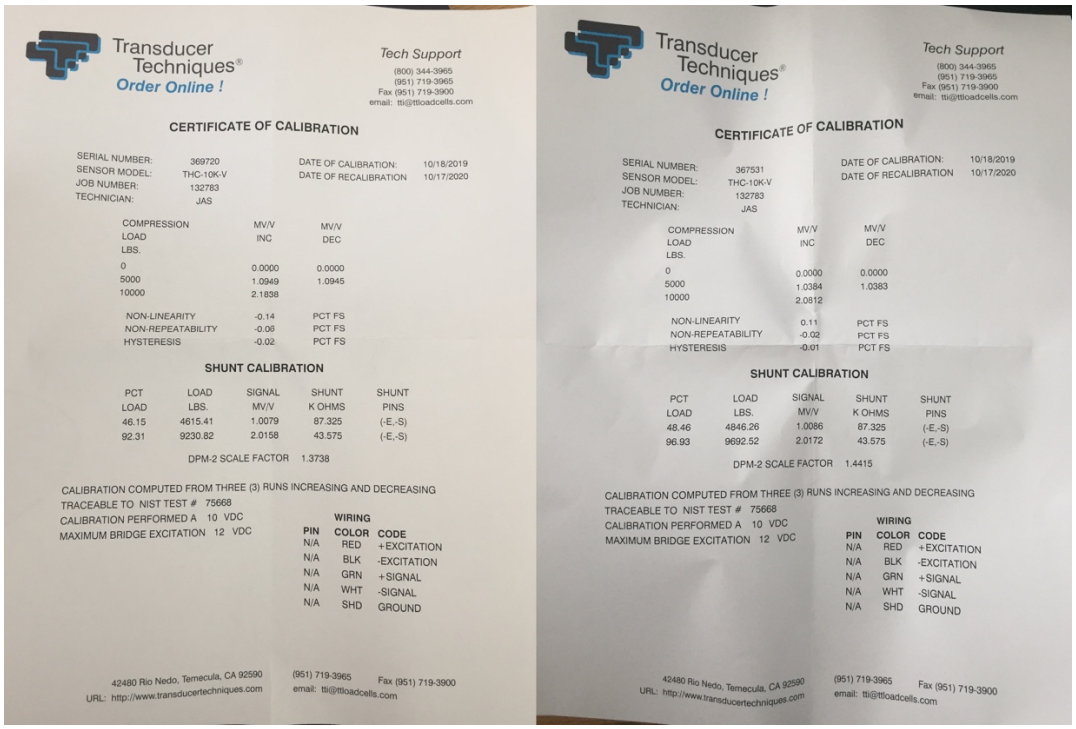
CALIBRATION COMPUTED FROM THREE (3) RUNS INCREASING AND DECREASING
TRACEABLE TO NIST TEST # 75668
CALIBRATION PERFORMED A 10 VDC
MAXIMUM BRIDGE EXCITATION 12 VDC

WIRING

| PIN | COLOR | CODE |
|---|---|---|
| N/A | RED | +EXCITATION |
| N/A | BLK | -EXCITATION |
| N/A | GRN | +SIGNAL |
| N/A | WHT | -SIGNAL |
| N/A | SHD | GROUND |

42480 Rio Nedo, Temecula, CA 92590
URL: http://www.transducertechniques.com
(951) 719-3965 Fax (951) 719-3900
email: tti@ttloadcells.com

Figure 100. Calibration sheets for load cells #0 and #1.



Transducer Techniques®
Order Online !

Tech Support
(800) 344-3965
(951) 719-3965
Fax (951) 719-3900
email: tti@ttloadcells.com

CERTIFICATE OF CALIBRATION

SERIAL NUMBER: 369720
SENSOR MODEL: THC-10K-V
JOB NUMBER: 132783
TECHNICIAN: JAS

DATE OF CALIBRATION: 10/18/2019
DATE OF RECALIBRATION 10/17/2020

| COMPRESSION LOAD LBS. | MV/V INC | MV/V DEC |
|---|---|---|
| 0 | 0.0000 | 0.0000 |
| 5000 | 1.0949 | 1.0945 |
| 10000 | 2.1838 | |
| NON-LINEARITY | -0.14 | PCT FS |
| NON-REPEATABILITY | -0.08 | PCT FS |
| HYSTERESIS | -0.02 | PCT FS |

SHUNT CALIBRATION

| PCT LOAD | LOAD LBS. | SIGNAL MV/V | SHUNT K OHMS | SHUNT PINS |
|---|---|---|---|---|
| 46.15 | 4615.41 | 1.0079 | 87.325 | (-E,-S) |
| 92.31 | 9230.82 | 2.0158 | 43.575 | (-E,-S) |

DPM-2 SCALE FACTOR 1.3738

CALIBRATION COMPUTED FROM THREE (3) RUNS INCREASING AND DECREASING
TRACEABLE TO NIST TEST # 75668
CALIBRATION PERFORMED A 10 VDC
MAXIMUM BRIDGE EXCITATION 12 VDC

WIRING

| PIN | COLOR | CODE |
|---|---|---|
| N/A | RED | +EXCITATION |
| N/A | BLK | -EXCITATION |
| N/A | GRN | +SIGNAL |
| N/A | WHT | -SIGNAL |
| N/A | SHD | GROUND |

42480 Rio Nedo, Temecula, CA 92590
URL: http://www.transducertechniques.com
(951) 719-3965 Fax (951) 719-3900
email: tti@ttloadcells.com

Transducer Techniques®
Order Online !

Tech Support
(800) 344-3965
(951) 719-3965
Fax (951) 719-3900
email: tti@ttloadcells.com

CERTIFICATE OF CALIBRATION

SERIAL NUMBER: 367531
SENSOR MODEL: THC-10K-V
JOB NUMBER: 132783
TECHNICIAN: JAS

DATE OF CALIBRATION: 10/18/2019
DATE OF RECALIBRATION 10/17/2020

| COMPRESSION LOAD LBS. | MV/V INC | MV/V DEC |
|---|---|---|
| 0 | 0.0000 | 0.0000 |
| 5000 | 1.0384 | 1.0383 |
| 10000 | 2.0812 | |
| NON-LINEARITY | 0.11 | PCT FS |
| NON-REPEATABILITY | -0.02 | PCT FS |
| HYSTERESIS | -0.01 | PCT FS |

SHUNT CALIBRATION

| PCT LOAD | LOAD LBS. | SIGNAL MV/V | SHUNT K OHMS | SHUNT PINS |
|---|---|---|---|---|
| 48.46 | 4846.26 | 1.0086 | 87.325 | (-E,-S) |
| 96.93 | 9692.52 | 2.0172 | 43.575 | (-E,-S) |

DPM-2 SCALE FACTOR 1.4415

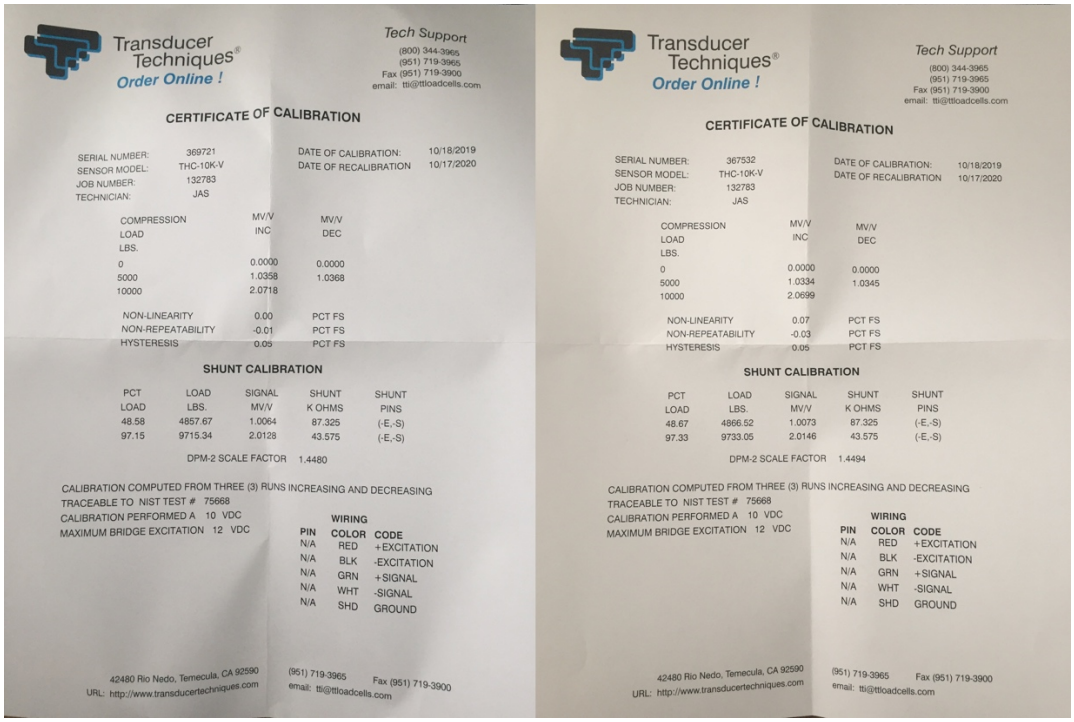
CALIBRATION COMPUTED FROM THREE (3) RUNS INCREASING AND DECREASING
TRACEABLE TO NIST TEST # 75668
CALIBRATION PERFORMED A 10 VDC
MAXIMUM BRIDGE EXCITATION 12 VDC

WIRING

| PIN | COLOR | CODE |
|---|---|---|
| N/A | RED | +EXCITATION |
| N/A | BLK | -EXCITATION |
| N/A | GRN | +SIGNAL |
| N/A | WHT | -SIGNAL |
| N/A | SHD | GROUND |

42480 Rio Nedo, Temecula, CA 92590
URL: http://www.transducertechniques.com
(951) 719-3965 Fax (951) 719-3900
email: tti@ttloadcells.com

Figure 101. Calibration sheets for load cells #2 and #3.



Transducer Techniques®
Order Online !

Tech Support
(800) 344-3965
(951) 719-3965
Fax (951) 719-3900
email: tti@ttloadcells.com

CERTIFICATE OF CALIBRATION

SERIAL NUMBER: 369721
SENSOR MODEL: THC-10K-V
JOB NUMBER: 132783
TECHNICIAN: JAS

DATE OF CALIBRATION: 10/18/2019
DATE OF RECALIBRATION 10/17/2020

| COMPRESSION LOAD LBS. | MV/V INC | MV/V DEC |
|---|---|---|
| 0 | 0.0000 | 0.0000 |
| 5000 | 1.0358 | 1.0368 |
| 10000 | 2.0718 | |
| NON-LINEARITY | 0.00 | PCT FS |
| NON-REPEATABILITY | -0.01 | PCT FS |
| HYSTERESIS | 0.05 | PCT FS |

SHUNT CALIBRATION

| PCT LOAD | LOAD LBS. | SIGNAL MV/V | SHUNT K OHMS | SHUNT PINS |
|---|---|---|---|---|
| 48.58 | 4857.67 | 1.0064 | 87.325 | (-E,-S) |
| 97.15 | 9715.34 | 2.0128 | 43.575 | (-E,-S) |

DPM-2 SCALE FACTOR 1.4480

CALIBRATION COMPUTED FROM THREE (3) RUNS INCREASING AND DECREASING
TRACEABLE TO NIST TEST # 75668
CALIBRATION PERFORMED A 10 VDC
MAXIMUM BRIDGE EXCITATION 12 VDC

WIRING

| PIN | COLOR | CODE |
|---|---|---|
| N/A | RED | +EXCITATION |
| N/A | BLK | -EXCITATION |
| N/A | GRN | +SIGNAL |
| N/A | WHT | -SIGNAL |
| N/A | SHD | GROUND |

42480 Rio Nedo, Temecula, CA 92590
URL: http://www.transducertechniques.com
(951) 719-3965 Fax (951) 719-3900
email: tti@ttloadcells.com

Transducer Techniques®
Order Online !

Tech Support
(800) 344-3965
(951) 719-3965
Fax (951) 719-3900
email: tti@ttloadcells.com

CERTIFICATE OF CALIBRATION

SERIAL NUMBER: 367532
SENSOR MODEL: THC-10K-V
JOB NUMBER: 132783
TECHNICIAN: JAS

DATE OF CALIBRATION: 10/18/2019
DATE OF RECALIBRATION 10/17/2020

| COMPRESSION LOAD LBS. | MV/V INC | MV/V DEC |
|---|---|---|
| 0 | 0.0000 | 0.0000 |
| 5000 | 1.0334 | 1.0345 |
| 10000 | 2.0699 | |
| NON-LINEARITY | 0.07 | PCT FS |
| NON-REPEATABILITY | -0.03 | PCT FS |
| HYSTERESIS | 0.05 | PCT FS |

SHUNT CALIBRATION

| PCT LOAD | LOAD LBS. | SIGNAL MV/V | SHUNT K OHMS | SHUNT PINS |
|---|---|---|---|---|
| 48.67 | 4866.52 | 1.0073 | 87.325 | (-E,-S) |
| 97.33 | 9733.05 | 2.0146 | 43.575 | (-E,-S) |

DPM-2 SCALE FACTOR 1.4494

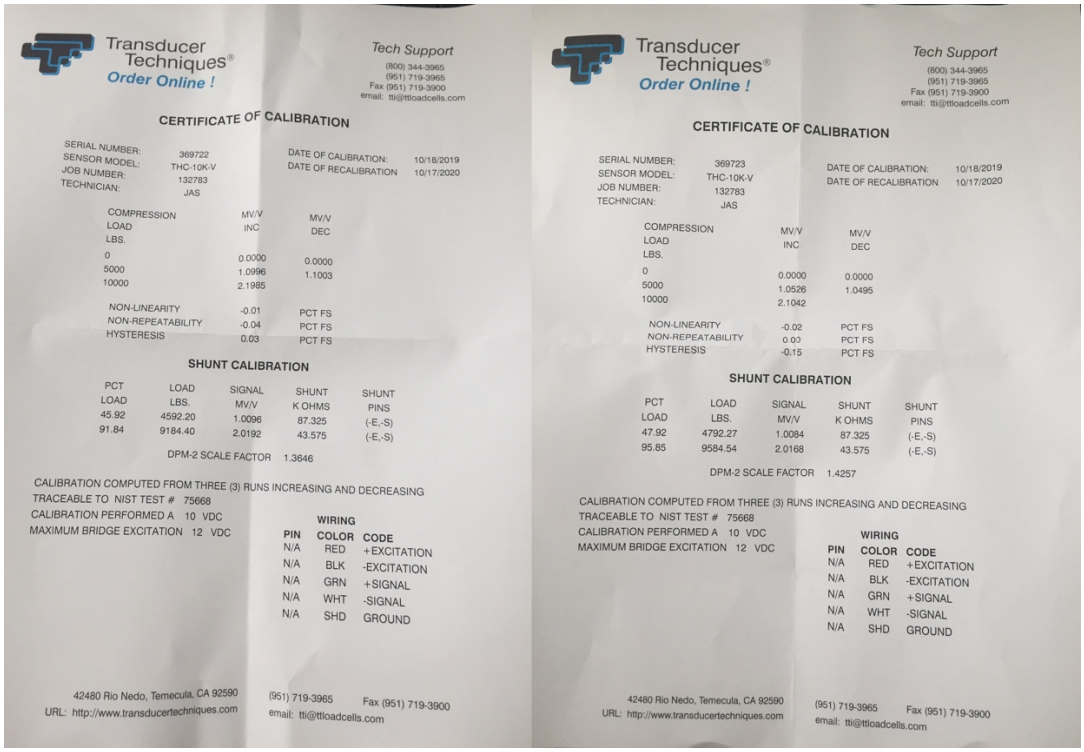
CALIBRATION COMPUTED FROM THREE (3) RUNS INCREASING AND DECREASING
TRACEABLE TO NIST TEST # 75668
CALIBRATION PERFORMED A 10 VDC
MAXIMUM BRIDGE EXCITATION 12 VDC

WIRING

| PIN | COLOR | CODE |
|---|---|---|
| N/A | RED | +EXCITATION |
| N/A | BLK | -EXCITATION |
| N/A | GRN | +SIGNAL |
| N/A | WHT | -SIGNAL |
| N/A | SHD | GROUND |

42480 Rio Nedo, Temecula, CA 92590
URL: http://www.transducertechniques.com
(951) 719-3965 Fax (951) 719-3900
email: tti@ttloadcells.com

Figure 102. Calibration sheets for load cells #4 and #5.



Transducer Techniques®
Order Online !

Tech Support
(800) 344-3965
(951) 719-3965
Fax (951) 719-3900
email: tti@ttloadcells.com

CERTIFICATE OF CALIBRATION

SERIAL NUMBER: 369722
SENSOR MODEL: THC-10K-V
JOB NUMBER: 132783
TECHNICIAN: JAS

DATE OF CALIBRATION: 10/18/2019
DATE OF RECALIBRATION 10/17/2020

| COMPRESSION LOAD LBS. | MV/V INC | MV/V DEC |
|---|---|---|
| 0 | 0.0000 | 0.0000 |
| 5000 | 1.0996 | 1.1003 |
| 10000 | 2.1985 | |
| NON-LINEARITY | -0.01 | PCT FS |
| NON-REPEATABILITY | -0.04 | PCT FS |
| HYSTERESIS | 0.03 | PCT FS |

SHUNT CALIBRATION

| PCT LOAD | LOAD LBS. | SIGNAL MV/V | SHUNT K OHMS | SHUNT PINS |
|---|---|---|---|---|
| 45.92 | 4592.20 | 1.0096 | 87.325 | (-E,-S) |
| 91.84 | 9184.40 | 2.0192 | 43.575 | (-E,-S) |

DPM-2 SCALE FACTOR 1.3646

CALIBRATION COMPUTED FROM THREE (3) RUNS INCREASING AND DECREASING
TRACEABLE TO NIST TEST # 75668
CALIBRATION PERFORMED A 10 VDC
MAXIMUM BRIDGE EXCITATION 12 VDC

WIRING

| PIN | COLOR | CODE |
|---|---|---|
| N/A | RED | +EXCITATION |
| N/A | BLK | -EXCITATION |
| N/A | GRN | +SIGNAL |
| N/A | WHT | -SIGNAL |
| N/A | SHD | GROUND |

42480 Rio Nedo, Temecula, CA 92590
URL: http://www.transducertechniques.com
(951) 719-3965 Fax (951) 719-3900
email: tti@ttloadcells.com

Transducer Techniques®
Order Online !

Tech Support
(800) 344-3965
(951) 719-3965
Fax (951) 719-3900
email: tti@ttloadcells.com

CERTIFICATE OF CALIBRATION

SERIAL NUMBER: 369723
SENSOR MODEL: THC-10K-V
JOB NUMBER: 132783
TECHNICIAN: JAS

DATE OF CALIBRATION: 10/18/2019
DATE OF RECALIBRATION 10/17/2020

| COMPRESSION LOAD LBS. | MV/V INC | MV/V DEC |
|---|---|---|
| 0 | 0.0000 | 0.0000 |
| 5000 | 1.0526 | 1.0495 |
| 10000 | 2.1042 | |
| NON-LINEARITY | -0.02 | PCT FS |
| NON-REPEATABILITY | 0.00 | PCT FS |
| HYSTERESIS | -0.15 | PCT FS |

SHUNT CALIBRATION

| PCT LOAD | LOAD LBS. | SIGNAL MV/V | SHUNT K OHMS | SHUNT PINS |
|---|---|---|---|---|
| 47.92 | 4792.27 | 1.0084 | 87.325 | (-E,-S) |
| 95.85 | 9584.54 | 2.0168 | 43.575 | (-E,-S) |

DPM-2 SCALE FACTOR 1.4257

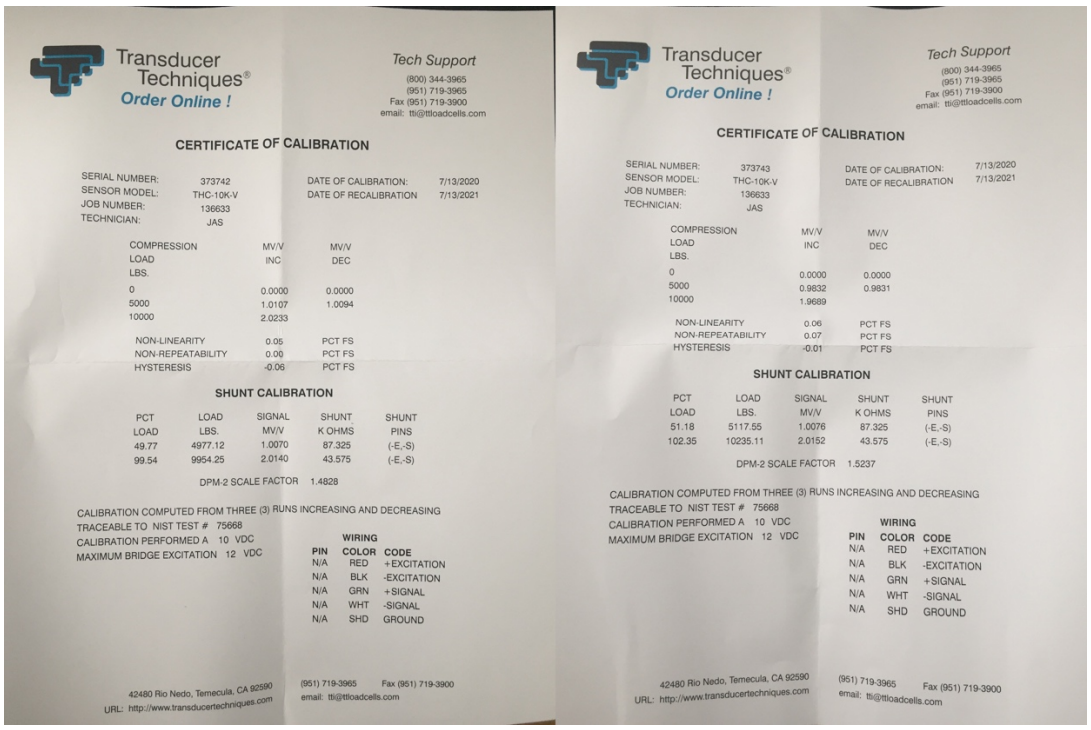
CALIBRATION COMPUTED FROM THREE (3) RUNS INCREASING AND DECREASING
TRACEABLE TO NIST TEST # 75668
CALIBRATION PERFORMED A 10 VDC
MAXIMUM BRIDGE EXCITATION 12 VDC

WIRING

| PIN | COLOR | CODE |
|---|---|---|
| N/A | RED | +EXCITATION |
| N/A | BLK | -EXCITATION |
| N/A | GRN | +SIGNAL |
| N/A | WHT | -SIGNAL |
| N/A | SHD | GROUND |

42480 Rio Nedo, Temecula, CA 92590
URL: http://www.transducertechniques.com
(951) 719-3965 Fax (951) 719-3900
email: tti@ttloadcells.com

Figure 103. Calibration sheets for load cells #6 and #7.



Transducer Techniques®
Order Online !

Tech Support
(800) 344-3965
(951) 719-3965
Fax (951) 719-3900
email: tti@ttloadcells.com

CERTIFICATE OF CALIBRATION

SERIAL NUMBER: 373742
SENSOR MODEL: THC-10K-V
JOB NUMBER: 136633
TECHNICIAN: JAS

DATE OF CALIBRATION: 7/13/2020
DATE OF RECALIBRATION 7/13/2021

| COMPRESSION LOAD LBS. | MV/V INC | MV/V DEC |
|---|---|---|
| 0 | 0.0000 | 0.0000 |
| 5000 | 1.0107 | 1.0094 |
| 10000 | 2.0233 | |

| | | |
|---|---|---|
| NON-LINEARITY | 0.05 | PCT FS |
| NON-REPEATABILITY | 0.00 | PCT FS |
| HYSTERESIS | -0.06 | PCT FS |

SHUNT CALIBRATION

| PCT LOAD | LOAD LBS. | SIGNAL MV/V | SHUNT K OHMS | SHUNT PINS |
|---|---|---|---|---|
| 49.77 | 4977.12 | 1.0070 | 87.325 | (-E,-S) |
| 99.54 | 9954.25 | 2.0140 | 43.575 | (-E,-S) |

DPM-2 SCALE FACTOR 1.4828

CALIBRATION COMPUTED FROM THREE (3) RUNS INCREASING AND DECREASING
TRACEABLE TO NIST TEST # 75668
CALIBRATION PERFORMED A 10 VDC
MAXIMUM BRIDGE EXCITATION 12 VDC

WIRING

| PIN | COLOR | CODE |
|---|---|---|
| N/A | RED | +EXCITATION |
| N/A | BLK | -EXCITATION |
| N/A | GRN | +SIGNAL |
| N/A | WHT | -SIGNAL |
| N/A | SHD | GROUND |

42480 Rio Nedo, Temecula, CA 92590
URL: http://www.transducertechniques.com
(951) 719-3965 Fax (951) 719-3900
email: tti@ttloadcells.com

Transducer Techniques®
Order Online !

Tech Support
(800) 344-3965
(951) 719-3965
Fax (951) 719-3900
email: tti@ttloadcells.com

CERTIFICATE OF CALIBRATION

SERIAL NUMBER: 373743
SENSOR MODEL: THC-10K-V
JOB NUMBER: 136633
TECHNICIAN: JAS

DATE OF CALIBRATION: 7/13/2020
DATE OF RECALIBRATION 7/13/2021

| COMPRESSION LOAD LBS. | MV/V INC | MV/V DEC |
|---|---|---|
| 0 | 0.0000 | 0.0000 |
| 5000 | 0.9832 | 0.9831 |
| 10000 | 1.9689 | |

| | | |
|---|---|---|
| NON-LINEARITY | 0.06 | PCT FS |
| NON-REPEATABILITY | 0.07 | PCT FS |
| HYSTERESIS | -0.01 | PCT FS |

SHUNT CALIBRATION

| PCT LOAD | LOAD LBS. | SIGNAL MV/V | SHUNT K OHMS | SHUNT PINS |
|---|---|---|---|---|
| 51.18 | 5117.55 | 1.0076 | 87.325 | (-E,-S) |
| 102.35 | 10235.11 | 2.0152 | 43.575 | (-E,-S) |

DPM-2 SCALE FACTOR 1.5237

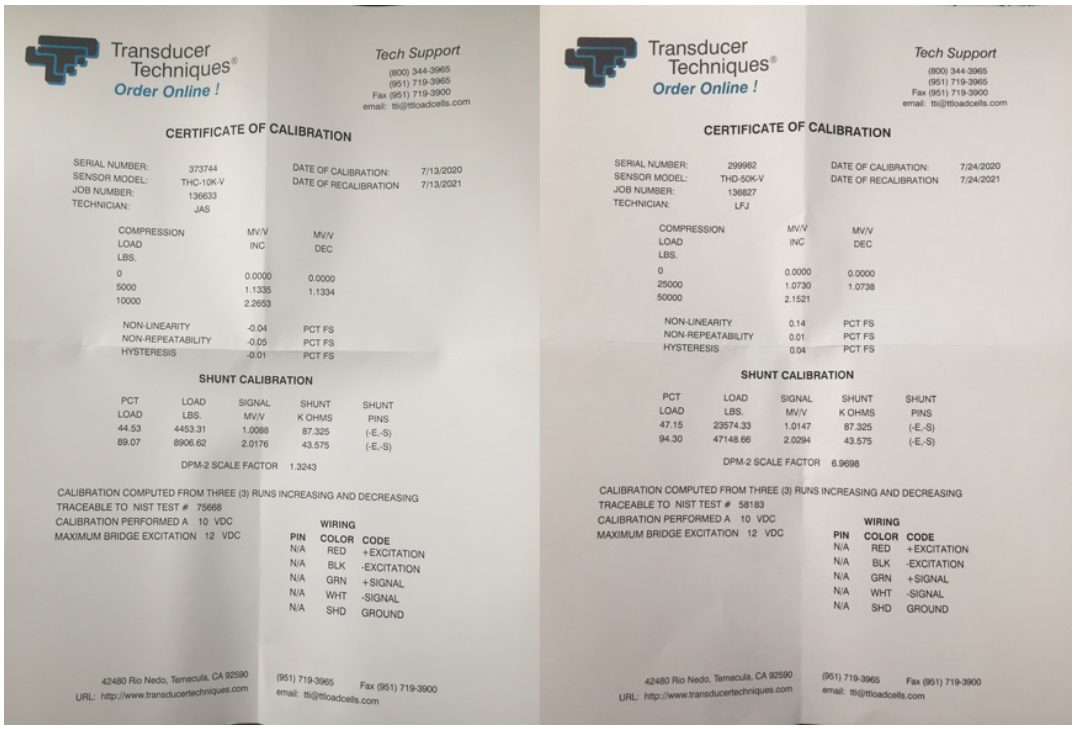
CALIBRATION COMPUTED FROM THREE (3) RUNS INCREASING AND DECREASING
TRACEABLE TO NIST TEST # 75668
CALIBRATION PERFORMED A 10 VDC
MAXIMUM BRIDGE EXCITATION 12 VDC

WIRING

| PIN | COLOR | CODE |
|---|---|---|
| N/A | RED | +EXCITATION |
| N/A | BLK | -EXCITATION |
| N/A | GRN | +SIGNAL |
| N/A | WHT | -SIGNAL |
| N/A | SHD | GROUND |

42480 Rio Nedo, Temecula, CA 92590
URL: http://www.transducertechniques.com
(951) 719-3965 Fax (951) 719-3900
email: tti@ttloadcells.com

Figure 104. Calibration sheets for load cells #8 and #9.



Transducer Techniques®
Order Online !

Tech Support
(800) 344-3965
(951) 719-3965
Fax (951) 719-3900
email: tti@ttloadcells.com

CERTIFICATE OF CALIBRATION

SERIAL NUMBER: 373744
SENSOR MODEL: THC-10K-V
JOB NUMBER: 136633
TECHNICIAN: JAS

DATE OF CALIBRATION: 7/13/2020
DATE OF RECALIBRATION 7/13/2021

| COMPRESSION LOAD LBS. | MV/V INC | MV/V DEC |
|---|---|---|
| 0 | 0.0000 | 0.0000 |
| 5000 | 1.1335 | 1.1334 |
| 10000 | 2.2653 | |

| | | |
|---|---|---|
| NON-LINEARITY | -0.04 | PCT FS |
| NON-REPEATABILITY | -0.05 | PCT FS |
| HYSTERESIS | -0.01 | PCT FS |

SHUNT CALIBRATION

| PCT LOAD | LOAD LBS. | SIGNAL MV/V | SHUNT K OHMS | SHUNT PINS |
|---|---|---|---|---|
| 44.53 | 4453.31 | 1.0088 | 87.325 | (-E,-S) |
| 89.07 | 8906.62 | 2.0176 | 43.575 | (-E,-S) |

DPM-2 SCALE FACTOR 1.3243

CALIBRATION COMPUTED FROM THREE (3) RUNS INCREASING AND DECREASING
TRACEABLE TO NIST TEST # 75668
CALIBRATION PERFORMED A 10 VDC
MAXIMUM BRIDGE EXCITATION 12 VDC

WIRING

| PIN | COLOR | CODE |
|---|---|---|
| N/A | RED | +EXCITATION |
| N/A | BLK | -EXCITATION |
| N/A | GRN | +SIGNAL |
| N/A | WHT | -SIGNAL |
| N/A | SHD | GROUND |

42480 Rio Nedo, Temecula, CA 92590
URL: http://www.transducertechniques.com
(951) 719-3965 Fax (951) 719-3900
email: tti@ttloadcells.com

Transducer Techniques®
Order Online !

Tech Support
(800) 344-3965
(951) 719-3965
Fax (951) 719-3900
email: tti@ttloadcells.com

CERTIFICATE OF CALIBRATION

SERIAL NUMBER: 299982
SENSOR MODEL: THD-50K-V
JOB NUMBER: 136827
TECHNICIAN: LFJ

DATE OF CALIBRATION: 7/24/2020
DATE OF RECALIBRATION 7/24/2021

| COMPRESSION LOAD LBS. | MV/V INC | MV/V DEC |
|---|---|---|
| 0 | 0.0000 | 0.0000 |
| 25000 | 1.0730 | 1.0738 |
| 50000 | 2.1521 | |

| | | |
|---|---|---|
| NON-LINEARITY | 0.14 | PCT FS |
| NON-REPEATABILITY | 0.01 | PCT FS |
| HYSTERESIS | 0.04 | PCT FS |

SHUNT CALIBRATION

| PCT LOAD | LOAD LBS. | SIGNAL MV/V | SHUNT K OHMS | SHUNT PINS |
|---|---|---|---|---|
| 47.15 | 23574.33 | 1.0147 | 87.325 | (-E,-S) |
| 94.30 | 47148.66 | 2.0294 | 43.575 | (-E,-S) |

DPM-2 SCALE FACTOR 6.9698

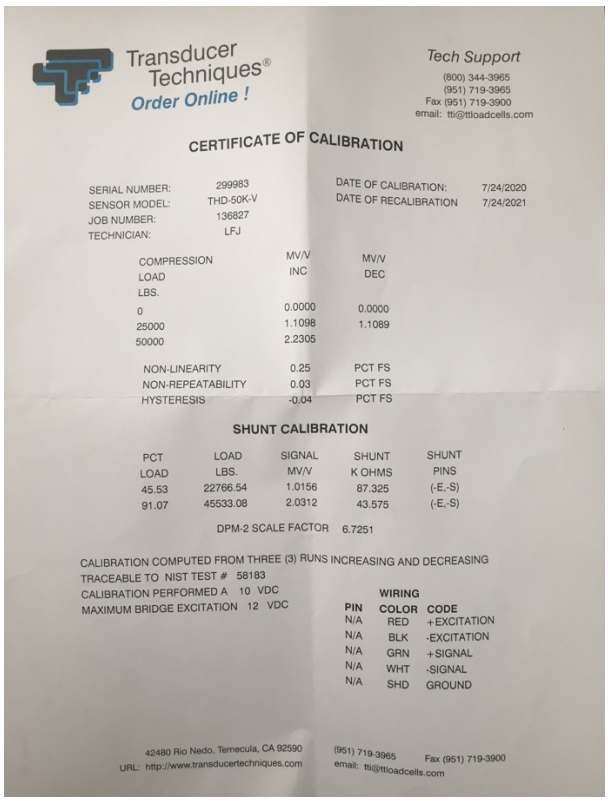
CALIBRATION COMPUTED FROM THREE (3) RUNS INCREASING AND DECREASING
TRACEABLE TO NIST TEST # 58183
CALIBRATION PERFORMED A 10 VDC
MAXIMUM BRIDGE EXCITATION 12 VDC

WIRING

| PIN | COLOR | CODE |
|---|---|---|
| N/A | RED | +EXCITATION |
| N/A | BLK | -EXCITATION |
| N/A | GRN | +SIGNAL |
| N/A | WHT | -SIGNAL |
| N/A | SHD | GROUND |

42480 Rio Nedo, Temecula, CA 92590
URL: http://www.transducertechniques.com
(951) 719-3965 Fax (951) 719-3900
email: tti@ttloadcells.com

Figure 105. Calibration sheets for load cells #10 and #11.



Transducer Techniques®
Order Online !

Tech Support
(800) 344-3965
(951) 719-3965
Fax (951) 719-3900
email: tti@ttloadcells.com

CERTIFICATE OF CALIBRATION

SERIAL NUMBER: 299983
SENSOR MODEL: THD-50K-V
JOB NUMBER: 136827
TECHNICIAN: LFJ

DATE OF CALIBRATION: 7/24/2020
DATE OF RECALIBRATION 7/24/2021

| COMPRESSION LOAD LBS. | MV/V INC | MV/V DEC |
|---|---|---|
| 0 | 0.0000 | 0.0000 |
| 25000 | 1.1098 | 1.1089 |
| 50000 | 2.2305 | |

| | | |
|---|---|---|
| NON-LINEARITY | 0.25 | PCT FS |
| NON-REPEATABILITY | 0.03 | PCT FS |
| HYSTERESIS | -0.04 | PCT FS |

SHUNT CALIBRATION

| PCT LOAD | LOAD LBS. | SIGNAL MV/V | SHUNT K OHMS | SHUNT PINS |
|---|---|---|---|---|
| 45.53 | 22766.54 | 1.0156 | 87.325 | (-E,-S) |
| 91.07 | 45533.08 | 2.0312 | 43.575 | (-E,-S) |

DPM-2 SCALE FACTOR 6.7251

CALIBRATION COMPUTED FROM THREE (3) RUNS INCREASING AND DECREASING
TRACEABLE TO NIST TEST # 58183
CALIBRATION PERFORMED A 10 VDC
MAXIMUM BRIDGE EXCITATION 12 VDC

WIRING

| PIN | COLOR | CODE |
|---|---|---|
| N/A | RED | +EXCITATION |
| N/A | BLK | -EXCITATION |
| N/A | GRN | +SIGNAL |
| N/A | WHT | -SIGNAL |
| N/A | SHD | GROUND |

42480 Rio Nedo, Temecula, CA 92590
URL: http://www.transducertechniques.com
(951) 719-3965
email: tti@ttloadcells.com
Fax (951) 719-3900

Figure 106. Calibration sheet for load cell #12.

# APPENDIX H

## LOAD CELL POST PROCESSING CODES

MATLAB_R2018b was used to process load cell results from testing. The code shown below is for post processing of strut results, but is easily adapted to accommodate the additional load cells required for wing and windscreen testing.

**Inputs**

```
filename = 'A16-GA_0001_RawVoltageData.xlsx'   % Make sure that the file is in path
SRate = 25;         % kHz, Sample rate
LC_Calib = [2.2045,2.121];     % mV/V, Response at full load
Full_Load = [10000,10000];  % lbs, full load
V_excite = 10;      % V, excitation voltage

% Variable that effect the found loading event section
LC_filter = 0.5;        % mV spike required to show data
indexshiftin  = 200;    % number of points to include before the filter activates
indexshiftout = 20000;    % number of points to be included after the out filter
```

**Import data and assign to load cells (comment this section out for repeated runs of the same file)**

Comment out this whole section if your running the same file again and the variables are already saved in memory since the importdata function takes so long

```
LCimport = importdata(filename);
LCinOG = LCimport.data.MeasuredData*1000; % Import convert to mV, ms
Time = (0:(length(LCinOG)-1))/SRate;


%%%%%%%%%%%%%%%%%%%% Not used variables, just a note about
% LC_0 = LCin(:,1); how the data is stored
% LC_1 = LCin(:,2);
% LC_2 = LCin(:,3);
% LC_3 = LCin(:,4);
%%%%%%%%%%%%%%%%%%%%
```

**Moving median filter of the data**

I am only applying this filter to find the loading event I don't know if it is a suitable filter otherwise as it may cause artificial reduction in peak loading

```
LCinfilt2 = movmedian(LCinOG,5);
```

**Find Loading event**

```
LCin = zeros(size(LCinOG));
NumLC = size(LCinOG,2);

for j = 1:NumLC
    LCzero = mean(LCinfilt2(2000:1000*SRate,j));  % Throw out the first 200 points and average over 2 seconds
    LCinfilt2(:,j) = LCinfilt2(:,j) - LCzero;     % Zero Filtered data
    LCin(:,j) = LCinOG(:,j) - LCzero;             % Zero raw data
    for i = 2000:length(LCinfilt2)
        check = abs(LCinfilt2(i,j));
        if check > LC_filter                    % Index location when the load cell meets the filter
            indexinI(j) = i;
            break
        elseif i == length(LCinfilt2)            % If the load cell does not meet the filter, input the last data point
            indexinI(j) = i;
        end
    end
end

indexin = min(indexinI) - indexshiftin;


for j = 1:NumLC
    checkave = mean(LCinfilt2((end-250):(end-1),j));
    for i = length(LCinfilt2-10):-1:1
        check = abs(checkave-LCinfilt2(i,j));
        if check > LC_filter
            indexoutI(j) = i;
            break
        elseif i == 1
            indexoutI(j) = i;
        end
    end
end
indexout = max(indexoutI) + indexshiftout;
```

**Convert output to load**

```
Load = LCin.*Full_Load./LC_Calib/V_excite;

% Lowpass Filter

d = designfilt('lowpassfir', 'PassbandFrequency', 0.1,...
             'StopbandFrequency', 0.2, 'PassbandRipple', 0.1, ...
             'StopbandAttenuation', 1,'DesignMethod', 'kaiserwin');


LCinfilt = filter(d,LCin);

LoadNoOutliers = filloutliers(Load,'center','movmean',500); % Removing outliers from data

FiltLoad = LCinfilt.*Full_Load./LC_Calib/V_excite;

% Find the standard deviation of the zero load data
StDev_lbf = std(LoadNoOutliers(200:(indexin-indexshiftin),:))

N = (indexin-indexshiftin)-200;  % Number of Samples

StDev_ofmean_lbf = StDev_lbf/sqrt(N)
```

**Plot Filtered Signal**

```
figure
leg = {};
hold on
for i = 1:NumLC
    plot(Time,LCinfilt(:,i))
    leg = horzcat(leg,{horzcat('Load Cell ',num2str(i-1))});
end

title('Filtered Load Cell Signal')
xlabel('Time (ms))')
ylabel('Voltage(mV)')
legend(leg)
```

### Plot Full Signal

```
figure
hold on
for i = 1:NumLC
    plot(Time,LCin(:,i))
end

title('Full Load Cell Signal')
xlabel('Time (ms))')
ylabel('Voltage(mV)')
legend(leg)
```

### Plot Impact Signal

```
figure
hold on
for i = 1:NumLC
    plot(Time(indexin:indexout),LoadNoOutliers(indexin:indexout,i))
end

title('Impact Event Load Cell Signal')
xlabel('Time (ms))')
ylabel('Load(lbf)')
legend(leg)
axis([Time(indexin), Time(indexout),...
        1.2*min(min(LoadNoOutliers(indexin:indexout,1:NumLC))), 1.2*max(max(Load(indexin:indexout,1:NumLC)))])

figure
color = [     0 0.4470 0.7410;...
         0.8500 0.3250 0.0980;...
         0.9290 0.6940 0.1250;...
         0.4940 0.1840 0.5560;...
         0.4660 0.6740 0.1880;...
         0.3010 0.7450 0.9330;...
         0.6350 0.0780 0.1840;
         1      0      0     ];
for i = 1:NumLC
    subplot(2,ceil(NumLC/2),i)
    plot(Time(indexin:indexout),LoadNoOutliers(indexin:indexout,i),'Color',color(i,:))
    title({'Impact Event Load Cell Signal',['Load Cell ' num2str(i-1)]})
    xlabel('Time (ms))')
    ylabel('Load (lbf)')
    %axis([Time(indexin), Time(indexout),...
        %1.2*min(min(Load(indexin:indexout,1:NumLC))), 1.2*max(max(Load(indexin:indexout,1:NumLC)))])
axis([Time(indexin), Time(indexout),...
        -1500, 1.2*max(max(LoadNoOutliers(indexin:indexout,1:NumLC)))])
end

figure
for i = 1:NumLC
    subplot(2,ceil(NumLC/2),i)
    plot(Time(indexin:indexout),FiltLoad(indexin:indexout,i),'Color',color(i,:))
    title({'Impact Event Load Cell Signal (filt)',['Load Cell ' num2str(i-1)]})
    xlabel('Time (ms))')
    ylabel('Load (lbf)')
    axis([Time(indexin), Time(indexout),...
        1.2*min(min(FiltLoad(indexin:indexout,1:NumLC))), 1.2*max(max(FiltLoad(indexin:indexout,1:NumLC)))])
end
```

---

### Output Peak Loads

```
    max(LoadNoOutliers)
```

### Output Load Cell Data to .CSV

```
T = array2table(Load);
TIME = array2table(Time');
TIME.Properties.VariableNames(1) = {'Time_ms'};
T.Properties.VariableNames(1:2) = {'LC0','LC1'};
Output_Matrix = [TIME T];
writetable(Output_Matrix,'A16-GA_0002_LoadCellData(lbf).csv');
```

# APPENDIX I

## DIC SYSTEM INFORMATION AND CALIBRATION QUALITY RESULTS

Table 22. DIC equipment.

| Item | Quantity |
|---|---|
| Photron NOVA s6 | 2 |
| ES PHSI3060 120 watt LED | 2 |
| Nikon 20mm lens f/1.8g | 2 |
| APC Pro 1500 Battery Backup | 1 |

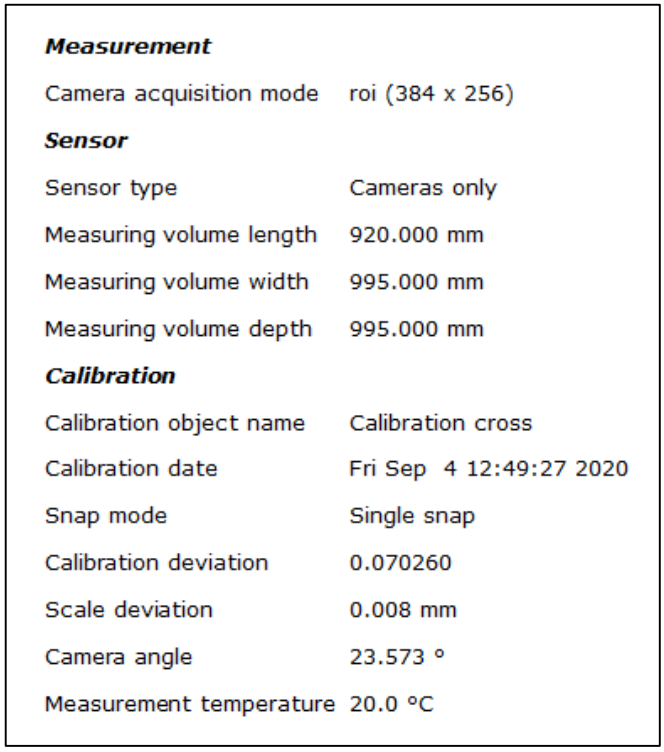



Figure 107. DIC calibration quality data for test A16-GA_0005 from GOM Correlate.

| | |
|---|---|
| ***Measurement*** | |
| Camera acquisition mode | roi (384 x 256) |
| ***Sensor*** | |
| Sensor type | Cameras only |
| Measuring volume length | 950.000 mm |
| Measuring volume width | 1025.000 mm |
| Measuring volume depth | 1025.000 mm |
| ***Calibration*** | |
| Calibration object name | Calibration cross |
| Calibration date | Fri Sep 11 10:47:57 2020 |
| Snap mode | Single snap |
| Calibration deviation | 0.119381 |
| Scale deviation | 0.011 mm |
| Camera angle | 22.965 ° |
| Measurement temperature | 20.0 °C |

Figure 108. DIC calibration quality data for test A16-GA_0006 from GOM Correlate.

| | |
|---|---|
| ***Measurement*** | |
| Camera acquisition mode | roi (384 x 256) |
| ***Sensor*** | |
| Sensor type | Cameras only |
| Measuring volume length | 965.000 mm |
| Measuring volume width | 1040.000 mm |
| Measuring volume depth | 1040.000 mm |
| ***Calibration*** | |
| Calibration object name | Calibration cross |
| Calibration date | Fri Sep 18 10:59:54 2020 |
| Snap mode | Single snap |
| Calibration deviation | 0.071572 |
| Scale deviation | 0.003 mm |
| Camera angle | 22.731 ° |
| Measurement temperature | 20.0 °C |

Figure 109. DIC calibration quality data for tests A16-GA_0007 – A16-GA_0009 from GOM Correlate.

| | |
|---|---|
| ***Measurement*** | |
| Camera acquisition mode | roi (384 x 256) |
| ***Sensor*** | |
| Sensor type | Cameras only |
| Measuring volume length | 950.000 mm |
| Measuring volume width | 1025.000 mm |
| Measuring volume depth | 1025.000 mm |
| ***Calibration*** | |
| Calibration object name | Calibration cross |
| Calibration date | Fri Oct 2 11:30:20 2020 |
| Snap mode | Single snap |
| Calibration deviation | 0.072538 |
| Scale deviation | 0.002 mm |
| Camera angle | 22.996 ° |
| Measurement temperature | 20.0 °C |

Figure 110. DIC calibration quality data for tests A16-GA_0010 – A16-GA_0012 from GOM Correlate.

**Werkskalibrierschein**

*Proprietary Calibration Certificate*

GOM GmbH
Schmitzstraße 2
38122 Braunschweig
Germany

| | |
|---|---|
| Kalibrierschein-Nr.<br>*Calibration Certificate no.* | *CG1121*<br>2020-05-08 |

| | |
|---|---|
| Gegenstand<br>*Object* | Kalibrierkreuz<br>*Calibration cross* |
| Hersteller<br>*Manufacturer* | GOM GmbH |
| Typ<br>*Type* | CC20/MV1000x800 |
| Serien-Nr.<br>*Serial no.* | CG1121 |
| Material<br>*Material* | CFK Typ 2<br>*Carbon fiber type 2* |
| Ausdehnungskoeffizient<br>*Coefficient of thermal expansion* | $-0.03*10^{-6}$ $K^{-1}$ |
| Anzahl der Seiten<br>*Number of pages* | 10 |
| Datum der Kalibrierung<br>*Date of calibration* | 08.05.2020 |

Dieser Werkskalibrierschein darf nur vollständig und unverändert weiterverbreitet werden. Auszüge oder Änderungen bedürfen der Genehmigung der ausstellenden Firma. Dieser Kalibrierschein wurde per EDV erstellt und hat ohne Unterschrift Gültigkeit.

*This calibration certificate may only be reproduced to its full extent and without any modifications. Extracts or changes require the prior written approval of the issuing party. This calibration certificate was created by electronic data processing and is legal without signature.*

| | |
|---|---|
| Datum der Ausstellung<br>*Date of issue* | 08.05.2020 |
| Prüfer<br>*Inspector* | Detlef Köhler |

## 1) Kalibriergegenstand / Calibration object

Der Kalibriergegenstand ist ein Kalibrierkreuz vom Typ CC20/MV1000x800 (siehe Abbildung 1). Das Kalibrierkreuz trägt die Seriennummer CG1121. Das Kalibrierkreuz besteht aus zwei länglichen, quaderförmigen Elementen, die auch als Kreuzschenkel bezeichnet werden. Sie sind durch ein Gelenk miteinander verbunden. Das Gelenk umfasst eine Gelenkfixierung. Die Kreuzschenkel sind aus dem Material CFK Typ 2 gefertigt. Auf den Kreuzschenkeln sind mehrere optische Kreismarken in einer definierten Anordnung fixiert. Einige dieser Marken sind durch zusätzliche Kreisscheibenelemente codiert.

*The calibration object is a calibration cross of the type CC20/MV1000x800 (see figure 1). The calibration cross has the serial number CG1121. The calibration cross consists of two elongated, rectangular elements which are also referred to as arms of the cross. They are connected to each other through a joint. The joint includes a joint fixing. The arms of the cross are made out of the material Carbon fiber type 2. Several optical circular markers are fixed on the arms of the cross in a defined arrangement. Some of these markers are coded by additional circular disc elements.*

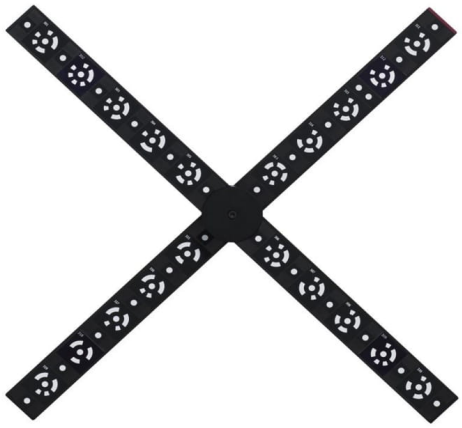


Abbildung 1: Kalibrierkreuz vom Typ CC20/MV1000x800
*Figure 1: Calibration Cross of the type CC20/MV1000x800*

Die zu bestimmenden Messwerte (siehe Abbildung 2) sind der räumliche Kreismittelpunktabstand zwischen den codierten Punkten 302 und 309 (Distanz D1) sowie der räumliche Kreismittelpunktabstand zwischen den codierten Punkten 312 und 318 (Distanz D2).

*The measuring values to be determined (see figure 2) are the spatial distance of the circle centers between the coded points 302 and 309 (distance D1) and the spatial distance of the circle centers between the coded points 312 and 318 (distance D2).*

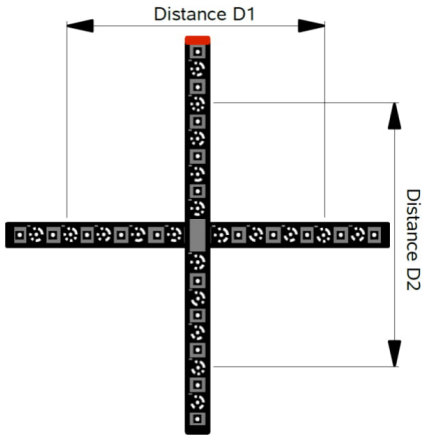



Abbildung 2: Zu kalibrierende räumliche Kreismittelpunktabstände
*Figure 2: Spatial distances of the circle centers to be calibrated*

## 2) Kalibrierverfahren / Calibration procedure

Das Kalibrierkreuz wird mit einer Messkamera des Typs Nikon D7200 mit der Seriennummer 4337690 gemessen. Die Kamera ist ausgestattet mit einem Objektiv des Typs Titanar 24 mit der Seriennummer 20957 sowie einen Aufsteckblitz des Typs SB700 mit der Seriennummer 3022856. In jedem aufgenommenen Messbild können 2D-Koordinaten der zu messenden Kreismarken des Kalibrierkreuzes ermittelt werden. Anschließend werden im Rahmen eines photogrammetrischen Bündelblockausgleichs die zugehörigen 3D-Koordinaten berechnet.

*The calibration cross is measured with a Nikon D7200 measuring camera with the serial number 4337690. The camera is equipped with a Titanar 24 lens with the serial number 20957 and a SB700 accessory flash with the serial number 3022856. 2D coordinates of the calibration cross to be measured can be determined in each captured measuring image. Then, the corresponding 3D coordinates will be computed during a photogrammetric bundle adjustment.*

## 3) Messbedingungen / Measurement conditions

### Messkonfiguration / Measurement configuration

Vor der Messung werden die beiden Kreuzschenkel voneinander getrennt. Anschließend werden die Kreuzschenkel in einen photogrammetrischen Messaufbau eingebracht. Der Messaufbau umfasst zwei optische Referenz-Längenmaßstäbe, die beiden Kreuzschenkel sowie eine Vielzahl an codierten

optischen Kreismarken. Alle Elemente sind auf einer festen ebenen Fläche angeordnet. Dabei werden die zu kalibrierenden Kreuzschenkel zwischen den beiden optischen Referenz-Längenmaßstäben platziert. Die zusätzlichen codierten optischen Kreismarken sind sowohl auf als auch neben den Kreuzschenkeln sowie den optischen Referenz-Längenmaßstäben angeordnet. Ihre konvexe Hülle umschließt sowohl die Kreuzschenkel als auch die optischen Referenz-Längenmaßstäbe vollständig.

*Before the measurement, the two arms of the cross are disjoined. Then, the arms of the cross are placed in a photogrammetric measuring setup. The measuring setup includes two optical reference scale bars, the arms of the cross and multiple coded optical circular markers. All elements are arranged on a firm plane surface. The arms of the cross to be calibrated are placed between the two optical reference scale bars. The additional coded optical circular markers are arranged on and next to the arms of the cross and the optical reference scale bars. Their convex envelope completely encloses the arms of the cross as well as the optical reference scale bars.*

**Sensorkonfiguration / Sensor configuration**

Die Messkamera wird mit folgenden Einstellungen betrieben:

*The measurement camera is operated with the following settings:*

| | |
|---|---|
| Modus<br>*Mode* | Manuelle Belichtungssteuerung<br>*Manuel mode* |
| Autofokus<br>*Autofocus* | Aus<br>*Off* |
| Belichtungszeit<br>*Shutter speed* | 1/250 s |
| ISO-Empfindlichkeit<br>*ISO sensitivity* | 200 |
| Bildfeld<br>*Image Area* | DX (24 mm x 16 mm) |
| Bildqualität<br>*Image quality* | JPEG Fine<br>*JPEG Fine* |
| Weißabgleich<br>*White Balance* | Blitz<br>*Flash* |
| Picture-Control-Konfiguration<br>*Picture control* | Neutral<br>*Neutral* |

Das Objektiv wird mit folgenden Einstellungen betrieben:

*The lens is operated with the following settings:*

| | |
|---|---|
| Fokussierung<br>*Focus setting* | Fixiert, konstant<br>*Fixed, constant* |
| Blende<br>*Aperture* | 11 |

Der Aufsteckblitz wird mit folgenden Einstellungen betrieben:

*The accessory flash is operated with the following settings:*

| | |
|---|---|
| Blitzmodus<br>*Flash mode* | Manuell<br>*Manual* |
| Ausleuchtungsprofil<br>*Illumination pattern* | Standard<br>*Standard* |
| Reflektorposition<br>*Zoom head position* | identisch zur Brennweite des Objektivs<br>*identical to the focal length of the lens* |
| Intensität der Blitzleistung<br>*Flash output level* | 1/4 |

Die Messfähigkeit des eingesetzten Messsystems bestehend aus Messkamera, Objektiv sowie Aufsteckblitz wird durch eine jährliche Annahmeprüfung gemäß VDI/VDE 2634 Blatt 1 geprüft.

*The performance of the measuring system, including the measuring camera, the lens and the accessory flash, is verified with an annual acceptance test according to VDI/VDE 2634 part 1.*

**Optische Referenz-Längenmaßstäbe / Optical reference scale bars**

Zur Definition des Maßstabs der Kalibrierung werden zwei optische Referenz-Längenmaßstäbe eingesetzt. Ihre räumlichen Längen sind im Rahmen einer DAkkS-Kalibrierung bestimmt worden. Die zugehörigen Kalibrierscheine dokumentieren die Rückführung auf nationale Normale zur Darstellung der Einheiten mit dem internationalen Einheitensystem (SI).

*Two optical reference scale bars are used to define the scale of the calibration. Their spatial lengths have been determined by a DAkkS calibration. The corresponding calibration certificates provide traceability to recognized national standards and to the International System of Units (SI).*

Die optischen Referenz-Längenmaßstäbe weisen folgende Eigenschaften auf:

*The optical reference scale bars have the following characteristics:*

| | | |
|---|---|---|
| Serien-Nr.<br>*Serial no.* | SE0045 | SE0046 |
| Typ<br>*Type* | Ref-SB I 1000 | Ref-SB I 1000 |
| Kalibrierscheinnummer<br>*Calibration certification no.* | 31433/D-K-15151-01-00/2020/01 | 31434/D-K-15151-01-00/2020/01 |
| Kalibrierdatum<br>*Calibration date* | 21.01.2020 | 21.01.2020 |
| Kalibrierlabor<br>*Calibration laboratory* | eumetron GmbH | eumetron GmbH |

Die DAkkS ist Unterzeichner der multilateralen Übereinkommen der European cooperation for Accreditation (EA) und der International Laboratory Accreditation Cooperation (ILAC) zur gegenseitigen Anerkennung der Kalibrierscheine.

*The DAkkS is signatory to the multilateral agreements of the European cooperation for Accreditation (EA) and of the International Laboratory Accreditation Cooperation (ILAC) for the mutual recognition of calibrations certificates.*

Gemäß der zugehörigen Akkreditierungsurkunde „D-K-15151-01-00" beträgt die kleinste angebbare erweiterte Messunsicherheit:

*According to the specific Accreditation certificate „D-K-15151-01-00", the smallest assignable expanded measurement uncertainty is:*

- erweiterte Messunsicherheit k=2 (P = 95%)
- *expanded measurement uncertainty k=2 (P = 95%)*

**$U = 0.5\ \mu m + 1.0 * 10^{-6} * L$**

**Kalibrieraufgabe /Calibration task**

Bestimmt werden soll der räumliche Abstand zwischen den beiden codierten optischen Kreismarken 302 und 309 beziehungsweise 312 und 318 gemäß Abbildung 2. Der Bezugspunkt ist jeweils der Kreismarkenmittelpunkt.

*The spatial distance between the two coded optical circular markers 302 and 309 or 312 and 318 is to be determined according to figure 2. The reference point is the center of each circular marker.*

**Messstrategie / Measuring strategy**

Mit Hilfe der Messkamera werden 52 Bildaufnahmen der Messkonfiguration von a priori definierten Standpunkten durchgeführt.

*52 images of the photogrammetric measuring setup are taken from a defined and reasoned set of camera positions.*

40 von den 52 Bildaufnahmen werden von Standpunkten gemessen (entsprechend der handgeführten Reproduzierbarkeit einer Position), die alle auf einer imaginären Kugel liegen, wobei das Zentrum der Kugel mit dem Zentrum der Messkonfiguration zusammenfällt und der Radius der Kugel der optimalen Objektweite gemäß der Fokuseinstellung des Objektives entspricht. Die optischen Achsen der Messungen schneiden sich genähert im Zentrum der Messkonfiguration. Die Standpunkte umfassen somit die Messkonfiguration in einer geometrischen optimalen Weise.

*40 of the 52 images are measured from positions located on an imaginary sphere, accepting the positional reproducibility of a hand-operated camera. The center of the imaginary sphere coincides with the center of the photogrammetric measuring setup. The radius of the sphere corresponds to the optimal object distance determined by the focus setting of the lens. The optical axes of the measurements meet, approximately, at the center of the photogrammetric measuring setup. This measurement strategy provides the optimal geometric arrangement for the photogrammetric measuring setup*.

Die 40 Bildaufnahmen gliedern sich wie folgt auf:

*The 40 images are structured as follows:*

- Aus einer senkrechten Position bezüglich des Zentrums der Messkonfiguration werden vier Bildaufnahmen durchgeführt, wobei die Kamera zwischen den Aufnahmen jeweils um 90° um ihre optische Achse verdreht wird.
- *Four images are taken from a vertical position with respect to the center of the photogrammetric measuring setup, rotating the camera by 90° around its optical axis for each image.*

- Aus jeder Haupthimmelsrichtung (Nord, Süd, Ost und West) sowie den zugehörigen vier Nebenhimmelsrichtungen (Nordost, Südost, Nordwest, Südwest) werden jeweils drei Aufnahmen durchgeführt. Die optischen Achsen weisen jeweils einen Zenitwinkel (Bezugsachse ist die Normalenrichtung der Messkonfiguration) von 15°, 30° und 45° auf.
- *From each main compass direction (north, south, east, west) and the corresponding four ordinal directions (northeast, southeast, northwest, southwest) three images each are taken. The optical axes have a zenith angle (reference axis is the normal direction of the measurement configuration) of 15°, 30° and 45°.*

- Je Haupthimmelsrichtung und je Nebenhimmelsrichtung wird eine Aufnahme mit dem Zenitwinkel von 45° aufgenommen, wobei die Kamera um ihre optische Achse um 180° gedreht ist.
- *An image is captured with the zenith angle of 45° per main compass direction and per ordinal direction, rotating the camera by 180° around its optical axis.*

- Aus den Himmelsrichtungen „Ost" und „West" werden jeweils zwei Aufnahmen mit dem Zenitwinkel von 45° durchgeführt. Dabei ist die Kamera um ihre optische Achse um +/- 90° verkantet.
- *From the compass directions "east" and "west", two images each are taken with a zenith angle of 45°. The camera is tilted around its optical axis by +/- 90°.*

Die restlichen 12 Bildaufnahmen stützen den Bildverband zusätzlich ab. Sie liegen nicht auf der imaginären Kugel mit dem Radius der optimalen Objektweite und die optischen Achsen schneiden sich nicht im Zentrum der Messkonfiguration. Sie gliedern sich wie folgt auf:

*The remaining 12 images provide additional support to the image set. They are not located on the imaginary sphere with the radius of the optimal object distance. The optical axes do not intersect in the center of the photogrammetric measuring setup. Instead, the images are structured as follows:*

- Aus acht senkrechten Positionen bezüglich des Randes der Messkonfiguration wird jeweils eine Bildaufnahme durchgeführt. Jede Position bezieht sich je auf eine Haupthimmelsrichtung oder eine Nebenhimmelsrichtung. Die optische Achse schneidet den jeweiligen Messkonfigurationsrand.
- *One image each is taken from eight vertical positions with respect to the edge of the measurement configuration. Each position refers to one main compass direction or ordinal direction. The optical axis intersects the respective measurement configuration edge.*

- Aus jeder Nebenhimmelsrichtung wird je eine Bildaufnahme durchgeführt, wobei die optische Achse einen Zenitwinkel von 45° aufweist und die optische Achse den jeweils diametral entgegengesetzten Eckbereich der Kulisse schneidet.
- *One image is taken from each sub-compass direction. The optical axis has a zenith angle of 45° and the optical axis intersects the respective diametrical opposite corner area of the setup.*

**Berechnungsmethode / Calculation method**

Die 2D-Bildkoordinaten aller in den Bildaufnahmen erfassten optischen Kreismarken der Messkonfiguration werden durch die Methoden der digitalen Bildverarbeitung ermittelt. Auf Grundlage dieser 2D-Bildkoordinaten und a priori bekannten Näherungswerten der inneren Orientierung der Messkamera können im Rahmen einer photogrammetrischen Bündelblockausgleichung die 3D-Koordinaten der optischen Kreismarken bestimmt werden. Der Maßstab der Bündelblockausgleichung wird durch die beiden optischen Referenz-Längenmaßstäbe definiert. Nachfolgend werden aus den 3D-Koordinaten durch Anwendung des räumlichen Pythagoras die zu bestimmenden Längen des Kalibrierkreuzes berechnet.

*Digital image processing methods are used to determine the 2D image coordinates of all circular markers found in the set of images of the photogrammetric measuring setup. The 3D coordinates of the optical circular markers are determined by a photogrammetric bundle adjustment, using the 2D image coordinates and the theoretical approximate values for the parameters describing the inner orientation of the measuring camera. The scale of the bundle adjustment is defined by the two optical reference scale bars. Subsequently, the lengths of the calibration cross to be determined are computed from the 3D coordinates by using the spatial Pythagorean.*

Die Güte der photogrammetrischen Bündelblockausgleichung wird durch die Kontrolle der Prüfmerkmale „mittlere Bildpunktabweichung" und „mittlere Maßstabsabweichung" sichergestellt. Die Ist-Werte der beiden Prüfmerkmale müssen kleiner oder gleich dem zugehörigen aufgabenspezifischen Grenzwert sein.

*The quality of the photogrammetric bundle adjustment is ensured by the control of the testing features "average image point deviation" and "average scale bar deviation". The actual values of the testing feature must be smaller or equal to the corresponding task-specific limit value.*

| Prüfmerkmal<br>*Testing feature* | Messwert<br>*Measured value* | Grenzwert<br>*Limit* |
|---|---|---|
| Mittlere Bildpunktabweichung [Pix]<br>*Average image point deviation[Pix]* | 0.026 | 0.050 |
| Mittlere Maßstabsabweichung [mm]<br>*Average scale bar deviation [mm]* | 0.0014 | 0.0100 |

## 4) Umgebungsbedingungen / Ambient conditions

Die Messungen erfolgen in einem klimatisierten Messraum. Die Temperatur des Messaufbaus wird durch ein Kontaktthermometer gemessen. Die Temperatur lag während der Messung bei 21.4 °C. Die Messergebnisse werden auf eine Referenztemperatur von 20 °C umgerechnet.

*The measurements are carried out in an air-conditioned measuring room. The temperature of the measuring setup is measured by a contact thermometer. The temperature was 21.4 °C during the measurement. The measurement results are converted to a reference temperature of 20 °C.*

## 5) Messergebnisse / Measuring results

| Prüfling<br>*Testing feature* | Messwert in mm<br>*Measured value in mm* | Messwert in inch<br>*Measured value in inch* |
|---|---|---|
| Distanz D1<br>*Distance D1* | 840.651 | 33.0965 |
| Distanz D2<br>*Distance D2* | 840.024 | 33.0718 |

# APPENDIX J

## LITERATURE REVIEW

## UAV Risk Assessment and Impact Testing

Extensive research and testing has been done to evaluate the risks of bird to aircraft collisions. However, due to advances in technology birds are not the only airborne danger to aircraft. As a result, impact testing with UAV has been afforded time, resources, and effort. As part of ASSURE's Airborne Collision Vol. 1 [8], projectile and target definitions were outlined along with justification for these choices. In addition to this work, several articles have been published where the risks of UAS to aircraft have been modelled and or evaluated [1,3,33,34,35,36,40,43]. To concretely evaluate the risks of drones in air to air collisions with commercial aircraft, impact testing of DJI Phantom 3 drones and AWM 525 aircraft components was performed by the National Research Council Canada (NRCC) [21]. This research is detailed below.

The goal of these tests was to simulate impact between quadcopter and the wings and windscreens of commercial aircraft. Tests were conducted at representative velocities for an aircraft under 10,000 ft [21]. All impact tests assumed that the drone was flying parallel to the planes longitudinal axis. Drones were shot into components using an air cannon sabot to accelerate the projectile. High speed video was used to capture the impact event and the damage was documented. Fixtures were created to mount windscreens and wings for testing and can be seen in figures 111 and 112 respectively below.

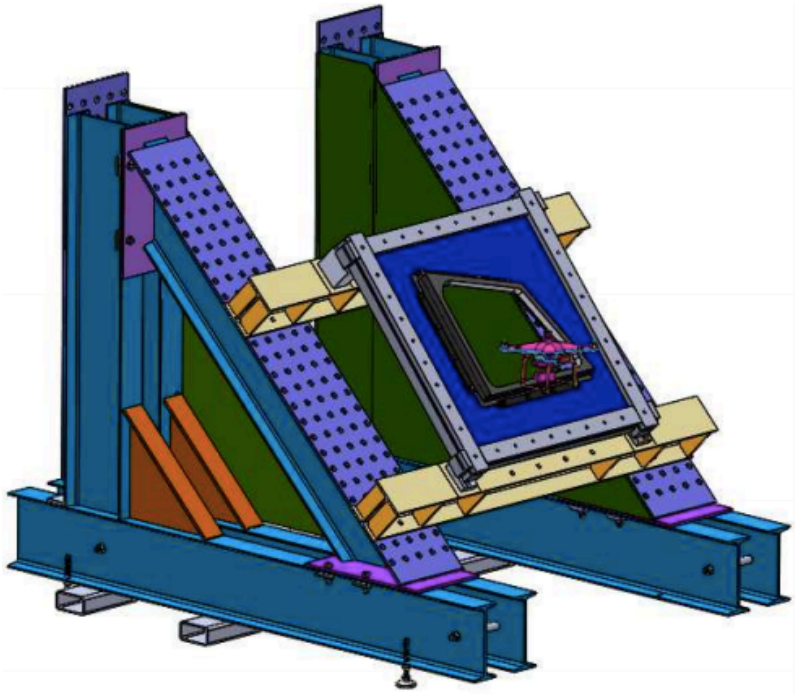


Figure 111. Windscreen testing fixture from NRCC report [21]

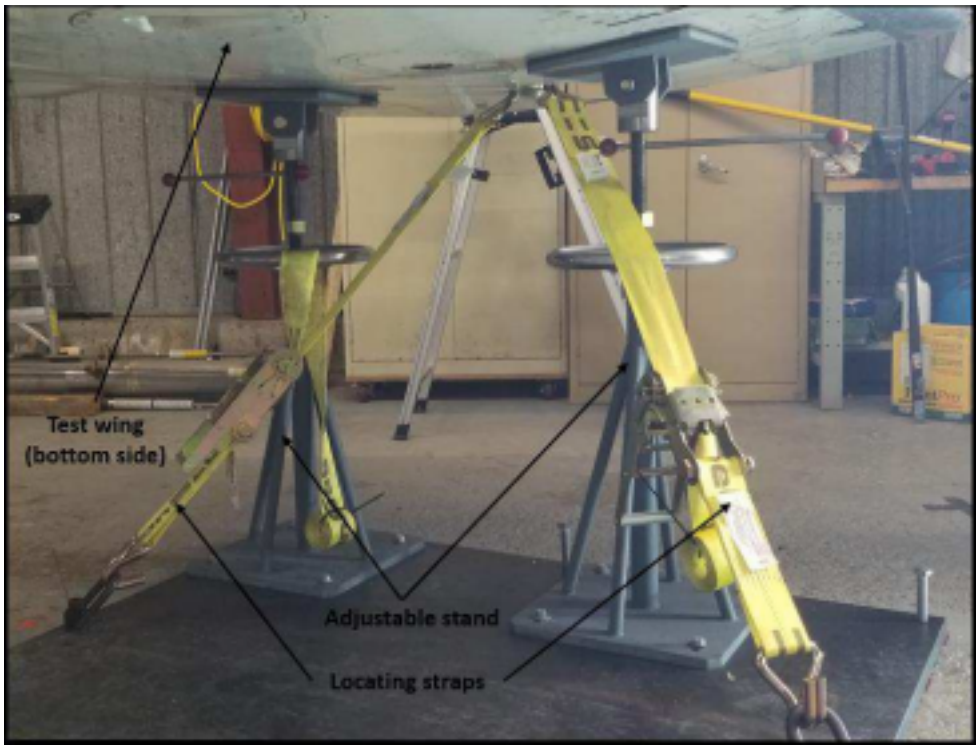



Figure 112. Wing stand for testing from NRCC report [21]

Two windscreen tests were performed in total, impacting at velocities of 140 kts and 250kts. Both windscreen tests resulted in severe damage, but no penetration of the windshield occurred, with the structural vinyl layer between the panes remaining in tact. Both the inner and outer windshield surfaces were shattered during the tests. Results for the first test can be seen below in figures 113 and 114.

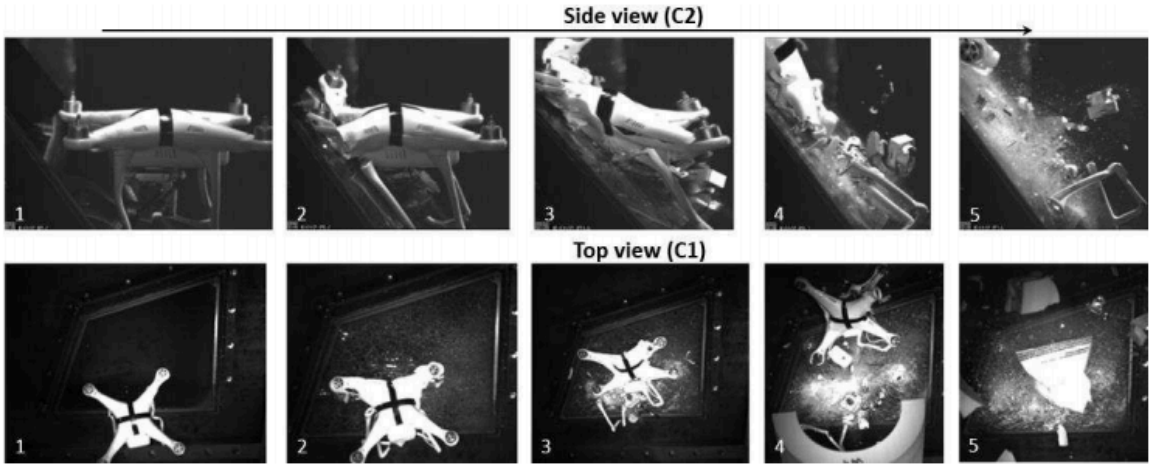


Figure 113. Windshield impact at 140 kts from NRCC report [21].



figure 114. Damage to outside of windshield (left) and inside of windshield (right) from NRCC report [21].

Wing tests were conducted with varying target zones along the wing length, six tests in total were performed. Four tests were performed at a velocity of 140 kts and two tests were performed with velocity 250 kts. Damage from wing test #2 consisted of extensive plastic deformation on the external skin, distortion of secondary parts, but no failure of the skin. Using reference damage level categories from FAA-ASSURE [7], this test resulted in level 2 damage. Other wing tests at 140 kts yielded similar results, with level 3 damage being sustained only during one 250 kts test. Level three damage consists of extensive failure of wing skin and penetration of drone parts into the interior structure. Results from test #2 are shown below in figures 115 - 117.

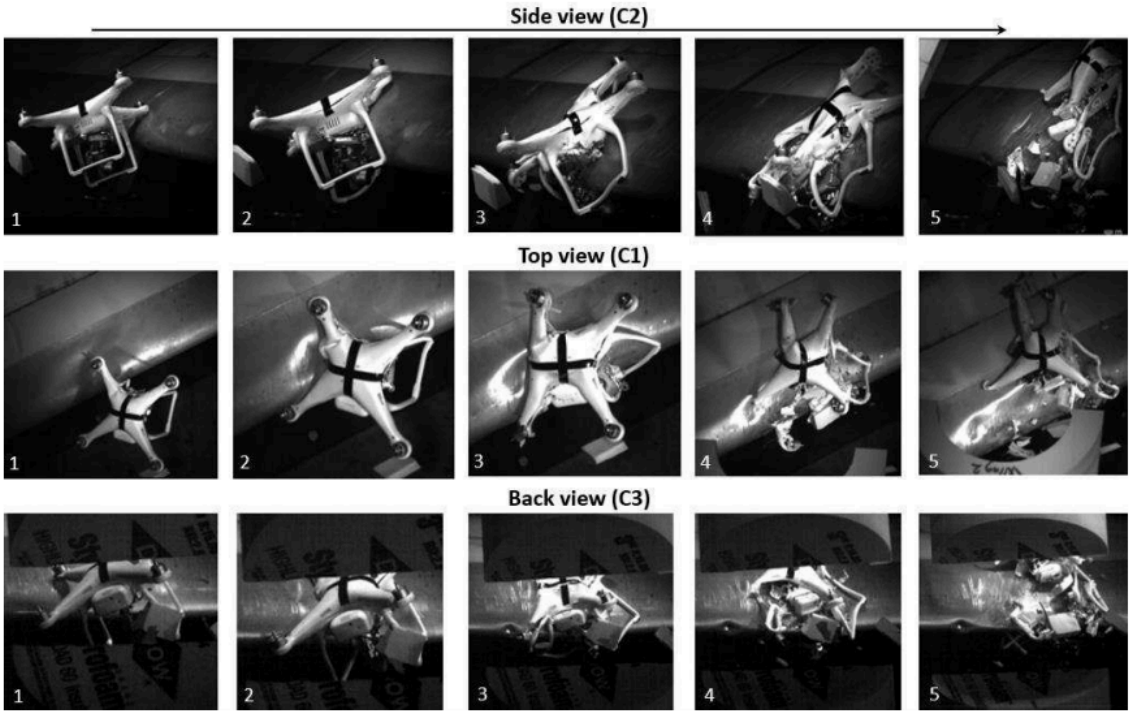



Figure 115. Drone to wing slat impact during test #2 from NRCC report [21].

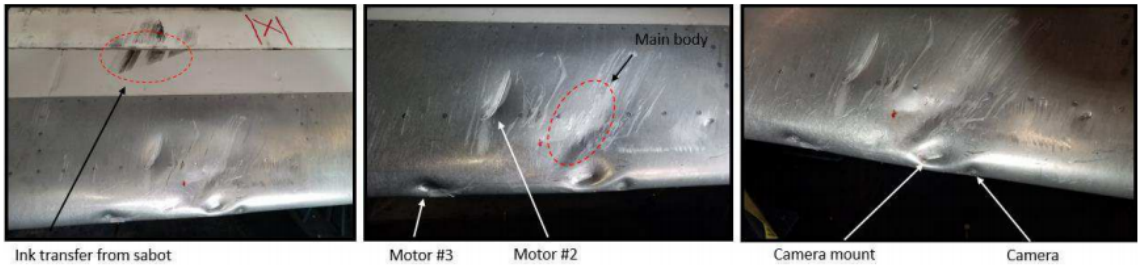



Figure 116. Post test pictures of wing slat from NRCC report [21].




Figure 117. Slat deflection post wing test from NRCC report [21].

In conclusion, impact tests between quadcopter and AWM 525 aircraft components were conducted by the NRCC. Windscreen tests showed that significant damage may result from impact, with all glass plies being shattered and substantial amounts of glass fragments being released into the cabin. Damage for these tests increased with the velocity of the drone. Wing testing showed that the battery impact location plays an important role in damage severity. At 140 kts, results ranged from plastic deformation to extensive damage of the skin and the underlying honeycomb structure of the wing. At high velocity (250 kts) drone impacts caused skin fracture, severe deformation of the wing slat, damage to the leading edge, and penetration of drone parts into the wing structure.

This study provides insight into some of the testing being done to evaluate the

severity of drone to aircraft collisions. Most of the research done thus far has involved commercial aircraft only, and has focused primarily on damage documentation. Similar testing of smaller recreational aircraft will help complete the picture of threats posed by drones to aviation as a whole. Capture of additional impact data such as load response and deflections of the test article will further characterize damage from such collisions.

## Digital Image Correlation

To gain additional background on the use of DIC systems in high velocity testing, articles were reviewed [14,39,42]. In the research conducted by the Australian Department of Defense [14], a DIC system was adapted for use in large scale ballistic testing and its performance was evaluated. DIC is typically performed on a much smaller scale, and this article provided insight into applying it to large scale measurement such as in windscreen testing. An article on capturing the deformations of a panel from ballistic impact was also reviewed [42]. In the article, a single-camera high-speed stereo-digital image correlation technique is used to capture full field transient 3D deformation measurements during ballistic impacts. In this research, a single high speed camera in combination with a set of mirrors was used to capture the back side of the plate as it is impacted from two different views. They then use this set of images to track the motion of non uniform markings that have been placed on the back side of the target. Using these deformations, a deformation map was constructed. To verify the accuracy and effectiveness of their system, static deformation of a stationary carbon fiber reinforced polymer panel and transient deformation of an aluminum panel were measured under the impact of a cylindrical foam projectile. A gas gun was used to propel the projectile into

the plate, and an additional high speed camera was used perpendicular to the direction of travel of the projectile in order to determine the speed of the object. Once the methodology was confirmed, they then went on to study full field in-plane and out-of-plane deformations of the carbon panel when being impacted by a rigid steel sphere to learn about the deformation behavior and failure mechanisms of the panel. The procedure described in this work was very similar to that used with 3-D DIC in windscreen testing and as a result provided valuable insight.